Searches for Higgs Bosons in the Di-tau Decay Channels at the ATLAS Experiment

Thesis submitted in accordance with the requirements of the University of Liverpool for the degree of Doctor in Philosophy by

Katharine Julie Clementine Leney

September 2010

Abstract

The search for the Higgs boson will be one of the primary tasks of the LHC. One of the most promising channels in the search for a low mass Higgs boson (M_H $\sim$120 GeV) will be the scenario where the Higgs is produced via Vector Boson Fusion and subsequently decays to a pair of tau leptons. One of the dominant (and most complex) backgrounds to this analysis is expected to come from $t\bar{t}$ decays. Monte Carlo samples with a centre-of-mass energy of 14 TeV are used to investigate the contributions from different $t\bar{t}$ decay modes and to develop methods to reduce the contribution from this background process and improve the overall sensitivity of the analysis. A technique to estimate contributions from background processes when there are insufficient Monte Carlo samples available to calculate this directly is also presented.

A low mass Standard Model Higgs boson will require at least 10 fb^{-1} data before a discovery (or exclusion) can be claimed, but extensions to the Standard Model that realise Supersymmetry predict that there should be three neutral Higgs bosons. The production cross-section is strongly enhanced and it is therefore expected that competitive limits on an MSSM Higgs boson can be made using data from the 2010-2011 LHC data-taking period (1 fb^{-1} expected with 7 TeV centre-of-mass collisions). A search strategy for an MSSM Higgs boson decaying to two taus is presented, focusing on ensuring analysis robustness during this early period. Comparisons with the first ATLAS data are also made.

Acknowledgements

First and foremost, I would like to thank my supervisors Sergey Burdin and Andrew Mehta. Their support, advice and encouragement over the past four years has been invaluable and I am extremely grateful.

I would also like to thank the Science and Technology Facilities Council (STFC) for providing generous financial support for the duration of the degree and for giving me the opportunity to spend three and a half years at CERN.

The work presented in this thesis could not have been realised without the help of the Liverpool High Energy Physics group and the ATLAS Collaboration, especially the ATLAS Higgs and Data Quality groups. I thank all my colleagues at Liverpool and at CERN for all their help, and for making my PhD so enjoyable. In particular, Carl Gwilliam for his help with coding aspects of the work, Helen Hayward for having as much bad luck with computers as I do, and Sinead Farrington for analysis advice. I would also like to thank Tony Weidberg, who provided me with my first introduction to ATLAS in 2004. His guidance and encouragement was instrumental in starting me off down the PhD route.

Many thanks to my family who have encouraged and supported me every step of the way. Thanks too to all my friends. Finally, I would like to thank my husband Pierre for his love and patience.

Declaration

No portion of the author's work described in this thesis has been submitted in support of an application for another degree or qualification in this, or any other, institute of learning.

Contents

Chapter 1

Introduction

The Large Hadron Collider (LHC) is a proton-proton collider at CERN [1] near Geneva, Switzerland. Although currently operating at a reduced centre-of-mass energy of 7 TeV, it is still the most powerful particle accelerator in the world. After maintenance work scheduled for 2011, the LHC will then reach its design luminosity of 10^{34} $\mathrm{cm}^{-2}\mathrm{s}^{-1}$ and collisions at 14 TeV. By this time the stored energy in the beam will be equivalent to a Citröen 2CV travelling at 2540 mph.

There are four main experiments stationed at the interaction points around the 27km ring: ATLAS, CMS, LHCb, and ALICE. ATLAS and CMS are both general purpose detectors, designed to be sensitive to new physics, whereas the other two experiments have specific functions; LHCb is specialised in making measurements of events containing b-quarks and its main aim is to measure the source of CP violation, while the ALICE experiment is dedicated to the study of the quark-gluon plasma formed from heavy ion collisions. Data taking started in 2009 and at the time of writing 3.46 pb^{-1} of data has been collected.

Although the Standard Model of particle physics is well confirmed by experimental measurements, the Higgs boson (which is required if mass terms are to be introduced into the Standard Model Lagrangian) remains undiscovered. Searches for a Standard Model Higgs boson are one of the primary goals of the LHC experiments.

While a Higgs boson discovery will complete the Standard Model, it's presence introduces a hierarchy problem. Radiative corrections to the Higgs mass must be very extremely finely tuned to ensure that there is cancellation with the bare mass and to maintain the scale of electroweak symmetry breaking at the order of 1 TeV. One solution to this problem is to allow each Standard Model particle to have a Supersymmetric partner. If it exists, supersymmetry must be a broken symmetry, allowing the supersymmetric particles to be many times heavier than their Standard Model counterparts, and with a half integer spin difference. The simplest realistic model of supersymmetry is the Minimally Supersymmetric Standard Model (MSSM).

This thesis is concerned with searches for Standard Model and MSSM Higgs bosons, in the scenario where the Higgs boson decays to two tau leptons. The Standard Model and Supersymmetry are described in more detail in chapter 2, together with an introduction to searches for the Higgs boson at the LHC. Chapter 3 provides an overview of the ATLAS detector and its many sub-detectors. Ensuring that the data being taken is of sufficient quality for physics analysis and flagging any problems with the detectors which may cause a mis-interpretation of results is crucial. In chapter 4 a review of the ATLAS Data Quality Monitoring is provided, and a framework for assessing data quality from detector conditions information in described. The identification and reconstruction of physics objects (e.g. electrons, muons) is detailed in chapter 5. Finally, analyses for searches for Standard Model and MSSM Higgs bosons in the di-tau channels are presented in chapters 6 and 7, respectively.

Chapter 2

Theory

2.1 The Standard Model

The Standard Model of particle physics describes a system of fundamental particles and their interactions. The particles can be divided by their spin into three groups:

- The fermions, 6 quarks and 6 leptons (plus their antiparticles), each with spin $\frac{1}{2}$ are the constituents of the matter we see around us.
- The force-carrying bosons: the photon (γ), gluons, and the $W^{\pm}$ and Z^0 bosons responsible for the electromagnetic, strong and weak forces respectively. Each boson carries spin 1.
- The final member of the Standard Model is the spin 0 Higgs Boson and is, as yet, unobserved.

Although gravity is the most obvious force in our everyday lives, it is not described by the Standard Model, but has a negligible effect on the particles and their interactions at the smallest scales.

2.2 Electroweak Symmetry Breaking & the Higgs Mechanism

The Standard Model is a gauge theory built on the $SU(3)\times SU(2)\times U(1)$ symmetry of the three gauge groups describing the three forces. SU(3) accounts for Quantum Chromodynamics (QCD) which describes the strong interaction, while $SU(2)\times U(1)$ describes the unification of electromagnetism and the weak interaction, known as electroweak (EW) theory. Since it is a gauge theory, this implies that its Lagrangian is invariant under certain symmetries. This gauge invariance forbids the presence of mass terms in the Lagrangian; in other words, the gauge bosons (which we know from experiment to be heavy) must be massless.

This problem can be overcome by assuming that the various particles interact with a new type of scalar field, called the Higgs field, where the interactions of the field with the gauge bosons is gauge invariant but which behaves differently from other fields in the vacuum state where a 'spontaneous' breakdown of symmetry occurs [2] (in other words, the Higgs field has a non-zero value in the vacuum state). This is achieved by incorporating an $SU(2)$ doublet of complex scalars into the Lagrangian which couple to the massless gauge fields through a covariant derivative. The interactions of the gauge fields with the non-zero vacuum expectation value of the Higgs field lead not only to the acquisition of mass for the $W^{\pm}$ and Z bosons, but also (with the introduction of Yukawa couplings) for the fermions [3].

The particle associated with the Higgs field and predicted by this theory is known as the Higgs boson. The Standard Model is unable to make any prediction on the mass of the Higgs boson, and so far, no significant experimental evidence has been found for the particle. The LEP experiments put a lower limit on its mass of 114.4 GeV at 95% confidence level [4] and unitarity arguments suggest an upper limit of around 1 TeV. If a Higgs boson with a mass in this range does exist then it should be accessible at the LHC. Fits to precision electroweak

measurements constrain this further and suggest a lighter Higgs nass. Figure 2.1 shows $\Delta\chi^2$ as a function of M_H once observed values of SM parameters have been taken into account. From this it can be seen that a light Higgs is preferred, with a mass of around 85 GeV, although it should be noted that this region has been excluded by LEP. Furthermore, recent Tevatron results (see figure 2.2) have excluded a Higgs in the mass range 158 GeV $< m_H <$175 GeV with 95% confidence [5].

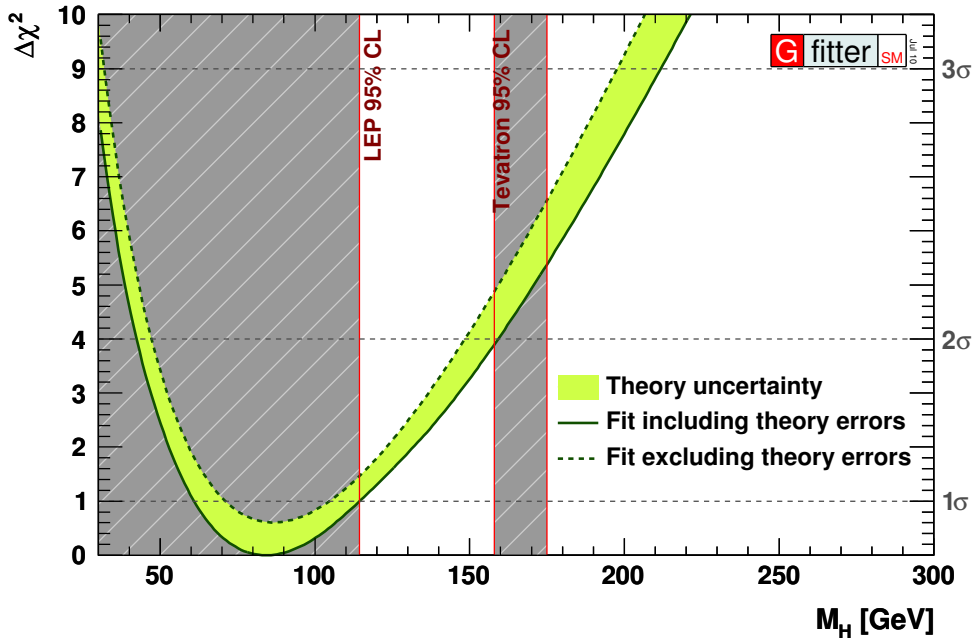

Figure 2.1: $\Delta\chi^2$ as a function of M_H after fitting to precision electroweak measurements, from [6]. The solid (dashed) lines give the results when including (ignoring) theoretical errors.

2.3 Why Go Beyond the Standard Model?

Although the Standard Model has withstood many tests over the last decades, several questions remain unanswered or unaccounted for within the Standard Model framework. These include:

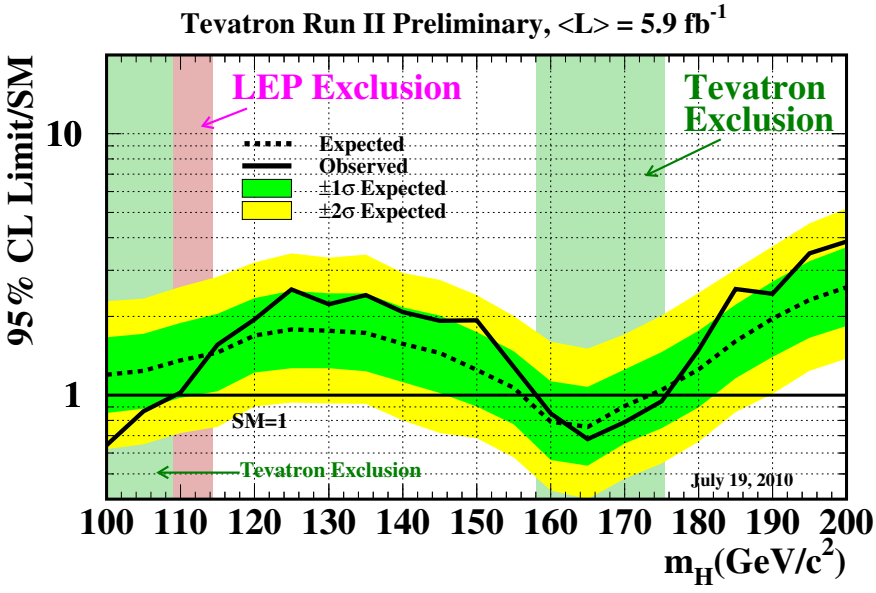

Figure 2.2: Combined CDF and D0 results for the observed and expected limits on a background-only hypothesis, from [5]. The limits are expressed as a multiple of the Standard Model prediction for test masses at 5 GeV intervals.

- **Higgs Boson Mass:** Radiative corrections to the Higgs mass must be calculated up to the energy at which the Standard Model can still be assumed to be valid (Λ). Quantum loop corrections to the Higgs mass are quadratically divergent and of the order Λ^2. If the SM is valid up to the Planck scale (10^{19} GeV) the corrections become enormous and must be cancelled by means of extreme fine tuning of the bare Higgs mass. This cancellation seems unlikely, although not completely unfeasible.

- **Mass Hierarchy:** There is a very wide range in the fermion masses, from the electron neutrino with a mass less than 2 eV, up to the top quark with a mass of 172 GeV – 11 orders of magnitude difference. The Yukawa couplings that give the fermions masses are inputs to the theory, but must be measured experimentally.

- **Unification of Electroweak and Strong Forces:** The Standard Model is described by an SU(3) $\times$ SU(2)$\times$ U(1) gauge group, where each subgroup has its own coupling constant. The couplings run with the energy scale and it would be natural if these converged toward a common value at some scale, although extrapolation of precision measurements indicates that they do not. Grand Unified Theories (GUT) assume that the coupling constants do converge. These typically require supersymmetric extensions of the Standard Model.

- **Gravity:** Although the other three fundamental forces are accounted for in the SM, gravity is not included. At the electroweak scale, gravity is so weak that it becomes negligible. Quantum gravity effects are only expected to become important at the Planck scale. The SM does not provide any explanation as to why gravity is so much weaker than the other forces either.

- **Dark Matter:** Only 4% of the universe is made from baryonic matter. The remaining 96% is thought to be composed of dark matter (23%) and dark energy (73%). The Standard Model only describes baryonic matter and no dark matter candidate is provided.

- **Baryogenisis:** The matter-anti-matter asymmetry in the universe is not explained by the Standard Model.

Because of these shortfalls, the Standard Model is thought to be a low-energy approximation of some other theory which can accommodate these features. Theories which include a supersymmetric extension to the Standard Model are widely believed to provide the most likely mechanism to answer these questions.

2.4 Supersymmetry

Supersymmetry (SUSY) introduces a symmetry between fermions and bosons, thus imposing a supersymmetric partner for every SM particle with a half unit

spin difference between them. Each SUSY particle will add its own terms into the quantum loop corrections to the Higgs mass. If SUSY were an exact symmetry these would exactly cancel the SM corrections, but in this case the SUSY particles would have the same mass as their SM counterparts which is known experimentally to be untrue. In order for the SUSY corrections to be not dramatically larger than the SM ones, the super-partners should have a mass of order 100 GeV.

The Minimally Supersymmetric Standard Model (MSSM) is the simplest supersymmetric extension to the SM, where only the minimum number of supersymmetric partners is allowed. The conservation of R-parity in the MSSM model means that the lightest super-symmetric particle will be stable, and could provide a dark matter candidate. Predictions for the mass of the top quark (m_t = 173.1 $\pm$1.3 GeV) and W-boson (M_W = 80.399 $\pm$0.023 GeV) are made within the MSSM. The results (see figure 2.3) are highly compatible with the model and show improvements over the SM [7].

The supersymmetric partners to the fermions take the name of the fermion with an 's' as a prefix (*e.g.* the supersymmetric partner to the electron is the 'selectron'), while the supersymmetric partners to the bosons take the suffix 'ino' (*e.g.* the supersymmetric partner to the W-boson becomes the 'Wino').

2.4.1 The Higgs Sector of SUSY

Two complex Higgs doublets are required in the MSSM - one to generate masses for "up-type" particles, and the other to generate masses for "down-type" particles. Each Higgs field has a vacuum expectation value, and the ratio of these is denoted as tanβ. Of the eight degrees of freedom provided by the two doublets, three of these are absorbed by the longitudinal components of EW bosons. Five observable Higgs bosons remain - three neutral ($\phi = h/A/H$) and two charged $H^{\pm}$. The h and H neutral Higgs bosons are CP-even, while the A-boson is CP-odd.

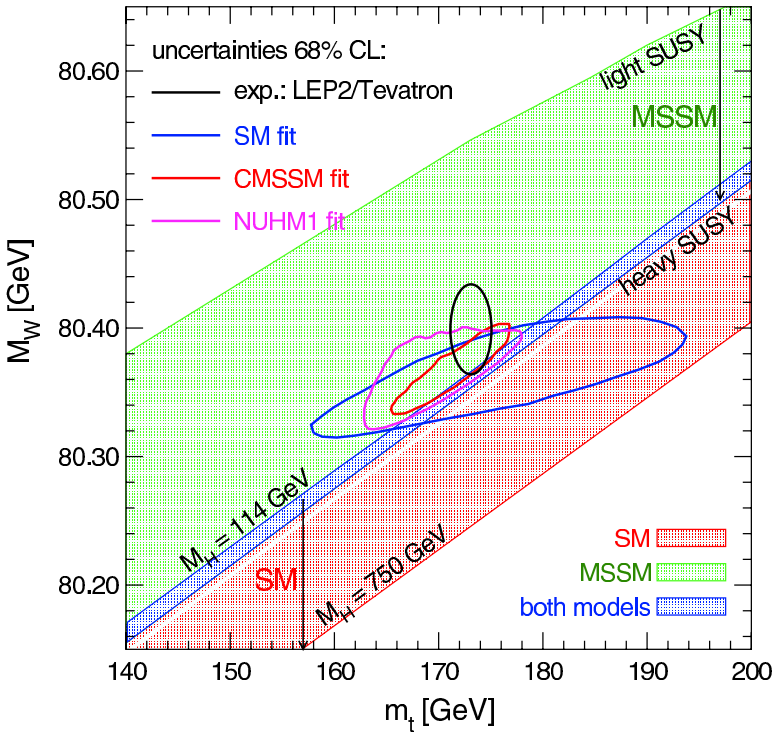

Figure 2.3: Predictions for m_t and M_W in the SM and MSSM. The red and blue shaded regions show the SM predictions. The green and blue regions show the MSSM predictions. The blue ellipse represents the 68% C.L. region in the m_t,M_W plane as predicted by a SM fit. Fits for two variants on the MSSM model (the Constrained MSSM (CMSSM) and NUHM1 (one non-universal Higgs mass) models) are shown in red and magenta respectively. The experimental bounds from the Tevatron and LEP2 are shown by the black ellipse.[7]

At tree level, the Higgs sector of the MSSM can be completely described in terms of tanβ and M_A. Higher order corrections introduce dependence on another 105 SUSY parameters. Making some general assumptions can reduce this somewhat, but it would be unfeasible to consider all possible scenarios. Instead, various benchmark models are defined [8]. The model used in the analysis described in chapter 7 is the 'maximal mixing' scenario (m_h max). The m_h max scenario is designed to give the largest possible mass for the mass of the lightest neutral Higgs boson (h) in order to provide the best agreement with limits from the

LEP experiments [4]. In this scenario, the relevant input parameters (and their assigned values) are summarised below [8]:

- $\mathbf{M_{SUSY}}$**:** Mass scale of squarks (= 1 TeV).
- $\boldsymbol{\mu}$**:** Higgs sector bilinear coupling (= 200 GeV).
- $\mathbf{M_2}$**:** Gaugino mass term (= 200 GeV).
- $\mathbf{A_t}, \mathbf{A_b}$**:** Trilinear couplings of stop and sbottom sectors ($A_t = A_b = 2$ TeV).
- $\mathbf{m_{\tilde{g}}}$**:** The gluino mass (= 0.8 M_{SUSY}).

2.5 Searches for Higgs Bosons at the LHC

2.5.1 Searches for the Standard Model Higgs Boson

The search for the SM Higgs boson is one of the primary tasks of the LHC and it has been established by many studies [9, 10] that a SM Higgs Boson can be discovered with high significance at the LHC, over the full range of mass interest, from the lower limit of 114 GeV up to about 1 TeV. At the LHC the predominant production mechanism will be gluon-gluon fusion. The second largest contribution comes from the fusion of vector bosons radiated from the initial state quarks [11]. The relative contributions of each depend on the Higgs mass. Cross-sections with next-to-leading order (NLO) QCD and EW corrections have been calculated (and incorporate the updated value for the top quark mass as confirmed by the Tevatron) [9]. These results are shown in figure 2.4.

The Higgs can decay in several modes, and the relative branching fractions as a function of mass are shown in figure 2.5. For $M_H >$ 125 GeV, the four-lepton decay from $H \rightarrow$ ZZ provides a very clean signature, but for a lower mass Higgs the branching fraction is very small. The $H \rightarrow \gamma\gamma$ channel looks to be a promising channel for Higgs masses less than 140 GeV, while for a heavier Higgs

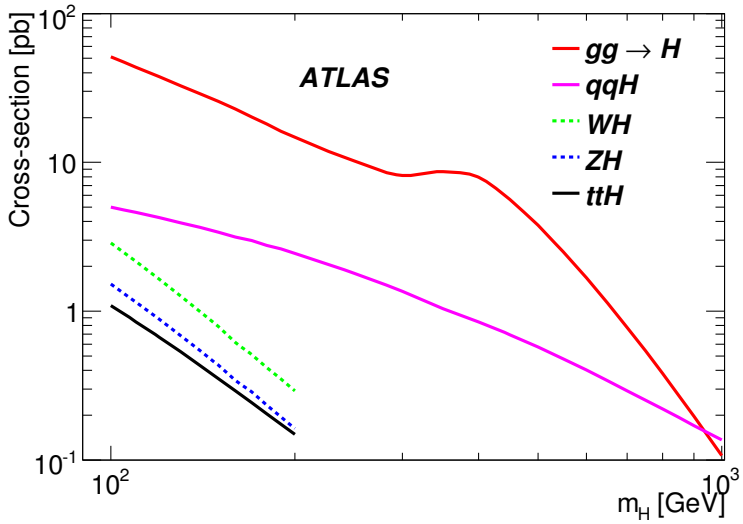

Figure 2.4: Cross-sections for different Higgs production mechanisms as a function of the Higgs mass, from [9]. Calculated to NLO with EW and QCD corrections.

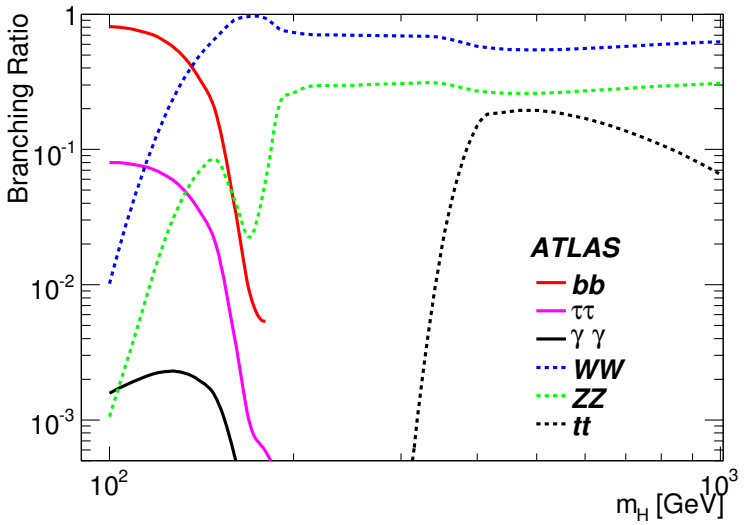

Figure 2.5: Branching ratios for different decay modes as a function of the Higgs mass, from [9]. Calculated to NLO with QCD and EW corrections.

the most promising search is for decay to a pair of W-bosons. The only direct fermion decays with significant branching ratios are to $b\bar{b}$ and to two tau leptons. These are particularly important channels for a measurement of the Higgs boson

coupling to fermions. Both modes have substantial QCD backgrounds, but while the di-tau channel can be identified by two high p_T leptons, the b-quarks in the $b\bar{b}$ decay mode will generally produce jets or low p_T leptons which makes the events extremely hard to distinguish from backgrounds. The success of analyses in different decay modes also depends heavily on detector performance. The di-photon channel requires excellent calorimetry and photon identification, while the $b\bar{b}$ channel will be heavily reliant on b-tagging techniques which use the silicon detectors for vertexing. The VBF $H \to \tau\tau$ channel requires excellent tau identification (and therefore a good understanding of calorimetry and tracking - see section 5.3.1) and forward jet identification is important too.

2.5.2 Searches for MSSM Higgs Bosons

The MSSM requires two Higgs doublets, which leads to 5 observable Higgs bosons - 3 neutral ($h/A/H$ - denoted ϕ) and two charged ($H^{\pm}$). For $M_A <$ $\sim$130 GeV, the h-boson is mass degenerate with the A, while M_H remains constant at $\sim$130 GeV. For $M_A >\sim$130 GeV, the H becomes degenerate and M_h remains constant at $\sim$125 GeV. Production rates for an MSSM Higgs boson grow with $\tan^2\beta$, where $\tan\beta$ is the ratio of the vacuum expectation values of each of the Higgs doublets, thus the larger the value of $\tan\beta$, the higher the production cross-section will be. At lower values of $\tan\beta(\leq 10)$, production is dominantly via gluon-fusion (figure 2.6a). As $\tan\beta$ increases production in association with b-jets (figure 2.6b-d) gains in importance, and 0-2 b-jets can be observed in the final state.

Decays to third generation fermions are enhanced for a large region of the MSSM phase-space. The dominant decay mode is to $b\bar{b}$ pairs, accounting for approximately 90% of all decays. As with Standard Model Higgs searches, large QCD backgrounds associated with this final state make the analysis difficult, although the enhanced production cross-section (with respect to a SM Higgs) and the possibility to take on a third or fourth b-jet could make this channel feasible.

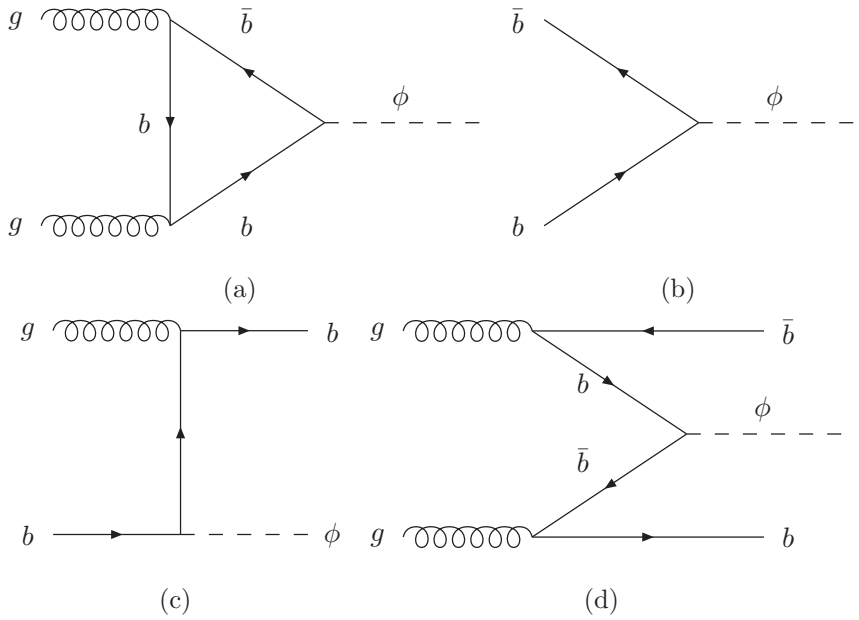

Figure 2.6: Feynman representations of MSSM ϕ production, by gluon-fusion (a), or via interactions with b-quarks (b)-(d).

Approximately 10% of all MSSM Higgs boson decays are to taus, providing the possibility of a high p_T lepton for triggering. Finally decays to $\mu^+\mu^-$ provide a viable search channel, thanks to it's clean final state which compensates for the low yield of just 0.03%. Limits on MSSM Higgs searches at the Tevatron and at LEP are summarised in figure 2.7.

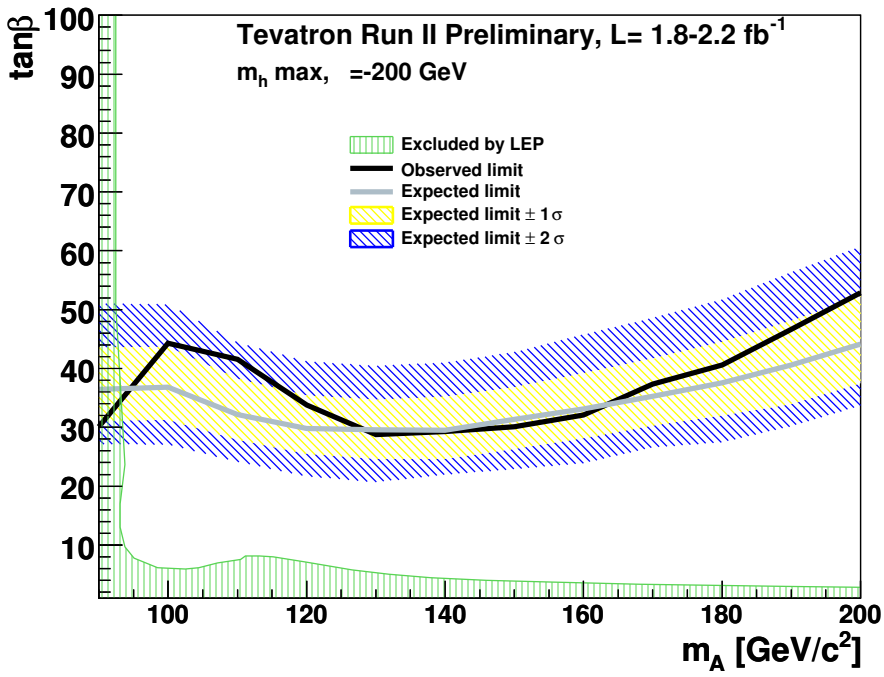

Figure 2.7: Combined CDF and D0 results for upper limits on MSSM Higgs boson production with di-tau final states, from [12]. LEP limits are also shown.

Chapter 3

The ATLAS Experiment

ATLAS (A Toroidal LHC ApparatuS) is a general purpose detector, designed to identify the broadest range of particles and measure their properties. It is 44m long, with a diameter of 25m, and weighs 7000 tonnes. Taking the classic 'onion' 4π design, it consists of a number of concentric cylinders and endcaps of increasing radius built around the interaction point and can be divided into three main components: the inner detector, the calorimeters, and the muon chambers. In addition, two magnet systems provide a solenoidal field in the inner detector and a toroidal field in the muon detectors to bend the paths of charged particles and allow a measurement of their transverse momentum. An overview of the detector is shown in figure 3.1. Finally, several smaller detectors in the very forward direction provide measurements of the absolute luminosity.

3.0.3 Co-ordinate System

ATLAS uses a right-handed co-ordinate system, with the x-axis pointing towards the centre of the LHC ring, the y-axis pointing upwards, and the z-axis following the beam direction. The azimuthal angle (ϕ) and polar (θ) angles are defined with respect to this axis system. Pseudorapidity (η) is more commonly used to represent the polar angle, rather than θ. This is defined in equation 3.1.

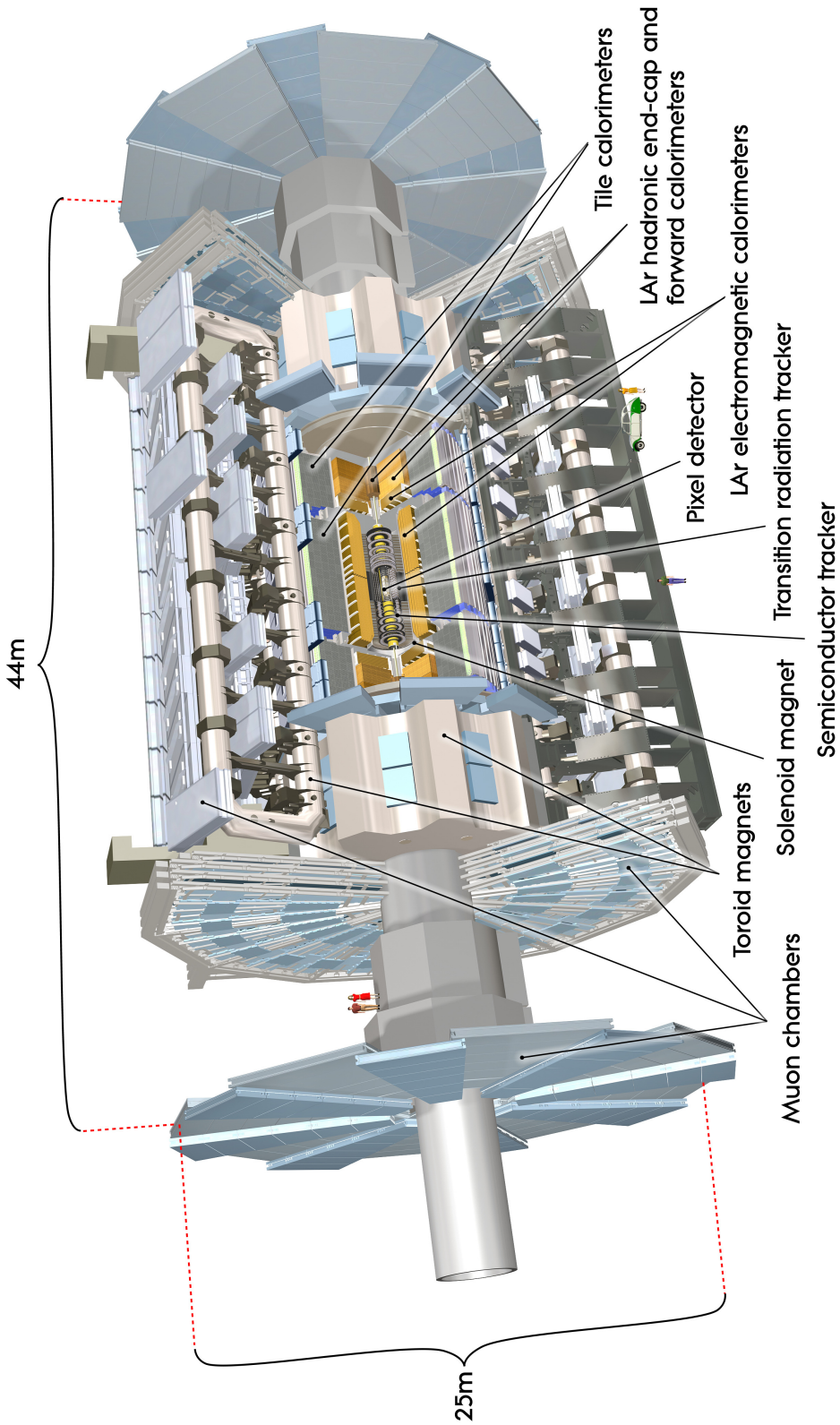

Figure 3.1: The ATLAS detector [13].

Detector Component	$\|\eta\|$-coverage
Inner Tracking Detectors	2.5
EM Calorimeters	3.2
Hadronic Calorimeters	4.9
Muon Spectrometers	2.7

Table 3.1: Coverage provided by detector components.

$$\eta = -ln\left(\tan\frac{\theta}{2}\right) \tag{3.1}$$

The angular separation (ΔR) between two particles is usually defined to be:

$$\Delta R = \sqrt{(\Delta\eta)^2 + (\Delta\phi)^2} \tag{3.2}$$

The detector is designed to have as large an acceptance as is practically possible to ensure that any new particles which may be created are detected, and for an accurate measurement of missing transverse energy. This is summarised in terms of η in table 3.1.

3.1 The Inner Detector

At a radius of just 5 cm out from the beam pipe, extending to a radius of 1.2 m and providing full coverage for $|\eta| < 2.5$, the inner detector is used for tracking charged particles. It has three components, the pixel detector, the semi-conductor tracker (SCT) and the transition radiation tracker (TRT). A schematic of the complete inner detector system is shown in figure 3.2. Figure 3.3 provides a more detailed view of individual components.

Surrounding the inner detector components is the inner solenoid which produces a 2 Tesla magnetic field to bend the trajectories of charged particles. By measuring the curvature of the track, the transverse momentum (p_T) and charge of the particle can be deduced. Particles with a transverse momentum less than 400 MeV will not be detected since at these low energies their paths will be so tightly curved by the magnetic field that they will not stray far enough from the

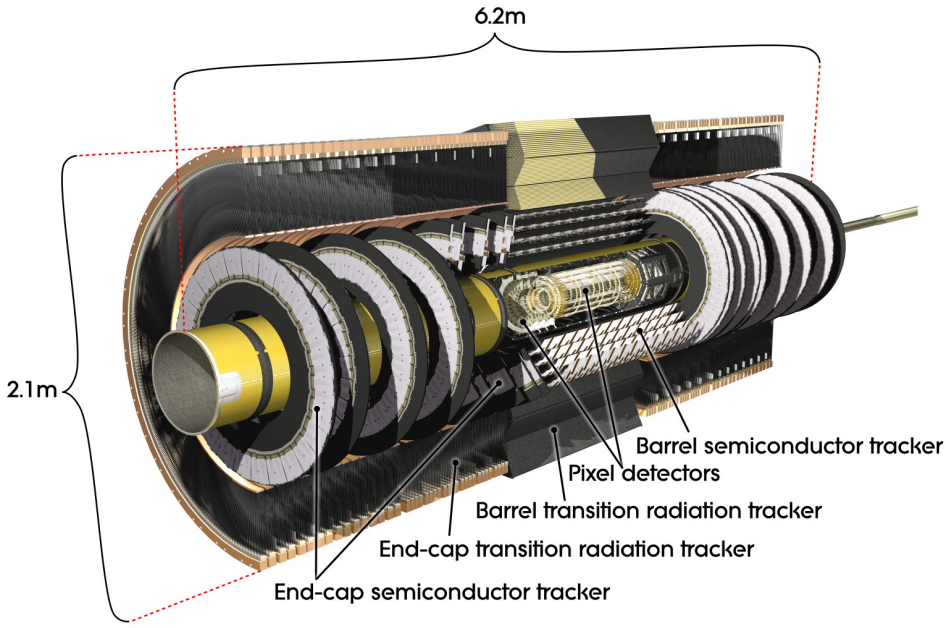

Figure 3.2: A 3-dimensional drawing of the ATLAS Inner Detector, showing various components [13].

interaction point to be detected. The Inner Detector provides a relative momentum resolution of ∼2% for tracks with a p_T of 1 GeV, up to ∼10% for higher p_T tracks ($p_T > 100$ GeV), where the resolution starts to deteriorate as particle paths become straighter.

3.1.1 Pixel Detector

The innermost component of the inner detector is the pixel detector. With three barrels and three endcaps and a total of 1744 n^+ in $n-$bulk silicon modules, each with approximately 47,000 50 μm by 400 μm pixels, it provides excellent tracking with a resolution of 12 μm in the r-ϕ direction, and 60 μm in the z-direction [14].

3.1.2 SCT (Semi-Conductor Tracker)

The middle component of the inner detector is the SCT. It consists of four barrel layers and two endcaps with 9 discs in each and uses double sided p-in-n sili-

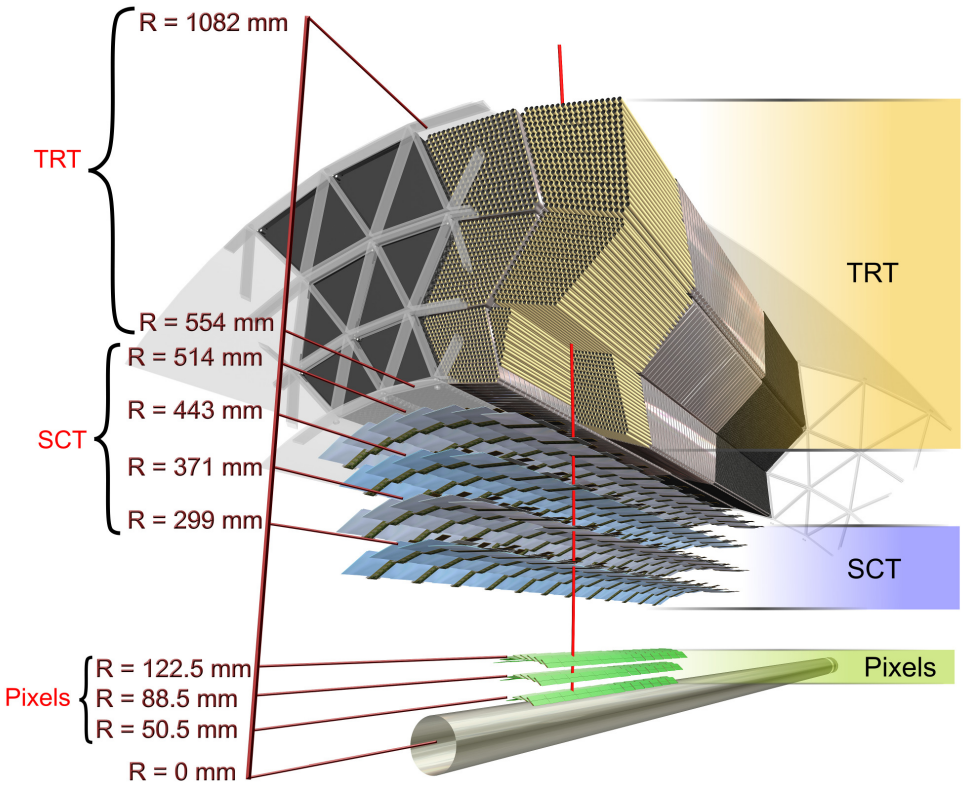

Figure 3.3: A slice of the ATLAS Inner Detector, showing details and positions of various components [13].

con strip detectors. Modules in the barrel region are all identical and have an 80 μm strip pitch with the strips on one side of the detector aligned to the beam direction and those on the other at a 40 mrad stereo angle to provide a measurement in the z-direction. Because of geometrical constraints, wedge shaped modules with varying strip pitch (from 55 μm to 90 μm depending on their position within the tracker) are required for the end-cap modules. In total there are 4088 modules, with 6 million readout channels, providing a resolution in ϕ of 23 μm [14].

3.1.3 TRT (Transition Radiation Tracker)

Surrounding the SCT is the TRT: a combination of straw tracker and transition radiation detector. It contains a total of about 351,000 'straws' (each 4 mm in diameter and up to 144 cm long) in its three barrel rings and two end-caps. Each straw is filled with gas (70% xenon, 20% tetrafluoromethane (CF_4) and 10% carbon-dioxide) and has a high voltage 30 μm diameter gold-plated tungsten wire running through it. As a charged particle passes through the straw the gas is ionised and this in turn induces a charge on the wire which can then be detected. Polypropylene foils are placed around the straws to act as transition radiators. When a relativistic particle passes through materials of different refractive indices it can emit a photon which helps to leave a much stronger signal in the straws. Since the intensity of transition radiation is proprotional to the gamma-factor of the particle ($\gamma = E/m$), it is possible in this way to identify particles. Although the TRT has a much coarser resolution than the two silicon components of the inner detector, its complementary (and innately radiation hard) design means that it provides different information, and its cheaper construction cost means it can cover a larger volume. The resolution in $r - \phi$ is required to be 30 μm, and not worse than 50 μm once systematic uncertainties are taken into account [14].

3.2 The Calorimeters

Outside the solenoidal magnet surrounding the inner detector, lie the two calorimeters; the inner electromagnetic (EM) calorimeter and the outer hadronic calorimeter. Both are sampling calorimeters and use a high density metal to absorb the energy of the particles. The electromagnetic calorimeter is used to absorb the energy of electrons and photons and build up a picture of their decays. Although hadrons can start their showering process in the EM calorimeter too, they are unlikely to deposit all their energy there, but will nearly always only be absorbed fully in the hadronic calorimeter. The EM calorimeter uses liquid argon (LAr) as

a sampling material, while the hadronic calorimeter uses a combination of LAr and scintillating tile technologies. The relative positions and layout of the two calorimeter systems is shown in figure 3.4.

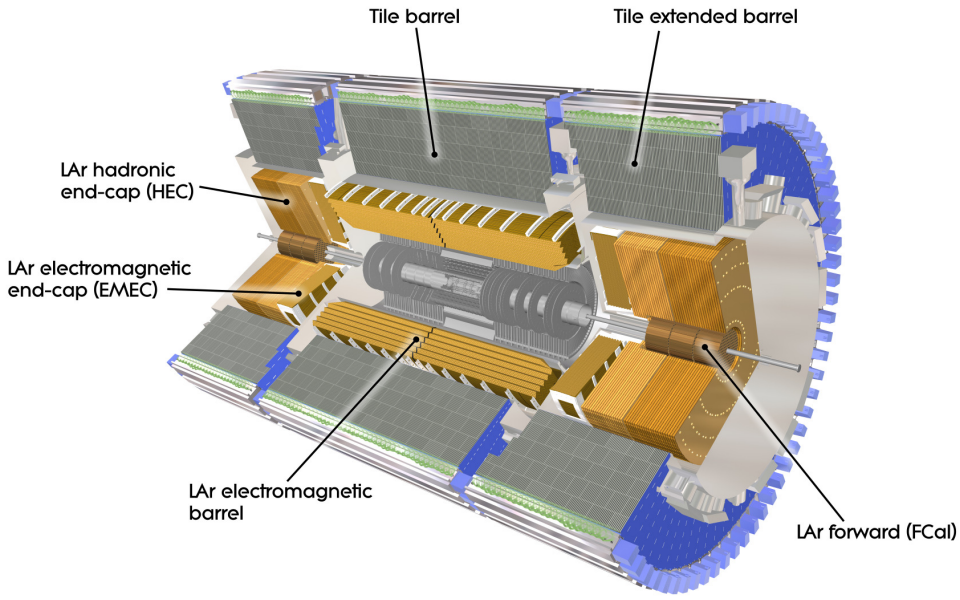

Figure 3.4: A schematic of the ATLAS electromagnetic and hadronic calorimeters [13].

3.2.1 LAr (Liquid Argon) Calorimeter

Using lead and stainless steel as energy absorbing materials, and liquid argon as a sampling material, an energy resolution of approximately $10\%/\sqrt{E}$ (in GeV) is achieved in the LAr Calorimeter. An accordion shaped geometry (see figure 3.5) is used to ensure that there is complete ϕ-symmetry with no azimuthal cracks. It has a total acceptance of $|\eta| < 3.2$ and is designed to fully absorb both electrons and photons [15].

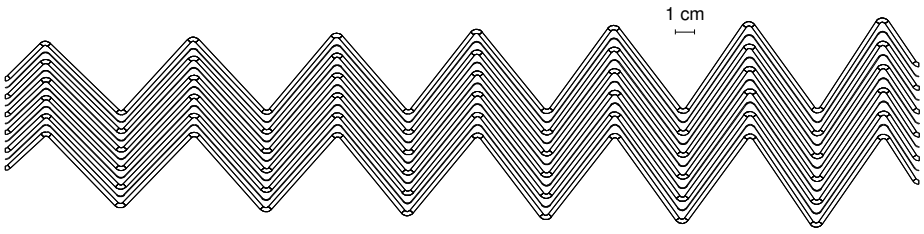

Figure 3.5: Transverse section through the barrel EM calorimeter [15].

3.2.2 Tile Calorimeter

The ATLAS hadronic calorimeter - the Tile Calorimeter - takes it's name from the scintillating tiles which are used to sample the energy. Steel is used as an energy absorbing material. It is less precise than the electromagnetic calorimeter with an energy resolution of around $50\%/\sqrt{E}$ (in GeV), but provides coverage up to $|\eta| < 4.9$ [15].

3.3 Muon Chambers

With a mean lifetime of 2.2×10^{-6} s, muons can effectively be treated as stable particles whilst in the detector and will generally be the only particles to survive passing through the calorimeters and reach the muon chambers. The detectors are arranged in layers and cover an area of 12,000 m^2 with 1,000,000 readout channels. They have a lower spatial resolution than the other detectors, but cover a much larger volume.

Four types of muon chambers are used in ATLAS for optimum performance. Those responsible for providing a trigger decision have a fast response time and cover a pseudo-rapidity range of $|\eta| < 2.4$. In the forward region the detectors need to be able to withstand a greater hit rate and are therefore designed accordingly. Closest to the interaction point, the detectors have the finest resolution and greatest radiation hardness. The layout is such that every muon track should pass through at least three trigger planes and at least three tracking detectors.

An overview of the ATLAS muon systems is shown in figure 3.6. A complete description of the ATLAS muon spectrometer can be found in [16] but is summarise in the following subsections for convenience.

The muon magnet system is the most distinctive feature of ATLAS and determines the overall dimensions of the experiment. It is composed of eight air-core superconducting toroidal barrel loops and two endcaps, storing a total of approximately 1.2 GJ of energy. The magnetic field is not uniform, but measurements do not need to be as accurate in the outer detector as in the inner detector.

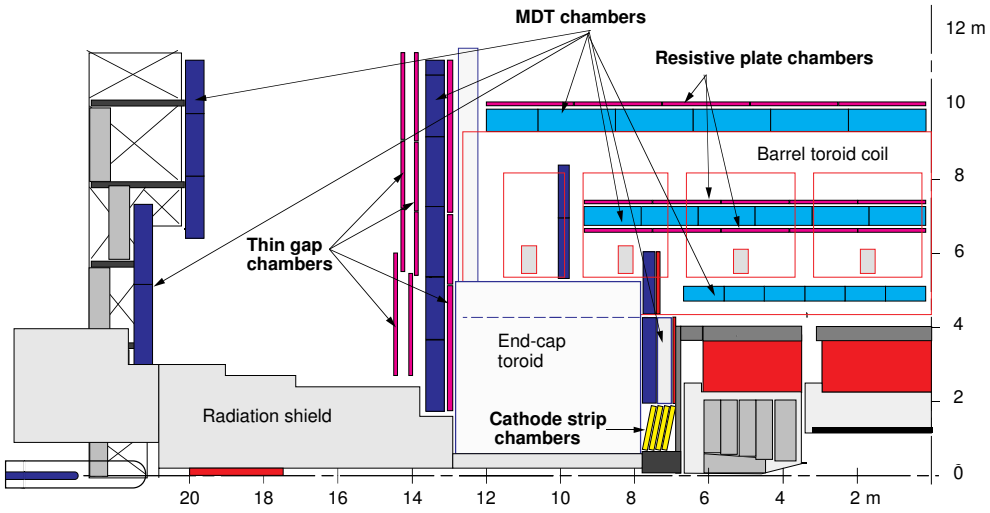

Figure 3.6: The ATLAS muon detectors [16].

3.3.1 MDT (Monitored Drift Tubes)

Precision measurements of the muon tracks in the r-z projection (parallel to the bending direction of the magnetic field) are made by the MDT chambers. The chambers provide coverage up to $|\eta| < 2.7$, with a single wire providing a resolution of $\sim$80 μm. The basic detection elements of the MDT chambers are 30 mm diameter aluminium tubes, filled with a gas mixture of 91% argon, 4% nitrogen and 5% methane and a 50 μm tungsten-rhenium (T-We) wire at 3270 V running through their centres. Any charged particle passing through the

tube will ionise the atoms in the gas. The resulting ions and electrons will then drift toward the wire, causing a cascade of ionisation which is then collected by the wire and detected as an electric current. The tubes are arranged in layers, with the wires running parallel to the direction of the magnetic field lines. Tube lengths vary from 70 to 630 cm, depending on their position in the detector. Precision measurements of the muon paths require that the position of the drift tubes is known to a high degree of certainty so an optical alignment system is used to monitor MDT wire displacements to an accuracy of ± 10 μm. A schematic drawing of an MDT chamber and of drift tube operation in a magnetic field are shown in figures 3.7 and 3.8 respectively.

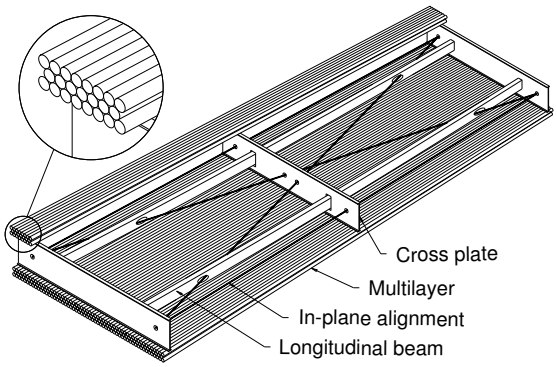

Figure 3.7: A schematic drawing of a rectangular MDT chamber from the barrel region of the detector. Endcap chambers are of a similar construction, but trapezoidal in shape [16].

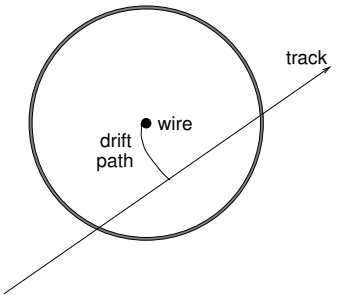

Figure 3.8: Drift tube operation in a magnetic field [16].

3.3.2 CSC (Cathode Strip Chambers)

In the innermost plane of the two endcaps where the background is highest, the MDTs are replaced with Cathode Strip Chambers (CSCs). These multi-wire proportional chambers operate on much the same principle as the MDTs, but the large diameter and high operating pressure of the MDTs makes them unsuitable for use in regions where high counting rates (>200 Hz cm^{-2}) are expected. The CSCs are therefore used in the innermost layer for $|\eta| > 2.0$ to provide a spatial resolution of 80 μm.

The CSCs are symmetric cells, in which the distance between the anode and cathode (distance d in figure 3.9) is equal to the separation between anode wires (S). This distance is fixed at 2.54 mm to provide the required performance. Precision co-ordinates are obtained by measuring the charge induced on the cathode by the avalanche formed on the anode wire. The gas mixture used in the chambers is composed of 80% argon and 20% carbon-dioxide. The lack of hydrogen in the gas-mix, coupled with the small gap width provides a low sensitivity to neutron backgrounds (less than 10^{-4}). Sensitivity to photons is expected to be of the order of 1%.

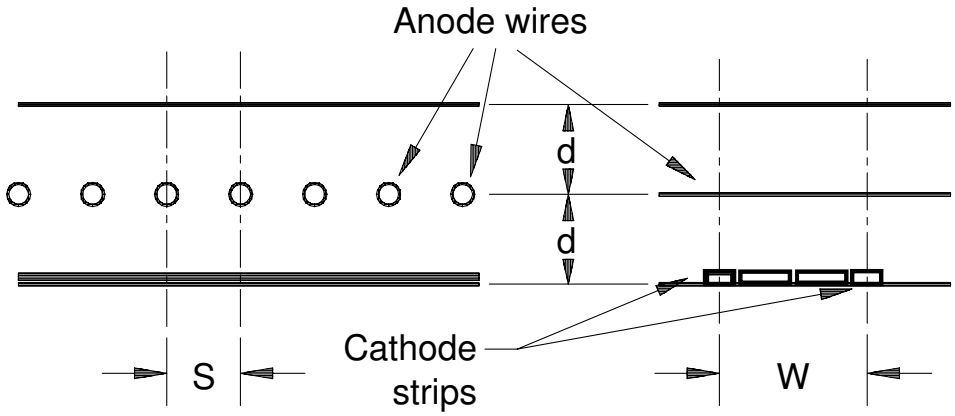

Figure 3.9: A schematic of a Cathode Strip Chamber [16].

3.3.3 RPC (Resistive Plate Chambers)

The RPC detector provides the trigger decision for the barrel region. It has an excellent time resolution of 1.5 ns (r.m.s.) which allows for identification of different bunch-crossings (the nominal LHC bunch spacing is 25 ns) and provides a fast and coarse measurement of the muon transverse momentum and tracking to identify hits in the precision chambers which are associated to the muon track.

The RPCs have a simple mechanical structure, consisting of a narrow gas gap formed by two parallel resistive Bakelite plates separated by insulating spacers 2 mm thick. The gas used is a mixture of 97% tetrafluoroethane ($C_2H_2F_4$) and 3% isobutane (C_4H_{10}) and has a total volume of 18 m^2. A trigger chamber is construced from two rectangular detector layers, each one read-out by two orthogonal series of pick up strips - one set running parallel to the MDT wires to provide track bending information, and the other running orthogonally to provide a second co-ordinate measurement which is also required for offline pattern recognition. The trigger logic uses both strips.

3.3.4 TGC (Thin Gap Chambers)

The TGC detectors provide trigger information in the endcap regions (up to $|\eta| < 2.4$). They take a similar design to multi-wire proportional chambers, but with the difference that the separation between anode wires (1.8 mm) is smaller than the anode-cathode separation (2.8 mm). The anode wires are arranged parallel to the MDT wires and provide the trigger information together with read-out strips arranged orthogonally to these. The read-out strips also provide a second co-ordinate for the measurement. The chambers are filled with a gas mixture of 55% carbon-dioxide and 45% n-pentane ($n-C_5H_{12}$). The electric field configuration and small wire-wire distance allow for a short drift time and as a result, good time resolution. 99% of incident muons will be detected within 25 ns allowing for reliable bunch-crossing identification.

3.4 Forward Detectors & Luminosity Monitors

In addition to the main bulk of the detector, three different additional detectors are used to make luminosity measurements. These are located at various points along the beam axis (z-direction) to provide information about the instantaneous and absolute luminosities received at ATLAS. Figure 3.10 shows the positions of each detector system, with respect to the interaction point (IP).

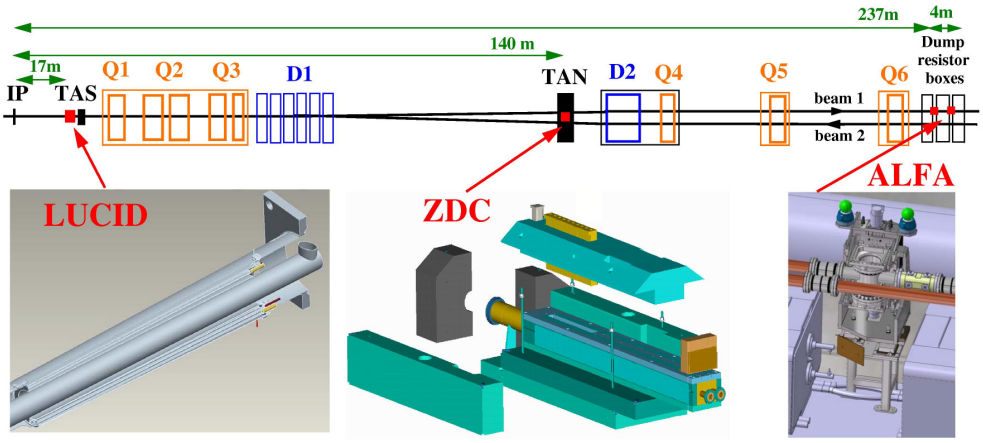

Figure 3.10: The ATLAS forward detectors: LUCID, ZDC and ALFA [17].

3.4.1 LUCID (LUminosity Cherenkov Integrating Detector

Two identical detectors, ± 17m in the z-direction from the interaction point are in place to make online measurements of beam conditions and instantaneous luminosity, from 10^{27} cm^{-2}s^{-1} to 4×10^{33} cm^{-2}s^{-1}. Each side consists of 16 Cherenkov tubes read out by a photomultiplier tube and 4 Cherenkov tubes read out by optical fibres. Coverage in the region $5.6 < |\eta| < 5.9$ is provided. Luminosity is monitored by counting the number of interactions per bunch in the Cherenkov counters.[18]

3.4.2 ZDC (Zero Degree Calorimeters)

The ZDC [19, 20] is located ±140 m from the interaction point, at the point where the straight section of the beam pipe splits back into two separate beam pipes. It is designed to detect neutral particles (neutrons, photons) with $|\eta| > 8.3$. In addition to providing luminosity measurements, during the start-up phase of the LHC ($p-p$ collisions with luminosities below 10^{33} cm^{-2}s^{-1}) the ZDC can enhance the acceptance for diffractive processes, and provide an additional minimum bias trigger. During heavy-ion collisions, the ZDC will play a key role in determining the centrality of events, since this is strongly correlated to the number of very forward (spectator) neutrons. The ZDCs reside in a slot in the TAN (Target Absorber Neutral) absorber, which would otherwise contain inert copper bars as shielding. Eventually, each side of the ZDC will contain one electromagnetic module (∼29 radiation lengths thick) and three hadronic modules (each ∼1.14 interaction lengths thick), but at the time of writing, only the hadronic modules were installed. Each module is composed of tungsten, with an embedded matrix of quartz rods which are observed by photomultiplier tubes.

3.4.3 ALFA - Absolute Luminosity For ATLAS

The ALFA sub-detector [18, 21] will provide absolute luminosity measurements, via elastic $p - p$ scattering at small angles (3 μrad). Although not yet installed, it will consist of four Roman Pot stations, two on each side of the interaction point at ±240 m. Each station will house two tracking detectors, each equipped with 1500 scintillating fibres. It will sit just 1 mm away from the beamline, and provide a spatial resolution of 30 μm.

3.5 Trigger

The nominal LHC collision rate will be 40 MHz, with a bunch spacing of 25 ns. At design luminosity (10^{34} cm^{-2}s^{-1}) there will be around 23 extra 'pile-up' events in each bunch crossing which will lie on top of the signal event. This provides an interaction rate of approximately 1 GHz, which exceeds the rate at which events can be recorded by a factor of 10^7. In order to reject uninteresting background processes (mostly low p_T QCD processes) and keep only those which are potentially interesting, a decision must be made very quickly whether or not to keep the event. Additionally, the trigger efficiency must be excellent and unbiased, so that the cross-sections of rare processes (*e.g.* $H \to \tau\tau$) can be measured. The process is carried out in three separate stages/levels - each one examining the event in more detail to assess its worth. An overview of the system is given in figure 3.11. [22]

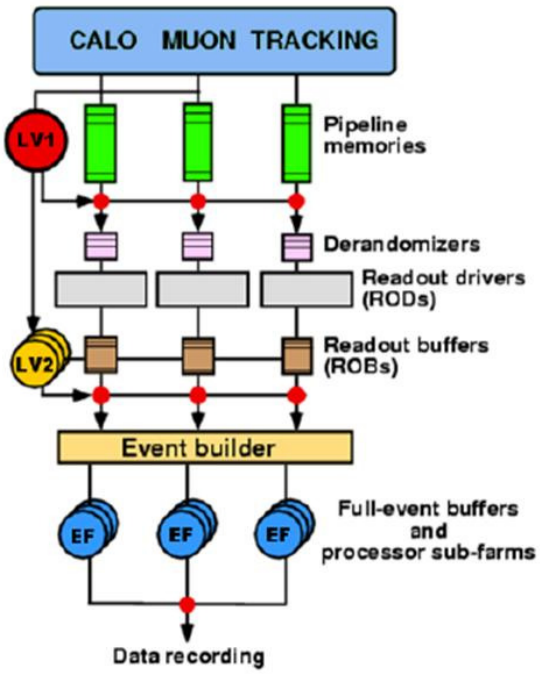

Figure 3.11: A schematic of the ATLAS trigger, from [22].

3.5.1 Level 1

The Level 1 trigger is a hardware trigger, based on coarse information from the tracking, calorimeter and muon detectors. Fragments of events are read out in parallel to look for the first indications of interesting signatures, such as the presence of a lepton. This first stage of rejection is carried out within 2.5 μs and reduces the bunch-crossing rate to 75 kHz.

3.5.2 Level 2

In the Level 2 trigger, only detector information in the region around the interesting feature flagged by Level 1 is read out. This has the advantage of reducing the amount of data which must be unpacked and analysed to $\sim$1-4% of the total data volume, saving time and computing power. The only exceptions to this are b-jet candidates, which require that large regions (or possibly all) of the detector are read out. The Level 2 trigger reduces the rate to $\sim$2 kHz and the average decision must be made within 40 ms.

3.5.3 Event Filter

The final stage of the trigger process uses the offline reconstruction algorithms to reconstruct the event in the same region of interest used in Level 2. The Event Filter is allowed $\sim$4 s to make its decision about whether or not to reject the event.

Chapter 4

Data Quality and the Detector Control System

An essential part of data taking at ATLAS is monitoring the status of the hardware components, and the quality of the data taken. An important component of this is the monitoring of the Detector Control System (DCS) which supervises detector components and can provide information about conditions inside the detector. Information from the DCS must be taken into account when making a decision about whether to use a given dataset for physics analysis.

4.1 Data Quality Monitoring Framework

The ultimate goal of the Data Quality Monitoring Framework (DQMF) [23] is to indicate whether or not a given luminosity block is deemed suitable for use in physics analysis. The various components of the DQMF all provide status flags to signal if the checks made on a given sub-detector (and thus the data taken from that detector) were satisfactory or not. Five status flags are available - each being represented by a colour (for graphical representations) or an integer (for database storage). The status flags are defined as follows:

- OFF (black, -1): Detector was not participating in data taking.

- UNDEFINED (grey, 0): Quality of data is not known, either as a result of insufficient statistics being available, or if information is missing.
- BAD (red, 1): Data cannot be used.
- CAUTION (yellow, 2): Data is flawed, but has issues which may be solved by further reprocessing.
- GOOD (green, 3): Data can be used for physics analysis.

Checks on the data quality come from several sources, both online (while a run is taking place) and offline (up to 24 hours after a run has finished). These include:

- Online automatic detector monitoring.
- Online shifter[1] checks of detector.
- Offline summarisation of DCS information
- Offline automatic detector monitoring.

Each method provides a status flag which is written to the offline database. These status flags are then combined automatically, taking the worst state. The last step is for the offline shifter (an expert from each sub-detector system) to review the decision. If they agree with the result they may do nothing. Otherwise, input from the expert offline shifter will override any of the automatic checks. This information is complemented by event displays which can provide 2-dimensional (Atlantis, [24]) and 3-dimensional (VP1, [25]) representations of events. These are not used to directly provide a status flag, but instead are used as tools to visualise and help understand individual events. A schematic of the ATLAS data quality monitoring framework is shown in figure 4.1.

[1]The detector must be monitored continuously during operation and routine manual checks of the detector are carried out by members of the collaboration, on a rotational basis throughout this time. The personnel carrying out these checks are referred to as 'shifters'.

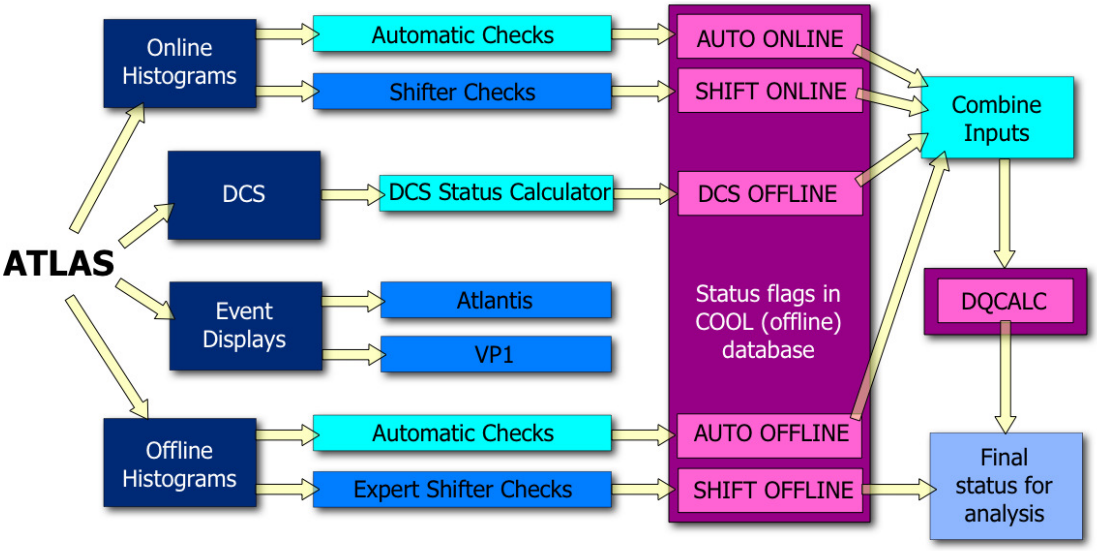

Figure 4.1: A schematic of the ATLAS Data Quality Monitoring Framework.

4.2 Detector Control System

The Detector Control System (DCS) supervises detector components and provides information about conditions inside the detector, for example temperature, state/status from the finite state machine (FSM)[2] or high voltage on a power supply. A full discussion of the DCS can be found in reference [27]. Some of these DCS quantities can affect the quality of data taken, and should therefore be monitored for use in the final data quality decision for data. Different quantities are useful for different sub-detectors and the DCS Status Calculator has been designed to accommodate this.

All DCS information from the detector is written to the ATLAS online database

[2]A finite state machine is a behavioural model composed of a finite number of states, transitions between those states and actions. It can be represented using a flow chart to inspect the way the logic runs when certain conditions are met [26]. FSMs are used to control the ATLAS DCS. Each FSM node is described by the 'STATE' and 'STATUS'. STATE reflects the operational mode of the system and can take one of three states - ON, OFF or STANDBY. STATUS provides information about how well the system is working and can be either OK, WARNING, ERROR or FATAL.

(PVSS Oracle Archive). Every 15 minutes a process (PVSS2COOL) is run to copy a sub-set of this data to the offline database. This is done via COOL [28] - an Application Programming Interface (API) for reading and writing conditions data, developed for use by LHC experiments. Conditions data, such as calibration, alignment or DCS, are non-event experiment data describing the state of the detector at the time of data taking, and are characterised by the fact that they vary in time and may have different versions. Once the information is available from COOL, the DCS Status Calculator can be run, to summarise the DCS status. A schematic of the flow of DCS information is shown in figure 4.2.

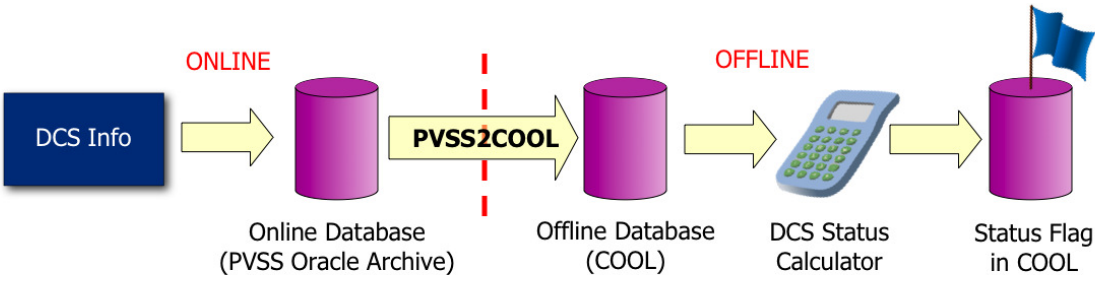

Figure 4.2: Flow of DCS information; From the detector to a summary status flag, via the online and offline databases.

4.3 DCS Status Calculator for Data Quality

The DCS Status Calculator summarises information from COOL folders to make a decision about the suitability of data for reprocessing. The number of luminosity blocks and the start and end times for a given run (Coordinated Universal Time (UTC) timestamps) are obtained from the database. This step is necessary because DCS information is indexed by timestamp, rather than run number/luminosity block. Following this, DCS information for each detector channel and also (if requested) the detector configuration is collected. Any number of DCS variables can be considered. A 5-bit bit-set is constructed for each channel,

with information about whether or not it was excluded from the run, and a status representing the combined DCS inputs. Finally, all the channels are considered together to provide a detector dead fraction, and based on this, a status flag, for each luminosity block. To minimise the amount of data written to and stored in the database, results for consecutive luminosity blocks are concatenated if the dead fraction (and therefore status) does not change. The process is depicted in figure 4.3.

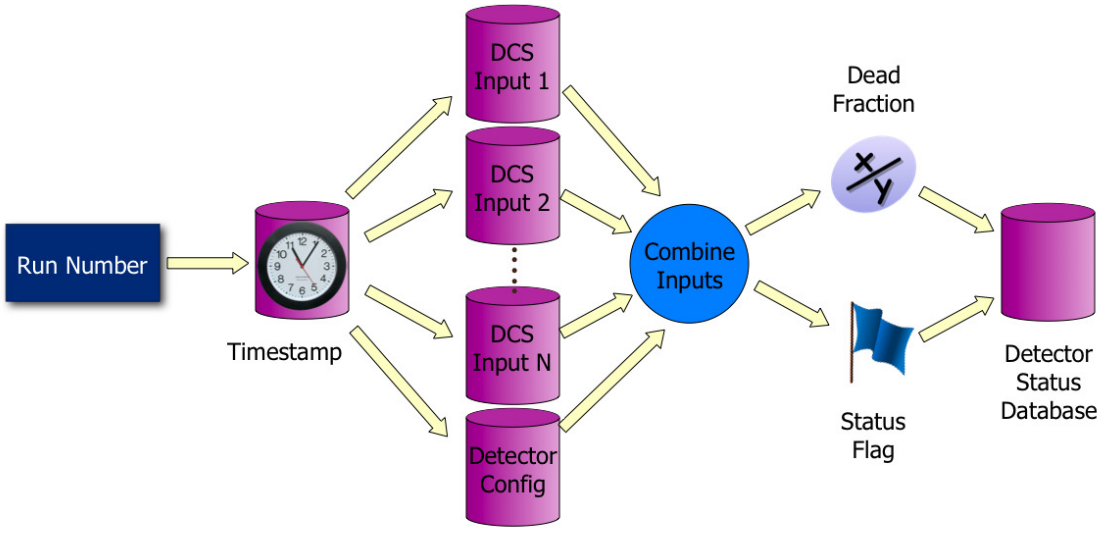

Figure 4.3: The DCS Status Calculator process: Once a run number is entered, the corresponding timestamps are obtained for each luminosity block. Then DCS information for each sub-detector channel is collected and compared with the detector configuration (if requested). Finally, these inputs are all combined and a detector 'dead fraction' and status are written to the database.

The framework for running the DCS Status Calculator automatically and a library of standard functions (e.g. converting run number to timestamp, reading information from the database, comparing different inputs etc) is provided and maintained centrally, leaving sub-detector groups with the freedom to configure the tool for their own system. There are two elements to the configuration. Firstly, an XML file containing database connection information, paths to folders, variable names, and criteria for that variable being GOOD/CAUTION and for

the detector to be GOOD/CAUTION/BAD. The sub-detector groups are also responsible for maintaining a second file, from which library functions are called. Any sub-detector specific functions (e.g. to look at detector configuration) are defined here too. The structure of the package is shown in figure 4.4.

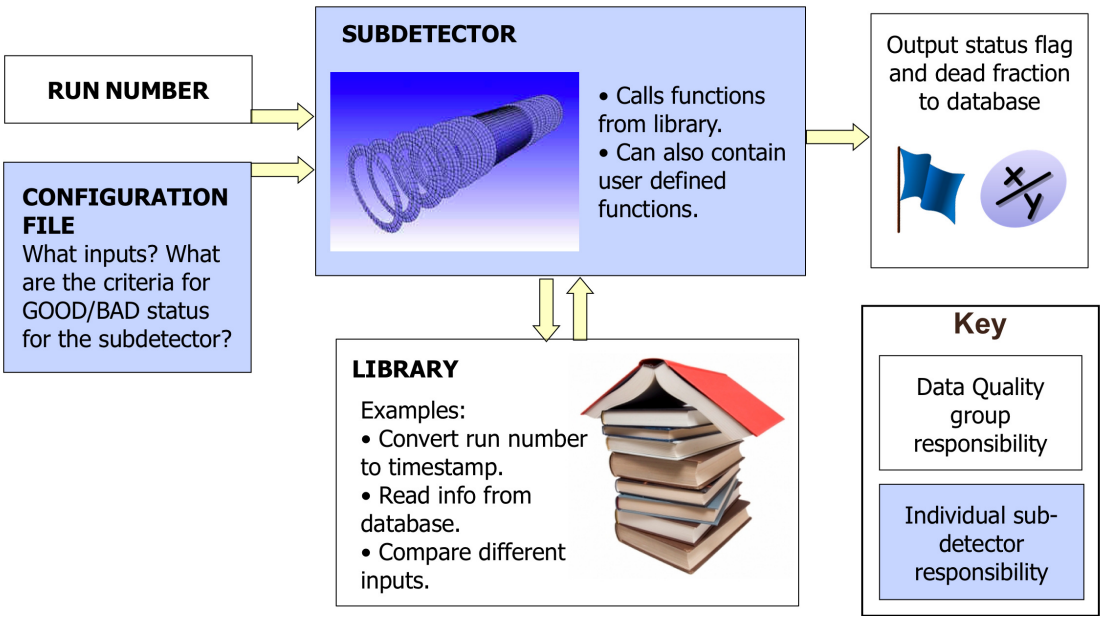

Figure 4.4: Structure of the DCS Status Calculator, showing the different components of the tool and where the responsibility for each lies.

4.3.1 DCS Calculator Sequence

The standard DCS Calculator sequence of events is as follows:

1. Read command line arguments to locate input configuration file(XML) and determine run number.

2. Parse the XML configuration file. The main information contained here is:

   (a) Unique 3-digit code identifying each sub-system (e.g. Pixel Barrel = 101).

   (b) Connection string for database where DCS information is stored.

(c) For each DCS input: The folder path, variable name, and set of criteria which describes the relationship between the input state and the output state. Each criterion can be set as one of two types:

- Bound: Specifies that the variable is a floating point number, and that its value should lie within the given range.
- Exact: Specifies the type of the value, and the exact value(s) which determine whether the result is GOOD, CAUTION or UNDEFINED. If the type does not match a 'known' type (one of int (I), unsigned int (U), float (F), string (S) or boolean (B)), the 'do-DCS-normally' flag is set to false. Users have the functionality to determine their own type here (e.g. bit comparison), but in these cases must provide a system specific function to evaluate them.

In addition, each variable name has an 'is-global' flag. If this flag is set then the overall status obtained from this variable will be applied to the entire sub-detector partition (i.e. if any individual channel is BAD (CAUTION) then the entire partition will be flagged as BAD (CAUTION), even if all other channels are GOOD).

(d) Flag to indicate whether or not detector configuration information should be taken into account. If it is then the database connection string, folder path and variable name, plus information for decoding the included/not included state are specified.

(e) Output database connection string (either the real 'Detector Status' database or an SQLite [29] copy of this, for testing purposes), path to folder, the threshold above which too many channels are 'dead' and the result is BAD, and a lower threshold, above which the result is CAUTION.

3. Obtain start and end timestamps for each luminosity block. This information is extracted from a folder in the database maintained by the trigger

group. It is indexed by run number and luminosity block, and contains the UTC timestamps of the start and end times for each one. There is no way for the DCS Calculator to know the number of luminosity blocks in a given run a priori, and so it must iterate through all entries until it reaches the last luminosity block. After this point queries to the database for luminosity blocks which do not exist will return the times of the last listed luminosity block. The DCS Calculator uses this repetition of returned data to determine the last 'real' luminosity block. Timestamps are stored in a list for later use. If no entries are found for a given run number then it is assumed that this run is not an ATLAS run (i.e. the data taken will not be processed or used for analysis) and the DCS Calculator exits.

4. Determine the configuration for the detector. At the most basic level this requires reading a text file to tell the DCS Calculator what channels it should be looking at and if it's included in the configuration or not. These are stored in a map which has the COOL channel ID as the key and a 1 or 0 (to indicate it's inclusion or exclusion respectively) as the value. The default value is 1 (i.e. tell the DCS Calculator to assume that every channel is included in the configuration), but if desired, sub-detector specific functions can be included to read the actual configuration for that run/luminosity block from the database and adjust the map values accordingly.

5. For each of the DCS inputs specified in the XML configuration file, the status is assessed for each individual channel and for each luminosity block to see if the channel passed the DCS requirements. If the Calculator detects that there are empty fields in the database then a warning flag is filled, a warning message output to the log file, and the status set to UNDEFINED. For each luminosity block, a temporary map of the COOL channel ID (key) and DQ status (value) is filled using the standard DQ colour-integer coding (see section 4.1). If a channel changes status within the same luminosity

block, the worst status is taken (even if the channel later recovers within the same luminosity-block). At the end of each luminosity block, information from this temporary map is added to another map containing the COOL channel ID (key) and a vector of statuses, where each vector element represents the channel's DCS status for a given luminosity block. A visualisation of this map is shown in figure 4.5. This process is repeated for every DCS variable input in the XML configuration file.

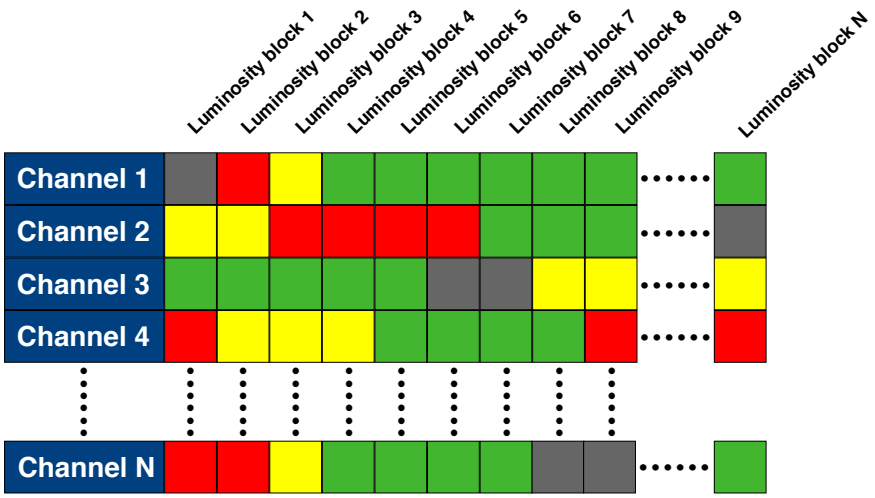

Figure 4.5: A graphical representation of the mechanism for storing DCS status results for individual channels and luminosity blocks; a map with the COOL channel ID as the key, and a vector representing the DCS status for each luminosity block as the value.

6. The final status for each channel is determined, by assessing the status from each variable for that channel and taking the worst case. This summary status is stored for every channel and then compared with the detector configuration. Finally, for each channel and each luminosity block a bit-set is recorded which represents the final summary state.

- Bit 0 Does the channel exist (i.e. should there be records for it in COOL)?
- Bit 1 Was the channel included in the detector configuration?
- Bit 2 Was the DCS status for that channel GOOD?
- Bit 3 Was the DCS status for that channel CAUTION?
- Bit 4 Was the DCS status for that channel BAD?

If bits 0 and 1 are = 1 but bits 2, 3 and 4 are all = 0 then the DCS status is UNDEFINED.

7. For each luminosity block the bit-sets generated in the previous stage are read and the detector 'dead fraction' is calculated (where dead fraction = number of channels which failed DCS or not in configuration / total number of channels in the detector). Unless 100% of the detector has the same final status (e.g. as a result of a DCS variable being declared global), the final overall status for the partition for that luminosity block is determined by comparing the dead fraction with the limits set in the xml configuration file (see item 2e). The dead fraction and final status, plus the total number of channels that exist and the total number and fraction of channels that are a) included in the run, b) in a GOOD state, c) in a CAUTION state, d) in a BAD state and e) in an UNDEFINED state are stored together with their interval of validity (encoded run number/luminosity block). If the warning flag indicating that information was missing in the database has been filled then this is also stated. If all of these values remain unchanged for subsequent luminosity blocks then the end value of the interval of validity is updated. Otherwise a new entry is recorded. This information is output to the log file.

8. Finally, the dead fraction, status code, number of channels included in the detector configuration and number of channels passing the DCS require-

ments are written to the 'DCS Offline' folder in the Data Quality group 'Detector Status' database, together with the interval of validity (encoded run number/luminosity block).

4.3.2 Sub-detector Configuration

DCS Calculator set-up and configuration details are given below for each sub-detector system and the level 1 trigger hardware. A short description of each sub-system can be found in section 3.

4.3.2.1 Pixel Detector

Assesses the Finite State Machine (FSM) State and Status for the *b*-layer (innermost barrel layer), the barrel and each of the two endcaps. Channels are deemed GOOD if State = 'OK' and Status = 'READY'. The final DCS status is GOOD if the detector dead fraction is less than 20%, CAUTION if the dead fraction is between 20% and 90% and BAD if more than 90% of the detector has failed the DCS requirements.

4.3.2.2 SCT

A bit comparison is carried out on a byte representing the FSM Status (recorded as an unsigned integer in COOL) to check for trips on the high and low voltage power supplies. A full description of this byte can be found in [30]. In addition, the high voltage on each silicon module must be between 55 and 3000 V.

The SCT configuration is accessed by querying a COOL folder to obtain a key, which is then used to look up the configuration information in a CORAL table. This set-up allows a single COOL entry to reference several payload table rows, or several COOL entries to reference the same row (i.e. a single object in COOL can be valid for many separate intervals of validity)[31].

The DCS status is evaluated for each of the two endcaps and the barrel. The status is deemed GOOD if less than 10% of modules fail the DCS requirements or

are not included in the run configuration, CAUTION if the detector dead fraction is between 10% and 50%, and BAD if more than 50% of the detector fails.

4.3.2.3 TRT

The high voltage on groups of straws must be between 1400 and 3000 V for the DCS status to be GOOD. The status is evaluated for each of the two endcaps and the barrel and is GOOD if the detector dead fraction is less than 5%, CAUTION if it is between 5% and 20% and BAD otherwise.

4.3.2.4 LAr Calorimeter

The FSM State is used as a global variable to decide the status of each LAr partition (two electromagnetic barrels, two electromagnetic endcaps, two hadronic endcaps, two hadronic forward detectors). This must be 'READY' for the status to be GOOD. If State = 'UNKNOWN' or 'DEAD' then the status is CAUTION. Otherwise the partition is flagged as BAD.

4.3.2.5 Tile Calorimeter

The tile calorimeter status is determined from the statuses of the tile modules, each of which contains several photomultiplier tubes (PMTs). An individual module is defined to be GOOD if the following requirements are met.

- All PMTs in the module have the correct high voltage (HV) across them and are in a 'READY' state.
- There must be communication with the PMT read-out electronics.
- The low voltage (LV) for the module motherboard is on and in a 'READY' state.
- The LV supply for the HV distributor system is on and in a 'READY' state.

A DCS DQ flag is written for each of the four partitions (two barrels and two endcaps). Each partition consists of 64 modules. More than 97% of modules must pass the DCS requirements in order for the partition to be flagged as GOOD. If less than 97% but more than 25% of moduless pass, the partition is flagged as CAUTION, otherwise it is marked BAD.

4.3.2.6 MDT

DCS DQ flags are written for each of the four regions of the MDT detector system – the $+z$ and $-z$ regions of the barrel, and each of the endcaps. Three separate DCS variables are considered by assessing the FSM States of the following:

- High voltage (HV) power supplies for multi-layers; GOOD if State = 'ON'.
- Low voltage (LV) power supplies for read-out electronics; GOOD if State = 'ON'.
- Front-end electronics and read-out chain; GOOD if State = 'INITIALIZED'.

Since each variable has a different granularity, the mapping of each of these variables to the others is stored in a text file. The multi-layers provide the finest level of granularity in the system and so the DCS Calculator uses the same granularity as the HV. A list of the names of chambers which have been dropped from the run are stored as a string in the DCS database. To determine the detector configuration, this string is parsed to obtain individual channel names, which are then mapped to the HV channels.

The DCS status is evaluated for each of the two barrels and two endcaps, and is flagged as GOOD if the detector dead fraction is less than 10%, CAUTION if the dead fraction is between 10% and 50% and BAD otherwise.

4.3.2.7 CSC

The following items are considered when assessing the DCS DQ decision for the CSC detectors:

- Gas state; The gas mixture in the chambers should be 80% argon and 20% carbon-dioxide. A chamber is GOOD if the gas mixture stays at this ratio, and BAD if the composition changes.
- Power supply high voltage (HV): If the HV is at nominal voltage then the channel is deemed GOOD.
- Power supply low voltage (LV): If the LV is on then the channel status is GOOD.

Flags are written for each of the CSC endcap detectors. The gas state is a global variable, *i.e.* if any chamber fails then the entire partition is flagged as BAD. Assuming this is not the case, a partition is flagged as BAD/CAUTION if more than 80%/50-80% (respectively) of channels have failed the HV or LV requirements. Otherwise, the partition is GOOD.

4.3.2.8 RPC

An individual trigger tower (projection of the detector) is flagged as GOOD if it meets the following requirements:

- All low voltage (LV) channels are on.
- 75% of middle layer chambers have high voltage (HV) on and in a 'READY' state.
- 50% of outer chambers have HV on and in a 'READY' state.
- The trigger electronics have been initialised.
- The trigger tower has not been masked off, and is not busy.

To be flagged as good, each RPC partition (two sides of the barrel, $\pm z$) is flagged as GOOD if at least 90% of trigger towers are GOOD. If less than 70% of towers pass the DQ requirements then the partition is BAD, otherwise a CAUTION state is returned.

4.3.2.9 LUCID

Two DCS status flags are provided for LUCID - one each for the detectors at the positive and negative z sides of the interaction point. To be flagged as GOOD, LUCID must meet the following requirements:

- All high voltage (HV) channels connected to the photomultiplier tubes (PMTs) in the detector must be on and the voltage across them must be within $\pm$ 5 V of the set value.
- The low voltage (LV) channels connected to the read-out chain (signal amplifiers, back-end electronics and LEDs used for calibration) are assessed in the same way as the PMT HV lines. The LV input is a global variable, so if any channel fails the requirements the entire partition is flagged BAD..
- The status of both ATLAS magnets is also taken into account since a varying magnetic field can interfere with the luminosity measurements. Both magnets must be in a steady state (*i.e.* either completely off, or on and running with the correct current - see section 4.3.2.11 for more details).

A CAUTION state will be triggered if one or more (but not all) PMT HV channels fail. If all PMT HV channels fail then the detector is flagged as BAD. A flag indicating whether or not the magnet information in the database can be fully trusted is also read from COOL. This is considered in the LUCID calculation and if this indicates that there may be a problem, the DCS Calculator will return an UNDEFINED state. In this way, the offline shifter can be alerted to the problem and the final DQ decision can be resolved to a GOOD/CAUTION/BAD state by considering other online and offline assessments.

4.3.2.10 Level 1 Trigger

The Level 1 Trigger systems monitor many different DCS variables (*e.g.* component temperatures, voltage levels), but if any of these go outside of the acceptable range then the power supply crates are powered off. The overall status can therefore be extracted by simply reading the crate power status which is stored in COOL as a boolean ('TRUE' = Power On, 'FALSE' = Power Off). The final status for each partition (Central Trigger Processor, Level 1 Muon trigger (barrel and endcaps are treated separately), and Level 1 Calorimeter trigger) is GOOD if all crates have a 'TRUE' status, and BAD otherwise. CAUTION states are never returned.

4.3.2.11 Magnets

A DCS status flag is written for each of the magnets (the solenoid surrounding the inner detector and the toroid outside the calorimeters), although the calculation is performed in much the same way for both. The measured and set currents for each magnet are recorded in COOL and a comparison is then made to determine a preliminary status which can take any of the following values;

- OFF: The measured current and set current are both zero.
- OK: The measured current and the set current are equal, with a tolerance of $\pm$ 5 A for the solenoid and $\pm$ 10 A for the toroid, but not zero.
- RAMPING: The measured current is not equal to the set current ($\pm$ tolerance).
- INVALID: A status flag indicating whether or not the data can be fully trusted is also assessed. If there is the possibility that the data may have been corrupted in any way (*e.g.* through a temporarily lost connection) then the magnet is flagged as 'INVALID'. This status overrides all others.

If the magnet status is 'OFF' a black/OFF DCS DQ flag is written. This is the only instance of the DCS Calculator writing an OFF flag, since this cannot be determined with 100% accuracy from COOL data for other detectors (although an educated guess can be made). Assuming a non-OFF status, the overall DCS status of the magnet is deemed to be GOOD if the magnet status is 'OK', UNDEFINED if the status is 'INVALID' and BAD otherwise.

4.3.3 Automatic Running

The ATLAS DQ group provides a set of standard functions which can be used to retrieve information about runs. The DCS Calculator makes use of one of these, which, given an input run number, provides a list of all runs which meet the following criteria:

1. Have a run number $\geq$ input run number.
2. Are 'ATLAS-partition' runs (*i.e.* all sub-systems are included and running in a data-taking configuration) or don't have a DAQ partition set (*i.e.* the run was not flagged as having only a subset of sub-systems (*e.g.* the inner detector components) running, for calibration and testing purposes).
3. Are not 'test' runs.
4. And either:
   (a) Have an 'end-of-run' timestamp, or
   (b) Have a run number which is less than the highest numbered ATLAS-partition run (this only gets set at the end of a run).

This function is called every 30 minutes. Precautions are taken to ensure that runs have finished and that sufficient time for all information to be written to COOL has elapsed before the DCS Calculator starts to run.

4.4 Viewing Output

The status flags output by the DCS Status Calculator can be easily viewed using standard ATLAS tools, including a web-based database browser. An example of the database browser is shown in figure 4.6. This tool is widely used within the Data Quality group to browse database entries from all data quality inputs (online and offline automatic checks and shifter inputs), as well as the DCS results.

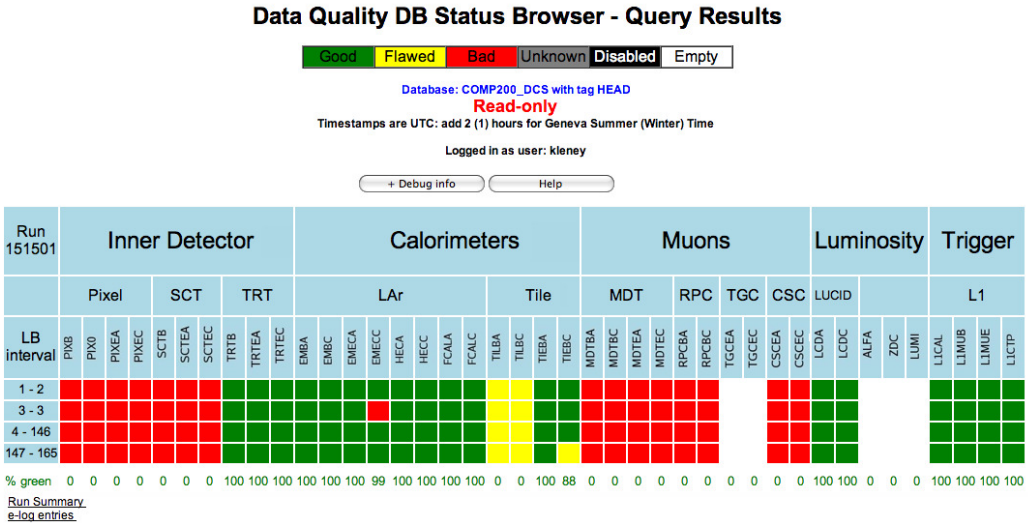

Figure 4.6: Data quality results can be viewed online using a database browser. By calculating the status per luminosity block, rather than per run, data from a sub-detector is not unnecessarily discounted if just a small fraction of it is deemed unsuitable for use in physics analysis.

4.5 Combination of Flags into Final Summary

Once all data quality flags (online and offline automatic checks, online shifter checks, and DCS) have been filled, the 'worst-case' is propagated through to provide a final DQ status flag. Checks are made by offline shifters (data quality experts) from each sub-detector system who then have the possibility to overwrite

the DQ result if necessary.

4.6 Physics Performance Flags

Once the final flags are filled, they are made available to physics performance groups, who each require that certain detectors be flagged as 'GOOD' in order for the data to be suitable for analysis involving their particular object of interest (e.g. electrons, muons). In addition to the different requirements made by each performance group there are flags which are of global interest, for example those which signal failures by the Central Trigger Processor hardware. These are combined into a single flag 'ATLAS Global DQ' which should be demanded to be 'GOOD' by all analyses.

4.6.1 Data Quality Requirements for Hadronic Taus

Hadronic taus are characterised by narrow, well-collimated energy deposits in both calorimeters, matched to one or three tracks in the inner detectors (see section 5.3.1 for more details). Consequently, tau identification requires that the entire inner detector and both calorimeters have all been marked as 'good' for data quality.

Once enough data has been accrued to optimise the boundaries, three different flags will be provided for taus, corresponding to different pseudorapidity regions in the detector - the central (barrel) region, an extended (forward) region, and the crack region (around $|\eta| = 1.4$). Until then, just one flag is provided, which is valid at any η position [32].

4.7 Summary and conclusion

A framework for summarising DCS information on a per luminosity block and per sub-detector basis has been implemented and has been running successfully

since September 2008. It is now used by all of the ATLAS sub-detector systems which are taking data and the level one trigger. The only exceptions to this are ALFA and ZDC (these systems do not yet have a fully operational DCS system implemented), and the TGC muon detectors (where DCS data is not written to COOL). The summaries provided by the DCS Status Calculator contribute to the final data quality status flag to indicate a run's suitability for physics analysis.

Chapter 5

Object Reconstruction, Identification and Trigger

5.1 Electrons

Electron candidates are formed by searching for a cluster of cells in the electromagnetic calorimeter matched to a track in the inner detector. The full electron identification algorithms take into account the shape of the shower, tracking information, and consistency between the track and the cluster. Candidates must be within $|\eta| < 2.47$, but not in the 'crack' region between the barrel and endcap regions of the calorimeter ($1.37 < |\eta| < 1.52$). In addition, candidates must pass the 'medium' criteria as defined in reference [9]. Fractional isolation requirements are made by demanding:

$$\frac{E_T^R - E_T^e}{\Sigma p_T} < X \tag{5.1}$$

Where E_T^e is the transverse energy (E_T) associated with the electron candidate, E_T^R is the E_T in a cone of radius R around the cluster, and Σp_T is the sum p_T of all tracks associated with the object. Typical values for R and X are of the order 0.2 and 0.1 respectively.

5.2 Muons

With a mean lifetime of 2.2×10^{-6} s [33], muons can effectively be treated as stable particles in the ATLAS detector. They will be the only (detectable) particles which will pass through both calorimeters and interact with the muon detectors. Following the recommendations of the ATLAS muon performance group, muons are reconstructed using the STACO combined algorithm (described in [9]), where muon-spectrometer tracks are combined with an inner detector track. Quality requirements are made and muon candidates must fall within the $|\eta| < 2.5$ range. Fractional isolation requirements are imposed in the same way as for electrons.

5.3 Taus

The mean lifetime of the tau lepton is 290.6×10^{-15}s [33] (corresponding to a distance of approximately 87 μm in the detector), after which, it will subsequently decay to either the lighter electron or muon plus two neutrinos, or to hadrons plus one neutrino. Schematics of tau decays to a lepton and to a single pion are shown in figure 5.1.

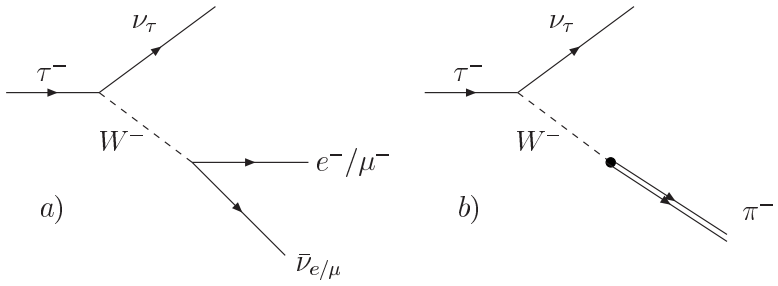

Figure 5.1: a). Leptonic tau decay. b). Tau decay to a single pion.

The hadronic final states predominantly involve charged pions, although there are a small proportion ($\sim 2.5\%$) of events where the hadron is a charged kaon. These states can be accompanied by several neutral pions or neutral kaons (although the latter has a much smaller branching fraction). Single prong/track

τ^- Decay Type	Branching Ratio (%)	Decay Mode	Branching Ratio (%)
Leptonic (τ_e/τ_μ)	35.3	$e^-\bar{\nu}_e\nu_\tau$	17.9
		$\mu^-\bar{\nu}_\mu\nu_\tau$	17.4
Hadronic (τ_h): 1-prong	48.6	$\pi^-\nu_\tau$	10.9
		$\pi^-\pi^0\nu_\tau$	25.5
		$\pi^-2\pi^0\nu_\tau$	9.3
		$\pi^-3\pi^0\nu_\tau$	1.1
		$K^-\nu_\tau$	0.7
		$K^-\pi^0\nu_\tau$	0.5
Hadronic (τ_h): 3-prong	15.2	$\pi^-\pi^+\pi^-\nu_\tau$	9.3
		$\pi^-\pi^+\pi^-\pi^0\nu_\tau$	4.6

Table 5.1: Main tau decay modes (adapted from [33]).

events account for approximately 85% of all hadronic tau decays. The main tau decay modes (branching ratio $\geq$ 0.5%) are summarised in table 5.1.

5.3.1 Hadronic Tau Identification

Hadronic tau decays (*e.g.* to pions) are identified by searching for narrow, well collimated energy clusters in the calorimeters, which are associated with one or three tracks.

Two complementary algorithms for tau ID are used in the ATLAS offline reconstruction software, one is seeded from a track, while the other is seeded from a cluster in the calorimeter. Both methods are described briefly below.

- **Calorimeter Seeded:**

  The calorimeter based algorithm uses clusters in the electromagnetic and hadronic calorimeters with $E_T > 10$ GeV as the seed.

- **Track Seeded:**

  In this approach, a track with $p_T > 6$ GeV that satisfies quality criteria on the number of associated hits in the silicon layers, and on the impact parameter with respect to the interaction vertex is used as the seed. Tracks that are associate to each tau candidate in a cone of ΔR =0.2 around the

seed axis are also required to pass similar quality criteria as the seed track. The tau candidate is said to be n-pronged if there are n tracks associated to it [34].

In both cases, the variables used in the identification process are built on information from the tracker and the calorimeter once the seed has been found. Tau candidates will then be selected by applying multi-variate discrimination techniques. Full details can be found in reference [9]. A fully optimised tau identification will only be possible once both calorimeters and all tracking detectors (see chapter 3) are completely calibrated and well understood. Until then a 'safe' cut-based tau ID using only the most robust identification variables will be used.

5.3.2 Hadronic Tau Identification in Early Data

During the early data-taking period (up to $\sim$500 pb^{-1} integrated luminosity), a cut-based tau ID using only 'safe' variables will be used. This 'safe tau-ID' will have two stages - the first (and most robust) will use only information from the calorimeter, whilst the second will use these calorimeter variables, plus information from the tracking detectors once these are understood and the requisite variables validated. A full discussion of tau identification using safe variables at ATLAS can be found in reference [34], but is summarised below for convenience.

5.3.2.1 Calorimeter Only

During very early data-taking periods, tau identification will be based solely on the following calorimeter variables.

- **Electromagnetic radius**

  The electromagnetic radius R_{EM} is defined to be:

$$R_{EM} = \frac{\sum_{i=1}^{\Delta R<0.4} E_{T,i}^{EM} \sqrt{(\eta_i^{EM} - \eta_{cluster})^2 + (\phi_i^{EM} - \phi_{cluster})^2}}{\sum_{i=1}^{\Delta R<0.4} E_{T,i}^{EM}}$$

where i runs over all cells in the EM calorimeter associated to the tau candidate cluster. $E_{T,i}^{EM}$ is the transverse energy in cell i, while the co-ordinates of this cell are given by η_i^{EM} and ϕ_i^{EM}. The co-ordinates of the tau candidate cluster are given by $\eta_{cluster}$ and $\phi_{cluster}$.

- **Isolation fraction**

  Since hadronic tau decays are well collimated, tight isolation criteria can be imposed. An isolation fraction f_{iso} is defined:

$$f_{iso} = \frac{\sum_{i}^{0.1<\Delta R<0.2} E_{T,i}^{EM}}{\sum_{j}^{\Delta R<0.4} E_{T,j}^{EM}}$$

  where the indices i and j run over the EM cells in cones around the tau candidate cluster axis of $0.1 < \Delta R < 0.2$ and $\Delta R < 0.4$ respectively. $E_{T,i}$ and $E_{T,j}$ represent the transverse energy in the cells.

- **Ratio of EM energy and total energy**

  The ratio of energy deposited in the EM calorimeter to the total energy (E_T^{EM}/E_T^{total}) is defined as:

$$\frac{E_T^{EM}}{E_T^{total}} = \frac{\sum_{i}^{\Delta R<0.4} E_{T,i}^{EM}}{\sum_{i}^{\Delta R<0.4} E_{T,i}^{EM} + \sum_{j}^{\Delta R<0.4} E_{T,j}^{had}}$$

  where the sums run over all cells in a cone of $\Delta R < 0.4$ around the tau candidate cluster axis, $E_{T,i}^{EM}$ is the cell energy in the EM calorimeter, and $E_{T,j}^{Had}$ is the energy in the hadronic calorimeter.

- **Transverse energy width in the η strip layer**

  The transverse energy width (W_{strip}) in the η-strip layer (first layer of the

EM calorimeter) is defined as:

$$W_{strip} = \sqrt{\frac{\sum_{i}^{\Delta R<0.4} E_{T,i}^{strip}(\eta_i - \eta_{caloseed})^2}{E_{T,i}^{strip}}}$$

where the sum runs over all strip cells in a cone of $\Delta R < 0.4$ around the tau candidate cluster axis and $E_{T,i}^{strip}$ is the corresponding strip transverse energy.

5.3.2.2 Calorimeter + Tracking

Once enough data has been accrued, the following variables which incorporate tracking information will be validated and then incorporated into the tau-ID, together with those described above.

- **Ratio of total $\mathbf{E_T}$ to $\mathbf{p_T}$ of leading track**

  A large fraction of the energy is expected to be carried by the leading track, and the ratio of the total transverse energy in the cluster to the transverse momentum of the leading track is expected to be large (close to 1). This ratio ($E_T^{total}/p_{T,1}$) is defined to be:

$$\frac{E_T^{total}}{p_{T,1}} = \frac{\sum_{i}^{\Delta R<0.4} E_{T,i}^{EM} + \sum_{i}^{\Delta R<0.4} E_{T,i}^{had}}{p_{T,1}}$$

  where $E_{T,i}^{EM}$ and $E_{T,i}^{Had}$ are the transverse energies of the cells in a cone of $\Delta R < 0.4$ around the tau candidate in the EM and hadronic calorimeters, respectively, and $p_{T,1}$ is the transverse momentum of the highest p_T track associated to the tau candidate.

- **Ratio of EM $\mathbf{E_T}$ to summed $\mathbf{p_T}$ of tracks**

The ratio $E_T^{EM}/\Sigma p_T^{track}$ is defined to be:

$$\frac{E_T^{EM}}{\Sigma p_T^{track}} = \frac{\sum_{i}^{\Delta R<0.4} E_{T,i}^{EM}}{\sum_{j=1}^{N} p_{T,j}^{track}}$$

where $E_{T,i}^{EM}$ is the energy of cells in the EM calorimeter in a cone of $\Delta R < 0.4$ around the tau candidate cluster axis, and the sum in the denominator runs over the transverse momenta p_T^{track} of the $N = min(n, 3)$ highest p_T tracks associated with the n-prong tau candidate.

- **Ratio of hadronic $\mathbf{E_T}$ to summed $\mathbf{p_T}$ of tracks**

  The ratio $E_T^{had}/\Sigma p_T^{track}$ is defined to be:

$$\frac{E_T^{had}}{\Sigma p_T^{track}} = \frac{\sum_{i}^{\Delta R<0.4} E_{T,i}^{had}}{\sum_{j=1}^{N} p_{T,j}^{track}}$$

  where $E_{T,i}^{had}$ is the energy of cells in the hadronic calorimeter in a cone of $\Delta R < 0.4$ around the tau candidate cluster axis, and the sum in the denominator runs over the transverse momenta p_T^{track} of the $N = min(n, 3)$ highest p_T tracks associated with the n-prong tau candidate.

- **Ratio of summed $\mathbf{p_T}$ of tracks and total energy**

  The ratio $\Sigma p_T/E_T^{total}$ is defined as:

$$\frac{\Sigma p_T}{E_T^{total}} = \frac{\sum_{k=1}^{N} p_{T,k}^{track}}{\sum_{i}^{\Delta R<0.4} E_{T,i}^{EM} + \sum_{j}^{\Delta R<0.4} E_{T,j}^{had}}$$

  where the sum in the numerator runs over the p_T of the $N = min(n, 3)$ highest p_T tracks associated with the n-prong tau candidate, $E_{T,i}^{EM}$ and $E_{T,j}^{total}$ are the cell energy in the electromagnetic and hadronic calorimeters, respectively.

- **Track spread**

  For multi-prong tau candidates, the spread of tracks (weighted by p_T) in η, ϕ-space (W^{τ}_{track}) is defined as:

$$W^{\tau}_{track} = \frac{\Sigma(\Delta R^{track})^2 \cdot p_T^{track}}{\Sigma p_T^{track}} - \frac{(\Sigma \Delta R^{track} \cdot p_T^{track})^2}{(\Sigma p_T^{track})^2}$$

  where ΔR^{track} is the distance between the track and the tau candidate seed track in η, ϕ-space and the summation is performed over all tracks associated to the tau candidate.

Three sets of cuts were determined for the calo-only and calo+tracking algorithms to provide different levels of hadronic tau selection efficiency. These are designated loose ($\epsilon = 70\%$), medium ($\epsilon = 50\%$) and tight ($\epsilon = 30\%$). Cuts were optimized separately for zero or one track candidates and for those with two or more tracks. In addition, the variables were optimised over five visible transverse energy (E_T^{vis}) bins (10-25 GeV, 25-45 GeV, 45-70 GeV, 70-100 GeV and $\geq$ 100 GeV). Rejection rates vary from 0.13 to 140, depending on the p_T of the tau candidate, and whether the loose, medium or tight selection is used. Detailed studies can be found in reference [34].

Thus there are six options for safe tau-ID during the early data taking period. Three using only calorimeter information:

- TauCutSafeCaloLoose
- TauCutSafeCaloMedium
- TauCutSafeCaloTight

and three using both calorimeter and tracking variables:

- TauCutSafeLoose
- TauCutSafeMedium
- TauCutSafeTight

5.3.3 Analysis Level Cuts

In addition to the tau ID flags provided using the official requirements, extra cuts are made at the analysis stage to enhance the signal-to-background ratio further.

- One or three tracks: Hadronic tau decays should have one or three prongs ∼99% of the time (5-prong decays are also possible, but the small branching ratio coupled with the difficulties differentiating these decays from QCD backgrounds makes their reconstruction unfeasible). In reality, the track reconstruction is not ideal and there is a proportion of events where two tracks are associated to the tau – either because one track is missed (in the case of a 3-prong event) or because an extra track is associated to the event (in a one-prong decay). Although there is this contribution from two-track candidates, the contribution from QCD events in the two-track bin is many times larger (proportionally) than in the one and three-track bins. Requiring only one or three track candidates therefore improves the acceptance-rejection ratio of signal and background events.

- Charge: The charge of the tau candidate should be ± 1.

- Electron Veto: Contamination from electrons (*e.g.* from $W \to e\nu_e$ or $Z \to ee$ decays) is reduced by making cuts on the ratio of the E_T deposited in the electromagnetic calorimeter to the p_T of the lead track, and the ratio of the number of high threshold hits to the number of low threshold hits in the TRT.

- Muon Veto: Fakes from muons are rejected by requiring that at least 10 GeV of energy has been deposited in the calorimeters.

5.4 QCD Jets

The starting point for jet reconstruction is an energy deposit (cluster) in the calorimeter. Clusters are identified using the 'Topological' (Topo) cluster algorithm which reconstructs clusters in three dimensions. The found cluster then serves as a seed for jet reconstruction, using a cone of $\Delta R = 0.4$ around the seed. Two jet reconstruction algorithms are used at ATLAS - the 'Cone' algorithm and the 'Anti-k_T' [35] algorithm.

5.5 Missing E_T

Neutrinos will pass straight through the detector without interacting, but their presence can be inferred by looking for an imbalance in energy deposition in the plane transverse to the beam direction. Since the colliding protons do not have a transverse component of their momentum, the summed momenta of all decay products (including neutrinos) should vanish as well. The sum of the transverse momenta of the visible decay products should therefore be equal to the negative sum of the transverse momenta of the neutrinos. The visible transverse energy is calculated from the energy deposited in each of the calorimeters, and from muons. Corrections are made for known sources of energy loss in inactive material, such as the Liquid Argon Calorimeter cryostat walls.

5.6 Overlap Removal

It may be possible that one object may pass the identification requirements for more than one type of particle. For this reason, an order of precedence is defined amongst the object types (muon, electron *etc.*) and any candidates which overlap with a higher precedence candidate are rejected. Overlap removal is performed in the order muon, electron, tau, jet, defining a cone of radius $\Delta R = 0.2$ to be the overlap region.

Chapter 6

Vector Boson Fusion Higgs to Tau Tau Search Strategy

6.1 Introduction

In this chapter Higgs boson production via vector boson fusion (VBF) and its subsequent decay into two tau leptons is considered and the background contribution from $t\bar{t}$ decays is evaluated using Monte Carlo simulations with a centre-of-mass energy of 14 TeV. Cross-sections quoted in this chapter therefore correspond to the predictions for production rates at this energy.

The signal process detailed in this analysis involves a Higgs boson which is produced via the fusion of two vector bosons ($W^{\pm}$ or Z^0), each one emitted from the proton's original quarks. This process is known as 'Vector Boson Fusion' (VBF) and provides a distinctive final state as the scattered quarks which emitted the vector bosons manifest themselves as jets in the forward region of the detector. The Higgs boson subsequently decays to two tau leptons. This process is depicted in the Feynman diagram in figure 6.1.

The dominant decays of taus are into leptons (plus two neutrinos) or one or three charged hadrons (plus one neutrino), as discussed in section 5.3. This therefore provides us with six possible final states, detailed (together with their

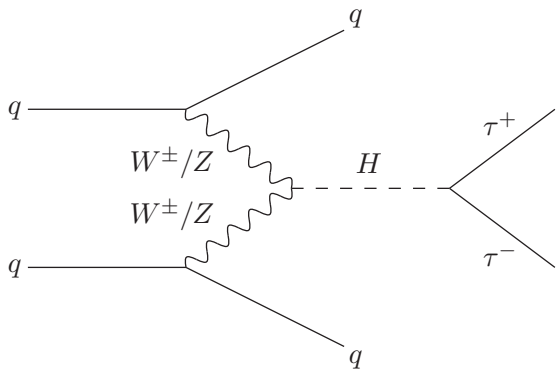

Figure 6.1: A Feynman representation of the VBF Higgs to Tau Tau process.

Final State		Branching Ratio (%)	
Di-Lepton	$\tau_e\tau_e$	3.2	12.4
	$\tau_e\tau_\mu$	6.2	
	$\tau_\mu\tau_\mu$	3.0	
Lepton-Hadron	$\tau_e\tau_h$	23.2	45.8
	$\tau_\mu\tau_h$	22.6	
Hadron-Hadron	$\tau_h\tau_h$	41.9	

Table 6.1: Tau pair final states and their branching ratios.

branching ratios) in table 6.1.

Although the hadron-hadron channel has a cross-section comparable with the lepton-hadron channel, it is very hard to trigger on because of large QCD backgrounds. For this reason it has not been included in this analysis at this time, although preliminary studies (see reference [9]) suggest that the fully hadronic channel may provide a viable analysis.

With the fully hadronic state excluded, the main experimental signature involves either a final state with one high p_T lepton (of at least 20 GeV) and one reconstructed hadronic tau jet, or two high p_T leptons, accompanied in both scenarios by missing energy. The VBF process provides distinctive jet activity, not only with two high p_T jets, generally in the forward region of the detector and a large separation in η, but also because other jet activity is suppressed due to a lack of colour exchange between the initial state quarks. Applying a veto on events with jet activity in the central region is a particularly effective way of

reducing QCD backgrounds.

Although the VBF $H \to \tau\tau$ process is perhaps the most promising discovery channel for a light Higgs (mass < 130 GeV), in this mass range the signal mass peak will be obscured by the tail from the $Z \to \tau^+\tau^- + N_{jets}$ mass peak. Whilst Z decays to e^+e^- and $\mu^+\mu^-$ (plus any number of accompanying jets) can be reduced by requiring that a significant amount of missing E_T is present (*i.e.* the leptons have the appearance of those which have come from tau decays), the contribution from the $Z \to \tau^+\tau^-$ decay mode is indistinguishable from the signal, except for the forward jet signature provided by the VBF process. Other processes expected to contribute significantly to the background include $W \to e^{\pm}\nu$, $W \to \mu^{\pm}\nu$, di-boson events (W^+W^-, W^+Z^0, W^-Z^0, Z^0Z^0) and $t\overline{t}$.

The baseline cuts for both analyses as specified by the ATLAS VBF Higgs to Tau Tau working group for an assumed Higgs mass of 120 GeV are summarised below [9]. A summary of these cuts and their effect on the signal (with statistical errors) in both decay modes are shown in table 6.2.

6.1.1 Monte Carlo Samples

Official ATLAS datasets generated with HERWIG [36] and with a Higgs mass of 120 GeV were used as signal samples. Two datasets, one containing 230,500 events where one tau is forced to decay leptonically and the other goes to hadrons, and one containing 86,750 events where both taus decay leptonically were used for the lepton-hadron and di-lepton analyses respectively. An ATLAS analysis framework, ATHENA [37], was used to analyse the simulated signal and background events.

6.1.2 Summary of Event Selection for Di-Lepton Channel

- Lepton Trigger: An isolated electron with $p_T > 20$ GeV, or an isolated muon with $p_T > 25$ GeV.

- Lepton p_T: $p_T(e) > 25$ GeV or $p_T(\mu) > 20$ GeV.

- Di-Lepton Requirement: The total number of electrons and muons in the event must be exactly equal to two.

- Missing p_T: There must be at least 40 GeV of missing transverse momentum.

- Collinear Approximation: The collinear approximation (see appendix A) is used to reconstruct the invariant mass of the two taus and is a good approximation when the parent particle is heavily boosted. It is assumed that the tau decay products are collinear to the parent's direction. To pass the cut, both tau daughters may carry up to 75% of their parent's momentum. In addition, the angle between the two tau decay products must not be in the region 154° to 206° since the approximation breaks down when the daughters are back to back. Once the momentum fractions of the decay products are known, the invariant mass of the tau pair can be calculated by $M_{\tau\tau} = m_{lh}/\sqrt{x_{\tau_{l1}} x_{\tau_{l2}}}$ where $x_{\tau_{l1}}$ and $x_{\tau_{l2}}$ are the momentum fractions carried by tau daughters 1 and 2 respectively.

- Two Jets: There must be two or more jets.

- Forward Jets: The two highest p_T tagged jets must have $p_T(1) > 40$ GeV and $p_T(2) > 20$ GeV and be in opposite hemispheres (*i.e.* that $\eta_1 \times \eta_2 < 0$).

- Centrality: The reconstructed taus must lie between the tagged jets in pseudo-rapidity.

- Angular Requirement: The decay products of the Higgs are generally back-to-back, so the separation in ϕ between the two reconstructed leptons is required to be < 2.6, and the ϕ separation of the two forward jets must be < 2.2.

- Jet Kinematics: The separation of the two tagged jets must be $\Delta\eta_{jj} > 4.4$ and the invariant mass of the two highest p_T tagged jets must be greater than 700 GeV.

- Central Jet Veto: The event is vetoed if any of the remaining jets in the event have $p_T > 20$ GeV and $|\eta| < 3.2$.

- Mass Window: The reconstructed Higgs mass must lie with ± 15 GeV of the Monte Carlo Higgs Mass (*i.e.* 105 GeV $< M_H <$ 135 GeV).

6.1.3 Summary of Event Selection for Lepton-Hadron Channel

- Lepton Trigger: An isolated electron with $p_T > 20$ GeV, or an isolated muon with $p_T > 25$ GeV.

- Lepton p_T: $p_T(e) > 25$ GeV or $p_T(\mu) > 20$ GeV.

- Di-Lepton Veto: The total number of electrons and muons in the event must be less than two.

- Tight Tau: Require one hadronic tau cluster in the calorimeter with $p_T >$ 40 GeV and $|\eta| < 2.5$.

- Missing p_T: There must be at least 30 GeV of missing transverse momentum.

- Collinear Approximation: The hadronic tau daughter can carry any fraction of its parents momentum and the leptonic daughter can carry up to 75% of its parents momentum. As in the di-lepton channel analysis, the angle between the two tau decay products must not be in the region 154° to 206°.

- Transverse Mass Cut: A cut on the transverse mass (where $\mathrm{M_T}(l\nu) = \sqrt{2p_T(l)\not{E}_T(1 - cos\Delta\phi_{l-\not{E}_T})}$) is applied in order to suppress the $t\bar{t}$ back-

ground, where the lepton and the missing transverse momentum originate from the decay of a W boson. $M_T(l\nu)$ is required to be < 30 GeV.

- Two Jets: There must be two or more jets.
- Forward Jets: The two highest p_T tagged jets must have $p_T(1) > 40$ GeV and $p_T(2) > 20$ GeV and be in opposite hemispheres (*i.e.* that $\eta_1 \times \eta_2 < 0$).
- Centrality: The reconstructed taus must lie between the tagged jets in pseudo-rapidity.
- Jet Kinematics: The separation of the two tagged jets must be $\Delta\eta_{jj} > 4.4$ and the invariant mass of the two highest p_T tagged jets must be greater than 700 GeV.
- Central Jet Veto: The event is vetoed if any of the remaining jets in the event have $p_T > 20$ GeV and $|\eta| < 3.2$.
- Mass Window: The reconstructed Higgs mass must lie with $\pm$ 15 GeV of the Monte Carlo Higgs Mass (*i.e.* 105 GeV $< M_H <$ 135 GeV).

6.2 Backgrounds

The main processes contributing to background come from $Z \to ee/\mu\mu/\tau\tau + N$ partons (QCD and EW), $W \to e\nu/\mu\nu + N$ partons, WW, WZ, ZZ and $t\bar{t} \to WbWb$. Of these, the main contributions come from the $t\bar{t}$ and $Z \to \tau\tau$ processes.

6.2.1 $Z \to \tau\tau$

The di-tau final state from the $Z \to \tau\tau$ process is kinematically the same as that from $H \to \tau\tau$, so here reliance on cuts to select the forward VBF jets in the signal are most effective at reducing $Z \to \tau\tau$ events. Z's can be produced in association

Cut	Di-Lepton Channel (fb)	Lepton-Hadron Channel (fb)
Production	22	145
Lepton Trigger	13.04 ±0.04	57.2 ±0.2
Lepton p_T	11.64 ±0.02	49.51 ±0.06
$Di-Lepton\ Requirement/Veto$	5.48 ±0.03	43.49 ±0.06
Tight Tau	-	8.45 ±0.07
Missing p_T *Cut*	3.18 ±0.02	5.16 ±0.04
Collinear Approximation	2.15 ±0.01	3.14 ±0.03
Transverse Mass Cut	-	2.39 ±0.02
Two Jets	1.776 ±0.009	1.97 ±0.02
Forward Jets	1.479 ±0.008	1.60 ±0.01
Centrality	1.343 ±0.006	1.46 ±0.01
Angular Requirement	1.075 ±0.007	-
$\Delta\eta_{jj}$	0.677 ±0.008	0.89 ±0.01
M_{jj}	0.578 ±0.005	0.781 ±0.008
Central Jet Veto	0.509 ±0.004	0.683 ±0.007
Mass Window	0.421 ±0.004	0.562 ±0.008

Table 6.2: Summary of the effects on the cross-section as cuts are made on the signal samples.

with any number of jets, but due to the requirements made on jets in the event, production in association with 2-jets poses the biggest threat. In addition the EW production also includes production by VBF, and in this scenario the contribution is irreducible. Feynman diagrams for $Z \to \tau\tau\ +\ 2-jets$ processes are given in figures 6.2 and 6.3.

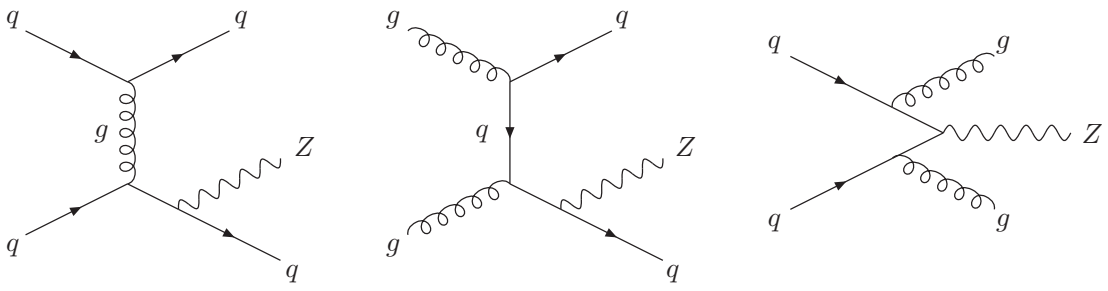

Figure 6.2: Feynman diagrams for the QCD $Z+$ 2 jets processes.

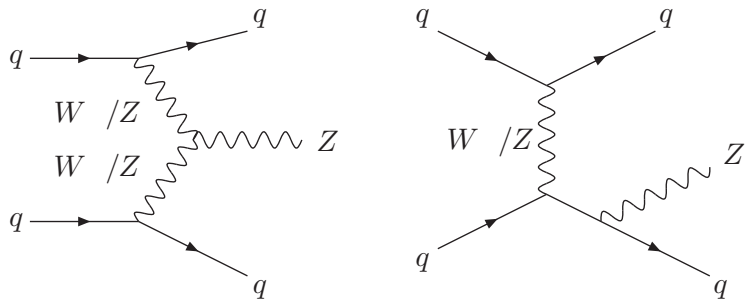

Figure 6.3: Feynman diagrams for the EW Z+ 2 jets processes.

6.2.2 $t\bar{t}$

Across all mass ranges, a major background contribution to a VBF H $\rightarrow \tau\tau$ analysis is expected to come from $t\bar{t}$ [11], which not only has a similar signature to that of the signal, but also has a very large production cross-section (833, 000 fb). The predominant top quark decay mode (accounting for almost 100% of events [33]) is each top quark decaying to a W-boson and a b-quark. The b-quark produces a jet and the W decays to either leptons (an electron or muon, plus the accompaniying neutrino), jets, or to a tau which itself subsequently decays to leptons or hadrons. The b-jets can mimic the forward jets seen in the signal and the W decay products can be misidentified as coming from taus. A diagrammatic representation of this process is shown in figure 6.4.

6.3 Classification of $t\bar{t}$ Background

The $t\bar{t}$ sample used was generated using the MC@NLO [38] (Monte Carlo at next-to-leading order) matrix element with HERWIG [36] and full detector simulation. Events where both W-bosons decay hadronically are excluded. Due to the generation method of MC@NLO, each event in the sample has a weighting of ± 1 which must be taken into account when counting events for cut flows or filling histograms. Approximately 650,000 events are available at this time, of which around 450,000 remain after taking into account the event weights and

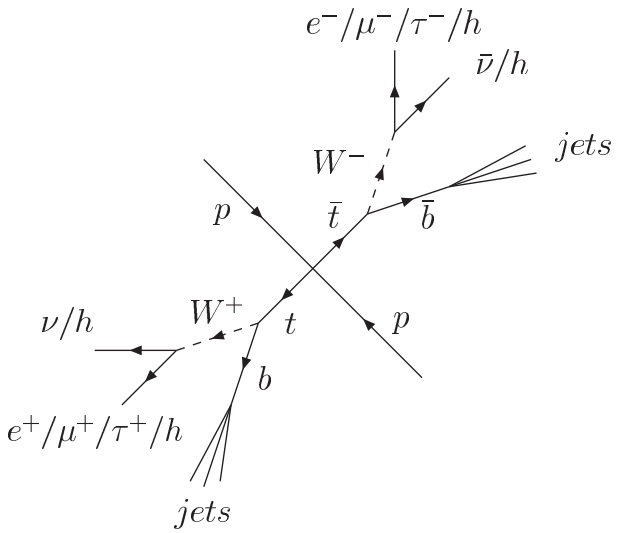

Figure 6.4: A schematic of top quark production and decay.

before applying any cuts. This corresponds to an integrated luminosity of approximately 1 fb^{-1}. By running the analysis code over the background sample and applying the same cuts as for the signal, a preliminary estimate of the rate of this background can be made. Table 6.3 shows the effects of each cut when applied to the $t\bar{t}$ background sample.

6.3.1 Contributions to Different $t\bar{t}$ Decay Modes

The $t\bar{t}$ process provides a particularly complex background process to the VBF H $\rightarrow \tau\tau$ signal because it contains both reducible and irreducible elements, particularly in the lepton-hadron channel where W's decaying to jets can mimic a hadronically decaying τ. To understand the composition of the $t\bar{t}$ background, the true decays of the W-boson from the top quark decay were examined, after the 'Lepton Trigger', 'Lepton p_T', 'Di-Lepton Requirement/Veto' and 'Tight Tau' (lepton-hadron channel only) cuts had been applied. The results are shown in table 6.4.

From this it is seen that the largest contribution to the $t\bar{t}$ background in the di-lepton channel comes from cases where the final state involves two leptons at truth

Cut	Di-Lepton Channel (fb)	Lepton-Hadron Channel (fb)
Production	461160	461160
Lepton Trigger	214960 ± 340	214960 ± 340
Lepton p_T	183670 ± 160	183670 ± 160
$Di-Lepton\ Requirement/Veto$	22880 ± 140	160600 ± 140
Tight Tau	-	6430 ± 80
Missing p_T *Cut*	17690 ± 60	5200 ± 30
Collinear Approximation	1950 ± 40	690 ± 20
Transverse Mass Cut	-	220 ± 10
Two Jets	1840 ± 10	204 ± 4
Forward Jets	840 ± 20	98 ± 7
Centrality	320 ± 10	34 ± 5
Angular Requirement	235 ± 8	-
$\Delta\eta_{jj}$	48 ± 6	2 ± 1
M_{jj}	41 ± 2	1.0 ± 0.7
Central Jet Veto	4 ± 2	0 ± 1
Mass Window	0 ± 1	0 ± 1

Table 6.3: Summary of the cuts made on the $t\overline{t}$ background sample, their effects on the cross-section, and the efficiency of each cut.

level ($WW \to e+e$, $WW \to e+\mu$, $WW \to \mu+\mu$, $WW \to e/\mu+\tau_l$ and $WW \to \tau_l+\tau_l$ – approximately 54%). Yet there is also a large contribution (∼38%) from events with final states involving one truth level lepton, plus hadronic jets from W-decay ($WW \to e/\mu/\tau_l + jet$), and to a lesser extent (∼7%), events with a truth level lepton accompanied by a hadronically decaying tau ($WW \to e/\mu+\tau_h$ and $WW \to \tau_l+\tau_h$).

For the lepton-hadron channel, whilst the final state including a lepton and hadronically decaying tau at truth level ($WW \to e/\mu+\tau_h$ and $WW \to \tau_l+\tau_h$ – approximately 37%) provides a significant proportion of the total $t\overline{t}$ background, there is an even larger proportion of events (∼43%) where the final state involves a true lepton, and a hadronic jet which can fake a tau ($WW \to e/\mu/\tau_l + jet$). In around 10% of cases the true final state involves two leptons ($WW \to e+e$, $WW \to e+\mu$, $WW \to \mu+\mu$, $WW \to e/\mu+\tau_l$ and $WW \to \tau_l\tau_l$), but one of these is not reconstructed and something else fakes a hadronically decaying tau.

Decay Mode (Truth)	Di-Lepton Channel	Lepton-Hadron Channel
$WW \rightarrow e + \tau_l$	2.5%	0.8%
$WW \rightarrow e + \tau_h$	2.4%	14.3%
$WW \rightarrow e + jet$	14.2%	16.8%
$WW \rightarrow e + e$	7.5%	3.2%
$WW \rightarrow e + \mu$	22.7%	5.1%
$WW \rightarrow \mu + \tau_l$	4.0%	0.4%
$WW \rightarrow \mu + \tau_h$	4.0%	20.6%
$WW \rightarrow \mu + jet$	21.4%	24.1%
$WW \rightarrow \mu + \mu$	17.2%	0.5%
$WW \rightarrow \tau_l + \tau_l$	0.2%	0.0%
$WW \rightarrow \tau_l + \tau_h$	0.5%	2.0%
$WW \rightarrow \tau_h + \tau_h$	0.1%	1.2%
$WW \rightarrow \tau_l + jet$	2.0%	2.2%
$WW \rightarrow \tau_h + jet$	1.2%	8.9%

Table 6.4: Decay modes for $t\bar{t} \rightarrow Wb\ Wb$ ($WW \rightarrow Final\ State$) in each of the analysis channels. The results are normalised to the number of events which pass all cuts up to and including the di-lepton requirement (di-lepton channel), or hadronic tau requirements and di-lepton veto (lepton-hadron mode).

A not insignificant contribution (∼9%) from $t\bar{t}$ events where $WW \rightarrow \tau_h + jet$ is also observed.

6.3.2 Matching Reconstructed Taus to Truth Level W-Boson Decay Products

From table 6.4, it can be seen that $WW \rightarrow lepton + jet$ decays account for approximately 43% of the $t\bar{t}$ contribution in the lepton-hadron channel. As expected, cases where the final state involves a true tau also provide a significant contribution (37%) in this decay mode.

To determine how often the reconstructed tau has come from the W-boson decay products, one can look at the direction of the true W-decay products, and compare this with the direction of the reconstructed tau. When these objects do not have the same direction (within errors), it can be deduced that the reconstructed tau must have come from something other than the W-boson decay.

The reconstructed leptonic taus are matched with W's that have either an electron or a muon as a daughter or granddaughter (*i.e.* the W-boson decays directly to either an electron or a muon, or to a tau which subsequently decays leptonically), and hadronic taus are matched with W's that have decayed to either hadronic taus or jets. The variable ΔR (where ΔR is defined to be $\sqrt{(\Delta\eta^2+\Delta\phi^2)}$) between the reconstructed tau and true W-decay products from $t\bar{t}$ is calculated and the objects are said to match if ΔR <0.1. If more than one candidate was available, the minimum ΔR combination was chosen. For the di-lepton channel, the requirement was made that there must be two fully reconstructed leptons in the event, and for the lepton-hadron channel, one fully reconstructed lepton and one tau jet were demanded. The ΔR between the reconstructed tau and true W-decay product is shown in figure 6.5. In the lepton-hadron channel, the decay products from the W-bosons are reconstructed as a leptonic tau 70% of the time (*i.e.* $\Delta R_{\tau_l,W}$ is < 0.1 in 70% of cases) and as a hadronic tau ($\Delta R_{\tau_h,W}$ is $<$

0.1) in 64% of cases. Both match just 60% of the time. In the di-lepton channel, one of the W-boson daughters matches a reconstructed tau just 54% of the time, with both matching in only 48% of cases.

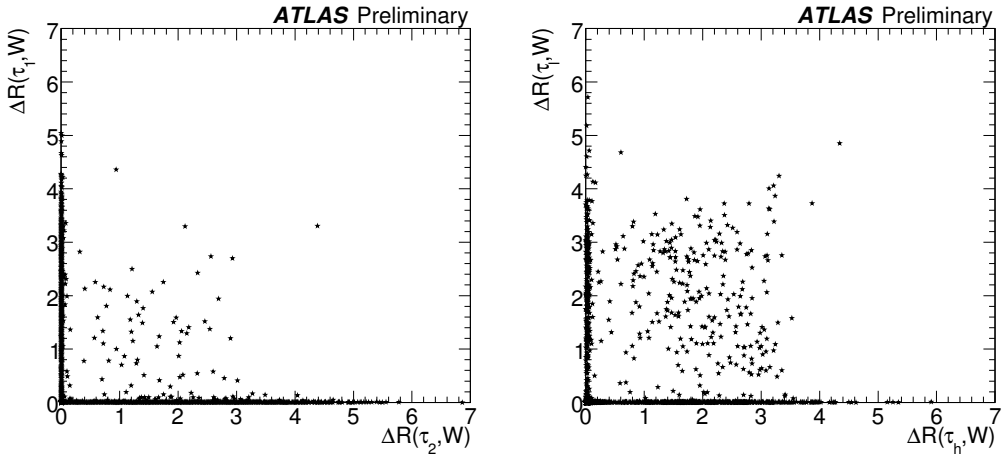

(a) Di-Lepton Channel (b) Lepton-Hadron Channel

Figure 6.5: Matching truth level W-decay products to reconstructed tau daughters. In the di-lepton channel, τ_1 is the higher p_T tau, and τ_2 is the lower p_T tau. For the lepton-hadron channel, τ_l is the leptonically decaying tau and τ_l is the hadronically decaying tau.

6.3.3 Matching Reconstructed Taus to Truth Level b-Decays

Table 6.4 also reveals a surprisingly large contribution (38%) from the $WW \rightarrow lepton + jet$ decay modes in the di-lepton channel. A possible source for these leptons may be from b-quark decays (where the b-quark comes from the top quark decay into W and b). In this section an estimate of the background contribution from the misidentification of leptons from b-jets is provided.

Table 6.5 shows the contributions from the $WW \rightarrow e+jet$ and $WW \rightarrow \mu+jet$ truth states to the ee, $e\mu$, $\mu\mu$ reconstructed final states. The matching process described in section 6.3.2 is repeated, but this time matching reconstructed tau daughters to the true b-jets from $t\bar{t}$ decays. Events where $WW \rightarrow e + jet$ and

	$WW \to e + jet$ truth state			$WW \to \mu + jet$ truth state		
Reconstructed State	Total	1 Match	2 Matches	Total	1 Match	2 Matches
$H \to \tau\tau \to ee$	675	61%	0%	0	-	-
$H \to \tau\tau \to e\mu$	6226	74%	0.2%	977	62%	0.5%
$H \to \tau\tau \to \mu\mu$	145	89%	52%	9645	74%	0.3%

Table 6.5: Proportion of $WW \to lepton + jet$ events where one or more of the reconstructed taus comes from the b-daughters, for each of the di-lepton channel reconstructed final states. Results are normalised to the number of events which pass the di-lepton requirement.

$WW \to \mu + jet$ were selected, and then the di-lepton requirement cut was applied. The columns '1 Match' and '2 Matches' give the fraction of reconstructed electrons/muons with a direction that matches the true b-quark direction.

From table 6.5, it can be seen that cases where the b-jet fakes a lepton from a tau represent a large fraction of the $WW \to lepton + jet$ background and that the muon contribution dominates this background. To estimate the relative reconstruction efficiency for muons and electrons, the ratio of the proportion of $WW \to \mu + jet$ type events to the proportion of $WW \to e + jet$ type events (from table 6.4) can be calculated. This ratio is 1.5 (21.4/14.2) for the di-lepton channel, and 1.4 (24.1/16.8) for the lepton-hadron channel.

Looking again at table 6.5, and making the assumption that one of the leptons in the reconstructed state comes from the W-decay (only the $WW \to lepton+jet$ contribution is considered here), the ratio of the number of events which are reconstructed as $H \to \tau\tau \to e\mu$ (6226) to the number of events reconstructed as $H \to \tau\tau \to ee$ (675) from the $WW \to e + jet$ truth state can be calculated. It is observed that this ratio is 9.2 – approximately 6 times greater than the relative reconstruction efficiency ratio for electrons and muons calculated above. A similar result (ratio of 9.8) is obtained by comparing the number of events which are reconstructed as $H \to \tau\tau \to e\mu$ (9645) to the number of events reconstructed as $H \to \tau\tau \to \mu\mu$ (977) from the $WW \to \mu + jet$ truth state. A much larger number of $H \to \tau\tau \to \mu\mu$ reconstructed events from $WW \to e + jet$ type events

(145 events) than $H \to \tau\tau \to ee$ reconstructed events from the $WW \to \mu + jet$ contribution (0 events) is also seen.

So whilst this electron/muon asymmetry can be partly explained by the difference in the reconstruction efficiencies for these objects, there could be specific electron selection requirements which suppress the reconstruction of fake electrons from jets (and in particular from b-jets). One of these requirements could be isolation. Although a muon isolation requirement was included in the analysis on which this study is based and [9], supplementary studies on muon isolation requirements may be helpful in reducing this contribution further.

Bearing this in mind, the entire $t\bar{t}$ sample is considered once more, and for both the di-lepton and lepton-hadron channels. The ΔR between the true b-daughters and the reconstructed tau daughters are plotted in figure 6.6. Once again, the closest match combination was chosen. In the di-lepton case, the higher p_T tau is labelled as tau 1, and the less energetic as tau 2. From figure 6.6, it is observed that a significant proportion of reconstructed leptonic tau daughters actually come from b-quark decays. In the di-lepton channel, 8% of the higher p_T tau daughters and 30% of the lower p_T tau daughters come from the b-jet. For the lepton-hadron channel, 16% of the leptonic tau daughters and 3% of the hadronic tau daughters have a match with the b-jet.

6.3.4 Matching Reconstructed Forward Jets to Truth Level b-Decays

In figure 6.7, the ΔR between a reconstructed forward jet and the true b-jet from the top quark decay is plotted (taking the minimum ΔR combination). Using the same definition of matching as before (*i.e.* that the absolute value of ΔR must be < 0.1), it is found that either reconstructed forward jet matches a b-jet in only 66% of cases, and both match just 13% of the time.

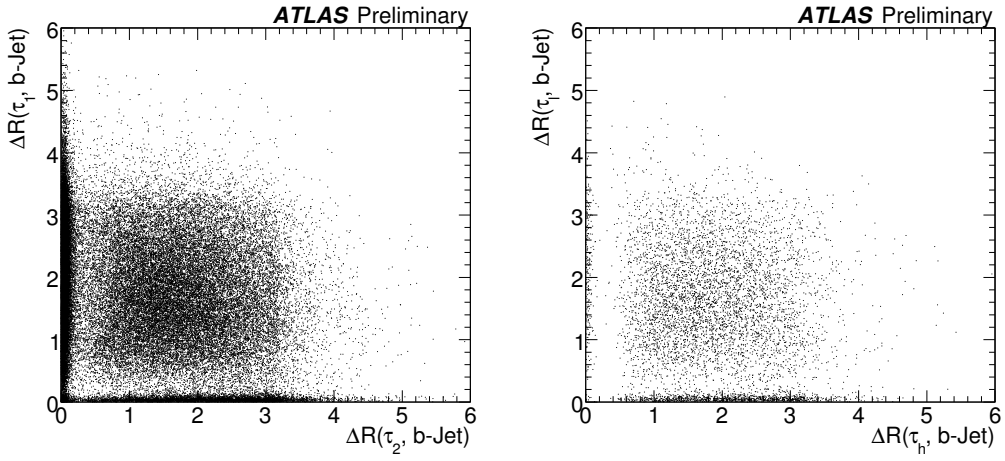

(a) Di-Lepton Channel (b) Lepton-Hadron Channel

Figure 6.6: Matching truth level b-daughters to reconstructed tau daughters.

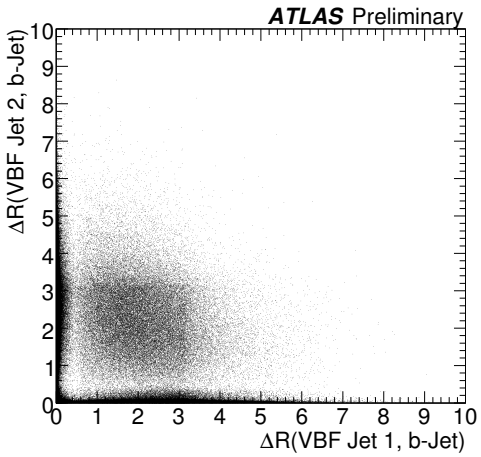

Figure 6.7: Matching reconstructed forward jets to truth level b-jets from top quark decays. The higher p_T jet is denoted as 'Jet 1', and the lower p_T jet as 'Jet 2'.

6.4 Suppression of $t\bar{t}$ Background

6.4.1 Introducing a b-Jet Veto

It was shown in section 6.3.4 that one of the b-jets from the top quark decay can mimic the forward jets from the VBF process. The results of section 6.3.3 also

indicate that the b-decay products can masquerade as a tau (particularly in the di-lepton channel, where the b-daughter is a muon). Since there should be no b-jets in the VBF H$\rightarrow \tau\tau$ process, incorporating a b-jet veto into the cut flow should help to reduce the contribution from these classes of $t\bar{t}$ background.

b-jets are identified in ATLAS by searching for tracks associated to a secondary vertex. Tracks likely to have come from decays of long-lived particles (*e.g.* K_S decays) are rejected, and the impact parameter of tracks with respect to the primary vertex is also considered. Several variables are taken into account and combined to form a b-tagging weight. More details can be found in reference [9]. The b-tagging weight of the highest weighted jet in each event (once the requirements on forward jets have been made) is plotted in figures 6.8(a) and 6.8(c). From this, very different shapes in the distributions for signal and $t\bar{t}$ background are observed.

The figure of merit $S/\sqrt{S+B}$ at different b-tag weights is plotted in figures 6.8(b) and 6.8(d) for several different methods of calculating the weight. The first method was to use the b-tagging weight of the highest weighted jet in the event. The second was to take the summed weight of the two highest weighted jets in the event, whilst the third considered the summed weight of the two forward jets. The ATLAS standard cut on b-tagging weight is set to 6.75, a value which was chosen to optimise light jet rejection. However, in order to reject $t\bar{t}$ events, this value must be optimised to anti-select b-jets.

From figures 6.8(b) and 6.8(d), it was decided to apply a cut on the maximum b-tag weight for any jet in the event at 1.0. This optimises the value $S/\sqrt{S+B}$ in the lepton-hadron channel, is close to the optimal value of $S/\sqrt{S+B}$ in the di-lepton channel, yet is sufficiently far away enough from the edge to be considered safe. This requirement is now introduced into the cut flow (after the restrictions on the forward jets have been made). Figure 6.9 demonstrates the performance of the b-jet veto as a function of the p_T of the leading forward jet. Due to a lack of statistics, only cuts which apply to tagging jets were imposed for this study.

It is expected that this value may need to be re-optimised once a bigger sample is available.

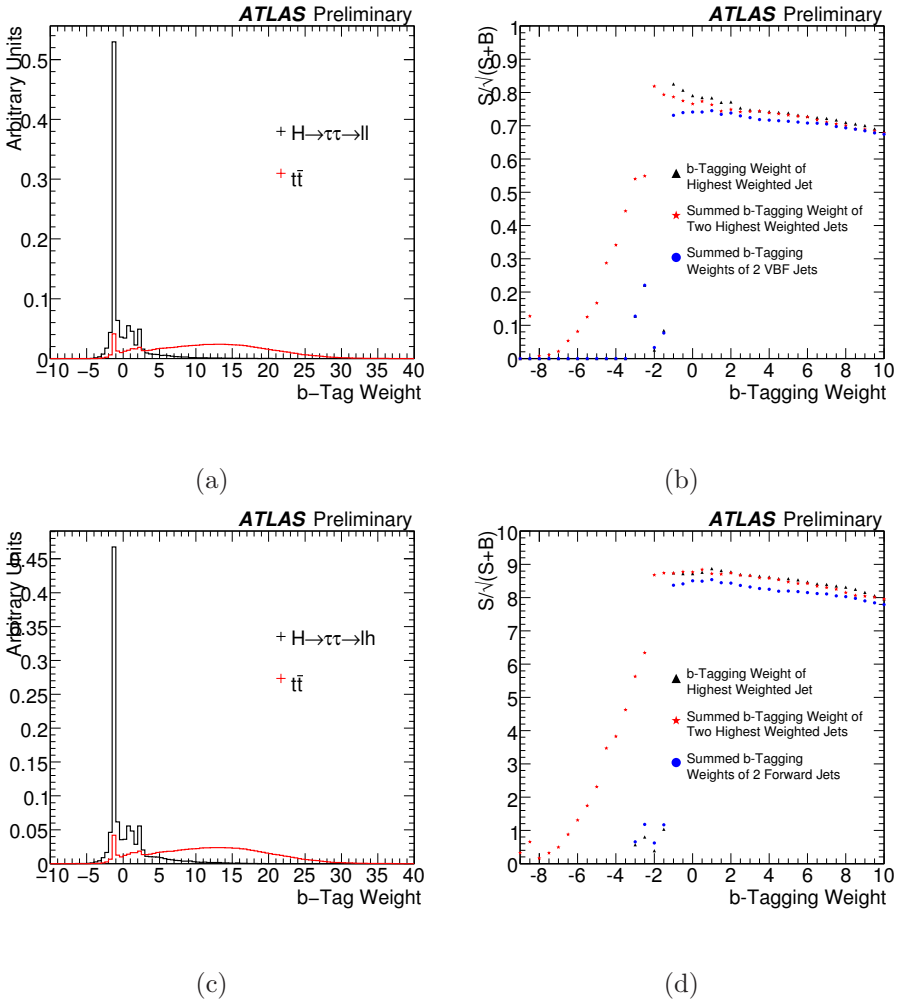

Figure 6.8: Optimising the b-jet veto for the di-lepton ((a) and (b)) and lepton-hadron ((c) and (d)) channels. (a,c) Very different distributions of b-tagging variables (e.g. the b-tagging weight of the highest weighted jet in an event) are observed for signal and $t\bar{t}$ background. (b,d) Using the figure of merit as $S/\sqrt{S+B}$ and assuming an integrated luminosity of 30 fb^{-1}, it was decided to veto any events where the maximum b-jet weight in an event is greater than 1.0.

It should be noted that the tracker acceptance is $|\eta| < 2.5$. Even with soft leptons, b-tagging outside this region (where there is by definition no inner detector track) is likely to be extremely difficult, if not impossible. At the time of

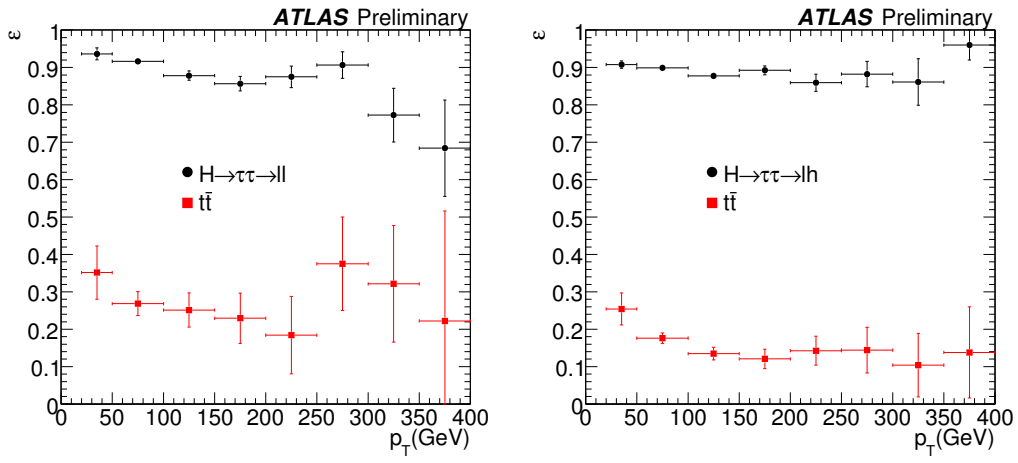

(a) Di-Lepton Channel (b) Lepton-Hadron Channel

Figure 6.9: Performance of the b-jet veto as a function of the leading forward jet p_T.

writing, ATLAS does not provide any functionality for b-tagging in the $|\eta| > 2.5$ region. This has been taken into account in the results presented here however, since samples with full detector simulation were used.

6.4.2 Charge Correlation Between Tau Decay Products

One of the largest contributions to the $t\bar{t}$ background in both channels comes from events where the final state involves a pair of W bosons which have decayed to a lepton plus jets (see table 6.4). In the lepton-hadron decay mode, this jet then fakes the hadronic tau in the signal. The true tau events (where $t \to Wb, W \to \tau\nu$) should have opposite signs between the charges of the decay products (e.g. an $e^-$and a τ^+), whereas events in which jets fake a hadronically decaying tau should have a proportion of events with the same sign charge on the final state particles (although one should bear in mind that if this jet comes from W decay it will still be correlated to the decay products of the other W-boson, and so a preference for opposite-sign events should still be observed). Section 6.3.3 showed that at least one of the reconstructed taus actually comes from the b-decay in a

significant proportion of events, in which case less correlation between the charge of the reconstructed tau daughters than in events where both come from W decays would be expected.

The quantity $Q_{\tau\ daughter\ 1} \times Q_{\tau\ daughter\ 2}$ is calculated in figure 6.10. Figures 6.10(a) and 6.10(a) show this distribution for the signal and inclusive $t\bar{t}$ background, and figure 6.10(c) shows only the subset of $t\bar{t}$ background to the lepton-hadron channel where $WW \rightarrow e/\mu + jets$.

For events where the final state involves a true tau, the tau daughters should have opposite-sign charge and so $Q_{\tau\ daughter\ 1} \times Q_{\tau\ daughter\ 2}$ should be -1. Fake tau backgrounds should contain a proportion of events where the final state particles have the same sign charge ($Q_{\tau\ daughter\ 1} \times Q_{\tau\ daughter\ 2} = +1$). Efficiency is better in the di-lepton channel, as is expected due to better charge determination for leptons than jets. Around 25% of the $lepton + jet$ type events are reconstructed as same-sign events. Whilst a 50:50 split between same-sign and opposite-sign modes might naively be expected, misidentifying the charge of, or missing one of the component tracks of a hadronic jet can mean that the overall charge of the jet is mis-attributed. This effect will be more pronounced in lower multiplicity jets, and since it is generally low multiplicity jets which are reconstructed as hadronic taus (which typically have 1 or 3 tracks), a lower proportion of same-sign events than may be initially expected is observed.

Applying a charge correlation cut in the lepton-hadron channel cuts about 5% of signal events, and 16% of $t\bar{t}$ events, whilst in the di-lepton channel the cut has a negligible effect on the signal (cutting just 0.3% of events) and 3% of $t\bar{t}$ events.

A requirement on charge correlation is introduced into the cut flow immediately after di-lepton/lepton-hadron type events have been selected. As expected, requiring that the tau daughters have opposite sign charge has the greatest effect on decay modes that include a jet which fakes a hadronically decaying tau.

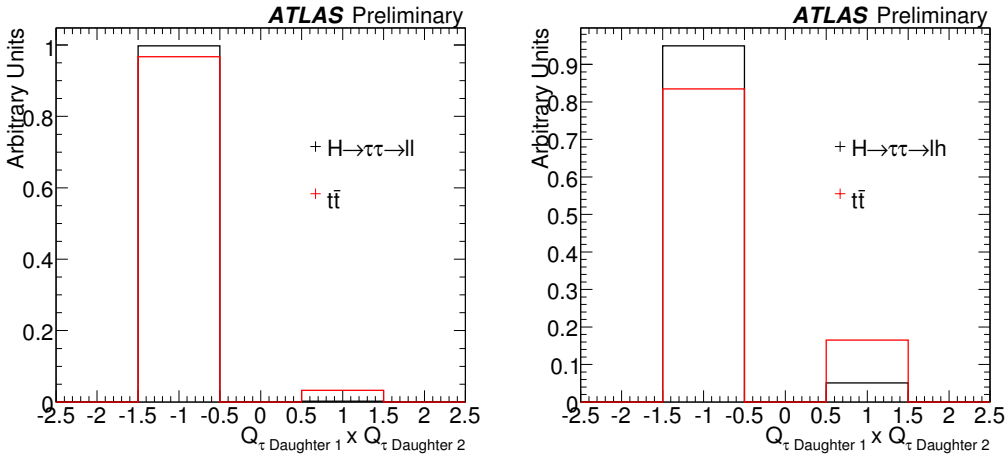

(a) Di-Lepton Channel

(b) Lepton-Hadron Channel

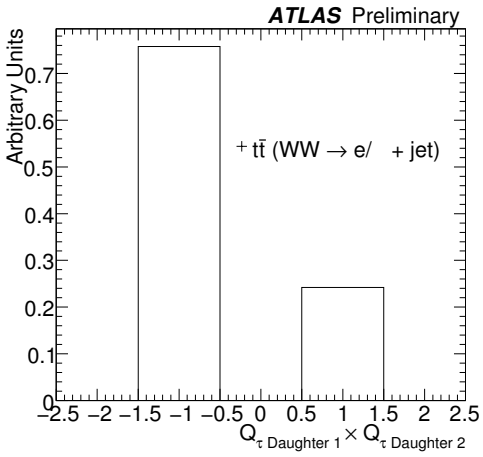

(c) Lepton-Hadron Channel ($t\bar{t} \rightarrow\ WW\ \rightarrow\ e/\mu + jet$ subset)

Figure 6.10: The quantity $Q_{\tau\ daughter\ 1} \times Q_{\tau\ daughter\ 2}$ is calculated for signal and inclusive $t\bar{t}$ background for (a) di-lepton channel, (b) lepton-hadron channel, and (c) the subset of the $t\bar{t}$ background to the lepton-hadron channel where $WW \rightarrow e/\mu + jet$.

6.4.3 Incorporating 'Charge Correlation' and 'b-jet Veto' Cuts into the Analysis

Demanding that the tau decay products have opposite-sign charge, and applying a veto on any jets with a b-tagging weight greater than 1.0, improves the suppression

Cut	$H \to \tau\tau \to ll\ (fb)$	$t\bar{t}\ \ (fb)$
Production	22	461160
Lepton Trigger	13.04 ± 0.04	214960 ±340
Lepton p_T	11.64 ± 0.02	183670 ±160
$Di-Lepton\ Requirement$	5.48 ± 0.03	22880 ±140
Charge Correlation	5.461 ± 0.002	22090 ± 30
Missing p_T *Cut*	3.17 ± 0.02	17160 ± 60
Collinear Approximation	2.15 ± 0.01	1860 ± 40
Two Jets	1.772 ± 0.009	1757 ± 10
Forward Jets	1.476 ± 0.008	800 ± 20
Centrality	1.341 ± 0.006	300 ± 10
$b-Jet\ Veto$	1.156 ± 0.006	94 ± 8
Angular Requirement	0.929 ± 0.007	75 ± 4
$\Delta\eta_{jj}$	0.605 ± 0.007	26 ± 4
M_{jj}	0.517 ± 0.004	22 ± 2
Central Jet Veto	0.455 ± 0.004	1 ± 1
Mass Window	0.376 ± 0.004	0 ± 1

Table 6.6: Summary of di-lepton channel cut flow for signal and $t\bar{t}$ background once cuts on the charge correlation between the tau daughters and a b-jet veto have been imposed.

of $t\bar{t}$ events, whilst still maintaining the number of signal events. Cut flows for signal and $t\bar{t}$ are shown for both the di-lepton and lepton-hadron channels in tables 6.6 and 6.7 respectively.

6.5 Estimating Background Contributions

Several million $t\bar{t}$ events would be needed to directly estimate the rejection efficiency of the cut flow, but generating this many fully simulated events would be unrealistic due to the large amount of computing power needed and time required. This is also the case for several other background processes. Bearing this in mind, it becomes apparent that it is beneficial to devise other methods to obtain an estimate for the suppression factor.

Cut	$H \to \tau\tau \to lh\ (fb)$	$t\bar{t}\ \ (fb)$
Production	145	461160
Lepton Trigger	57.2 ± 0.2	241960 ± 340
Lepton p_T	49.51 ± 0.06	183670 ± 160
$Di-Lepton\ Veto$	43.49 ± 0.06	160600 ± 140
Tight Tau	8.45 ± 0.07	6430 ± 80
Charge Correlation	8.02 ± 0.02	5390 ± 20
Missing p_T *Cut*	4.88 ± 0.03	4390 ± 30
Collinear Approximation	3.07 ± 0.03	590 ± 20
Transverse Mass Cut	2.33 ± 0.02	190 ± 10
Two Jets	1.93 ± 0.01	175 ± 3
Forward Jets	1.57 ± 0.01	85 ± 7
$b-Jet\ Veto$	1.34 ± 0.01	20 ± 4
Centrality	1.237 ± 0.008	10 ± 2
$\Delta\eta_{jj}$	0.77 ± 0.01	0 ± 1
M_{jj}	0.681 ± 0.007	0 ± 1
Central Jet Veto	0.601 ± 0.007	0 ± 1
Mass Window	0.494 ± 0.007	0 ± 1

Table 6.7: Summary of lepton-hadron channel cut flow for signal and $t\bar{t}$ background once cuts on the charge correlation between the tau daughters and a b-jet veto have been imposed.

Tau Cuts	Jet Cuts	Correlation To Both
Trigger	Two Jets	Angular Requirement†
Lepton p_T	Forward Jets	Centrality
Di-Lepton Veto*/Req†	b-Jet Veto†	Central Jet Veto
Tight Tau*	Jet Separation	Mass Window
Missing p_T	M_{jj} Cut	
Collinear Approx		
m_T Cut		

Table 6.8: Categorisation of cuts for 'Cut Factorisation Method'. A '*' signifies cuts which only apply to the lepton-hadron channel. A '†' signifies those which only apply to the di-lepton event selection. The b-jet veto is not included in the lepton-hadron channel event selection criteria due to a lack of signal events in this mode and to conform with the ATLAS group convention.

6.5.1 Cut Factorisation Method

The cuts applied to select the signal events can generally be categorised as either 'tau-type' cuts (*i.e.* cuts to select tau-like objects), or 'jet-type' cuts, (*i.e.* cuts optimised to select forward jets). For both the signal and $t\bar{t}$ processes, correlations between tau-type cuts and jet-type cuts are neglected and the different categories of cuts are considered independently[1]. Correlation effects are checked by comparing direct calculations of efficiency with efficiencies calculated using the Cut Factorisation Method whenever possible. The cuts are grouped according to table 6.8.

The efficiency is calculated when only the tau cuts are applied, and then when only the jet cuts are applied. Finally, the efficiencies of those cuts which have a correlation to both the taus and the forward jet are calculated individually by making a 'basic selection' (requiring just lepton-hadron or di-lepton events with p_T requirements and two forward jets). The efficiencies obtained in each category

[1]There is indeed some correlation between 'tau type' and 'jet type' cuts. Its influence on the results can be estimated by making a comparison with the direct efficiency calculations (the corresponding cross-sections are given in tables 6.9 and 6.10 whenever these figures are available).

can then be multiplied together to obtain an estimate for the total efficiency had all cuts been applied together. This is shown in equation 6.1.

$$\begin{aligned}\varepsilon_{Total} &= \varepsilon_{Tau\ Cuts} \times \varepsilon_{Jet\ Cuts} \times \varepsilon_{Centrality} \times \\ &\quad \varepsilon_{Central\ Jet\ Veto} \times \varepsilon_{Angular\ Requirements} \times \varepsilon_{Mass\ Window} \\ &= \frac{N_{Tau\ Cuts}}{N_{Total}} \times \frac{N_{Jet\ Cuts}}{N_{Total}} \times \frac{N_{Centrality}}{N_{Basic\ Selection}} \times \\ &\quad \frac{N_{Central\ Jet\ Veto}}{N_{Basic\ Selection}} \times \frac{N_{Angular\ Requirement}}{N_{Basic\ Selection}} \times \frac{N_{Mass\ Window}}{N_{Basic\ Selection}}\end{aligned} \tag{6.1}$$

Estimates of final cross-sections with statistical errors once all cuts have been made can be seen in tables 6.9 (di-lepton channel) and 6.10 (lepton-hadron channel). Direct estimates from the cut flows are also given when possible. Comparing these direct estimates with values from the Cut Factorisation Method shows that the values differ by up to a factor of 5. However, statistical errors are large for most of the direct calculations due to the small number of events remaining after all cuts have been applied. Uncertainties arising from residual correlations between the different types of cuts are not calculated.

6.6 Optimising Topological Cuts in the Lepton-Hadron Channel

Several of the cuts are based on the event topology, namely the separation in η and mass of the two forward jets and the centrality requirement (the τ's must lie in between the forward jets). By replacing the centrality cut with a continuous variable, these three cuts can then be combined into one which can be analysed using log-likelihood methods. The centrality requirement is thus replaced with the minimum angle between each of the reconstructed taus and the forward jets (without counting the same forward jet more than once per event). As shown in figure 6.11, the distributions of this value for signal and $t\bar{t}$ are very different,

	σ_{Start} (fb)	σ_{End}^{CFM} (fb)	σ_{End}^{Direct} (fb)
$H \to \tau\tau$	22	1.6×10^{-1} $\pm5\times10^{-3}$	3.8×10^{-1} $\pm1\times10^{-2}$
$t\bar{t}$	461160	8×10^{-2} $\pm2\times10^{-2}$	-
$Z \to ee + 2p$	5990	3.2×10^{-3} $\pm4\times10^{-4}$	-
$Z \to ee + 3p$	4930	2.8×10^{-3} $\pm4\times10^{-4}$	-
$Z \to ee + 4p$	2410	9×10^{-4} $\pm4\times10^{-4}$	-
$Z \to ee + 5p$	1270	3×10^{-3} $\pm1.2\times10^{-2}$	-
$Z \to \mu\mu + 2p$	5050	1.1×10^{-2} $\pm1\times10^{-3}$	-
$Z \to \mu\mu + 3p$	4510	5.1×10^{-3} $\pm6\times10^{-4}$	-
$Z \to \mu\mu + 4p$	2290	1.1×10^{-3} $\pm3\times10^{-4}$	-
$Z \to \mu\mu + 5p$	1230	1×10^{-4} $\pm2\times10^{-4}$	-
$Z \to \tau\tau + 0p$	2220	-	-
$Z \to \tau\tau + 1p$	1960	7×10^{-3} $\pm2\times10^{-3}$	4×10^{-2} $\pm3\times10^{-2}$
$Z \to \tau\tau + 2p$	2500	2.5×10^{-2} $\pm2\times10^{-3}$	4×10^{-2} $\pm1\times10^{-2}$
$Z \to \tau\tau + 3p$	2010	1.6×10^{-2} $\pm2\times10^{-3}$	3×10^{-2} $\pm1\times10^{-2}$
$Z \to \tau\tau + 4p$	1110	3×10^{-3} $\pm1\times10^{-3}$	5×10^{-3} $\pm5\times10^{-3}$
$Z \to \tau\tau + 5p$	590	4×10^{-4} $\pm9\times10^{-4}$	-
$W \to e\nu + 2p$	67500	3×10^{-3} $\pm5\times10^{-3}$	-
$W \to e\nu + 3p$	49300	-	-
$W \to e\nu + 4p$	25800	1×10^{-2} $\pm3\times10^{-2\dagger}$	-
$W \to e\nu + 5p$	13300	3×10^{-3} $\pm6\times10^{-3\dagger}$	-
$W \to \mu\nu + 2p$	61700	-	-
$W \to \mu\nu + 3p$	46300	3×10^{-3} $\pm4\times10^{-3\dagger}$	-
$W \to \mu\nu + 4p$	24300	2×10^{-2} $\pm1\times10^{-2\dagger}$	-
$W \to \mu\nu + 5p$	13300	-	-
W^+W^-	111600	1.1×10^{-1} $\pm6\times10^{-2\dagger}$	-
W^+Z^0	14750	6×10^{-4} $\pm4\times10^{-4}$	-
W^-Z^0	29370	4×10^{-3} $\pm2\times10^{-3}$	-
Z^0Z^0	18390	1×10^{-3} $\pm1\times10^{-3}$	-

Table 6.9: Initial and final cross-sections for signal and background processes in the di-lepton channel. Estimates (with statistical errors) for final cross-sections are given both from direct calculation (where available), and also using the cut factorisation method (CFM). In several modes the mass window cut removes all events and so in these cases the 'mass-window' cut was not included in the calculation. These are indicated by a †.

	$\sigma_{Start}\ (fb)$	$\sigma_{End}^{CFM}\ (fb)$	$\sigma_{End}^{Direct}\ (fb)$
$H \to \tau\tau$	145	$2.36\times10^{-1}\ \pm8\times10^{-3}$	$4.9\times10^{-1}\ \pm3\times10^{-3}$
$t\bar{t}$	461160	$1.3\times10^{-2}\ \pm6\times10^{-3}$	-
$Z \to ee + 2p$	5990	$2.0\times10^{-3}\ \pm5\times10^{-4}$	-
$Z \to ee + 3p$	4930	$1.2\times10^{-3}\ \pm4\times10^{-4}$	-
$Z \to ee + 4p$	2410	$4\times10^{-4}\ \pm3\times10^{-4}$	-
$Z \to ee + 5p$	1270	-	-
$Z \to \mu\mu + 2p$	5050	$8\times10^{-4}\ \pm4\times10^{-4}$	-
$Z \to \mu\mu + 3p$	4510	-	-
$Z \to \mu\mu + 4p$	2290	-	-
$Z \to \mu\mu + 5p$	1230	-	-
$Z \to \tau\tau + 0p$	2220	-	-
$Z \to \tau\tau + 1p$	1960	$1\times10^{-2}\ \pm2.7\times10^{-3}$	-
$Z \to \tau\tau + 2p$	2500	$5\times10^{-2}\ \pm4.7\times10^{-3}$	$4\times10^{-2}\ \pm1\times10^{-2}$
$Z \to \tau\tau + 3p$	2010	$3\times10^{-2}\ \pm3.1\times10^{-3}$	$3\times10^{-2}\ \pm1\times10^{-2}$
$Z \to \tau\tau + 4p$	1110	$7\times10^{-3}\ \pm1\times10^{-3}$	$5\times10^{-3}\ \pm6\times10^{-3}$
$Z \to \tau\tau + 5p$	0590	$6\times10^{-4}\ \pm4\times10^{-4}$	-
$W \to e\nu + 2p$	67500	$2\times10^{-2}\ \pm2\times10^{-2\dagger}$	-
$W \to e\nu + 3p$	49300	$8\times10^{-3}\ \pm6\times10^{-3}$	$5\times10^{-1}\ \pm5\times10^{-1}$
$W \to e\nu + 4p$	25800	$1\times10^{-3}\ \pm1\times10^{-3}$	-
$W \to e\nu + 5p$	13300	-	-
$W \to \mu\nu + 2p$	61700	$3\times10^{-3}\ \pm3\times10^{-3}$	-
$W \to \mu\nu + 3p$	46300	$1.7\times10^{-1}\ \pm6\times10^{-2\dagger}$	-
$W \to \mu\nu + 4p$	24300	$1\times10^{-3}\ \pm1\times10^{-3}$	-
$W \to \mu\nu + 5p$	13300	$3\times10^{-4}\ \pm3\times10^{-4}$	-
W^+W^-	111600	$8\times10^{-3}\ \pm1.2\times10^{-2\dagger}$	-
W^+Z^0	14750	$6\times10^{-4}\ \pm9\times10^{-4}$	-
W^-Z^0	29370	$1\times10^{-2}\ \pm2\times10^{-2\dagger}$	-
Z^0Z^0	18390	-	-

Table 6.10: Initial and final cross-sections for signal and background processes in the lepton-hadron channel. Estimates (with statistical errors) for final cross-sections are given both from direct calculation (where available), and also using the cut factorisation method (CFM). In several modes the mass window cut removes all events and so in these cases the 'mass-window' cut was not included in the calculation. These are indicated by a †.

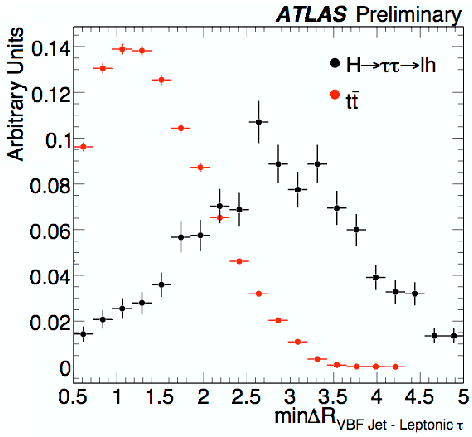

Figure 6.11: Minimum angle between forward jet and leptonically decaying τ, for signal and $t\bar{t}$ background.

with the separation generally being considerably smaller in $t\bar{t}$ events than in signal events.

$t\bar{t}$ Monte Carlo samples were combined in the correct proportions with $Z \rightarrow \tau^+\tau^- + 2/3/4/5$ *jets* samples and the ratio of signal to background for each of the four variables; $\Delta\eta_{jj}$, M_{jj}, ΔR_{jl}^{min} and ΔR_{jh}^{min} (where ΔR_{jl}^{min} and ΔR_{jh}^{min} are the minimum separations between the leptonic/hadronic τ and forward jet respectively). Fits were obtained for these ratios for each parameter and then the overall log likelihood ratio (LLR) is calculated as given in equation 6.2.

$$LLR = log(y\Delta\eta_{jj}) + log(yM_{jj}) + log(y\Delta R_{jl}^{min}) + log(y\Delta R_{jh}^{min}) \qquad (6.2)$$

where y is the signal to background ratio for each of the four variables.

Again, quite different distributions arise for signal and background and placing a cut on the log likelihood ratio value at -2.5 appears to optimise the figure of merit $S/\sqrt{S+B}$ (figures 6.12(a) and 6.12(b)). If the cut flows are calculated again, but replacing the aforementioned cuts with a cut on the log likelihood ratio at -2.5, the $t\bar{t}$ background is shown to be suppressed by a further factor of 10 (using the Cut Factorisation Method), whilst the final cross-section for signal

events actually increases slightly. Although this result may be a little optimistic (due to the small sample size), the method appears promising and should be further investigated as a possible analysis technique.

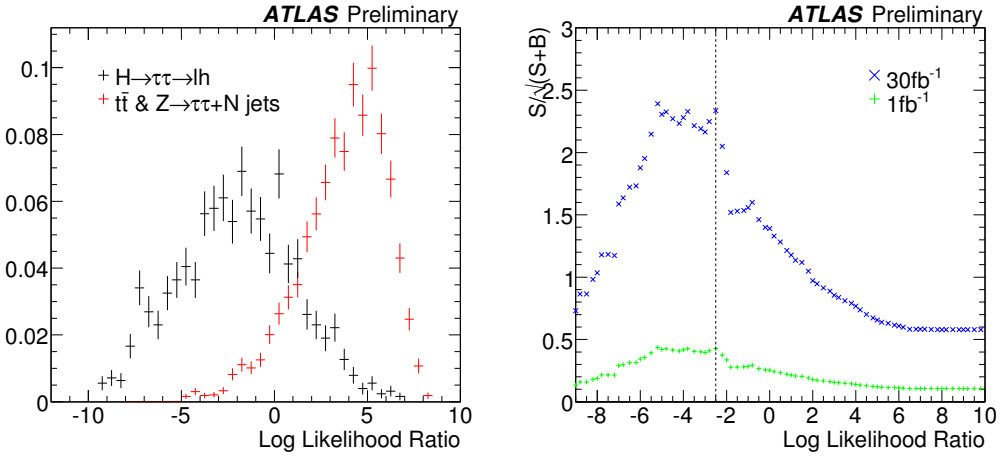

(a) (b)

Figure 6.12: Optimising topological cuts in the lepton-hadron channel: (a) Distributions of the log likelihood ratios for signal and combined $t\bar{t}$ and $Z \rightarrow \tau\tau$ backgrounds. (b) The figure of merit $S/\sqrt{(S+B)}$ is used to optimise a cut on the log likelihood ratio. A cut on LLR > -2.5 is applied to the analysis.

6.7 Summary and Conclusions

It has been established in sections 6.3.1, 6.3.2 and 6.3.3 that the four main classes of $t\bar{t}$ background are the decay modes where:

1. The final state at truth level includes a tau ($WW \rightarrow e/\mu + \tau$) – lines 1 and 5 in table 6.4.

2. The final state at truth level includes a hadronic jet which fakes a tau ($WW \rightarrow e/\mu + jet$) – lines 2 and 6 in table 6.4.

3. The final state at truth level includes two leptons (electrons or muons) from W-decays, but one of these is missed and a jet from somewhere else fakes

a hadronic tau (lepton-hadron channel) – lines 3 and 4 in table 6.4 and discussion in section 6.3.2.

4. The b-quark from the top decay subsequently decays to a lepton and this masquerades as a leptonically decaying tau (section 6.3.3).

By requiring opposite-sign charges on the tau daughters, and by vetoing any event which has a jet with a b-tagging weight more than 1.0, the $t\bar{t}$ background can be suppressed by approximately 30% in both channels, whilst still maintaining 85% of signal events. The b-jet veto appears to be particularly efficient at removing $t\bar{t}$ background events, although it should be noted that the tracker acceptance is $|\eta| < 2.5$ and even with soft leptons, b-tagging outside this region ($|\eta| > 2.5$), where there is by definition no inner detector track, is likely to be extremely difficult, if not impossible. Although this has been taken into account in the results presented here, since samples with full detector simulation were used, once data taking is well underway and the detectors are better understood, the study should be repeated to re-optimise the cut and obtain better estimates of the efficiency.

Using a log-likelihood method to optimise the topological cuts was shown to be very effective as a means to suppress $t\bar{t}$ background further (by an extra factor of 10). Although this initial result is probably over-optimistic, it serves to highlight the usefulness of this analysis technique and should be further investigated.

The cuts applied to select Higgs events decaying to two tau leptons are effective at suppressing backgrounds and the available background samples are rarely large enough to allow any direct estimation of final cross-sections from cut flows. Methods like the 'cut factorisation method' can be employed to give an 'order-of-magnitude' estimate of the cross-sections for individual backgrounds once all cuts have been made. From this, it can be established that the event selection criteria have a rejection power of 10^6-10^8 for most backgrounds.

Chapter 7

MSSM Higgs to Tau Tau Search Strategy

7.1 Introduction

In this chapter MSSM Higgs boson production and subsequent decay to two tau leptons is discussed. Only the lepton-hadron mode (see table 6.1) is considered here. Monte Carlo simulations of the $A \to \tau\tau$ process were used to model the $\phi \to \tau\tau$ signal, although mass degeneracy effects enhance this cross-section by a factor of $\sim$2 ($M_A \approx M_h$ for $M_A \leq 130$ GeV and $M_A \approx M_H$ for $M_A \geq 130$ GeV). Analysis performance at a centre-of-mass energy of 7 TeV is considered, and production cross-sections are given based on this energy. Due to it's relatively large production cross-section times branching ratio to tau-pairs, it should be possible to set limits on the $\phi \to \tau\tau$ process using data from the 2010-2011 LHC run. With this in mind, analysis robustness during this early data-taking period is a priority.

The basic experimental signature consists of one leptonically decaying tau (to an electron or muon) plus one hadronically decaying tau. These are accompanied by missing E_T due to the presence of neutrinos from the tau decays. In addition to requirements on these objects, cuts based on decay topology and jets can be

Gluon fusion		Associated production	
M_A (GeV)	Cross-Section (pb)	M_A (GeV)	Cross-Section (pb)
90	10.7	90	7.79
100	6.33	100	5.67
110	3.97	110	4.22
120	2.56	120	3.14
130	1.65	130	2.44
140	1.16	140	1.89
150	0.804	150	1.49
170	0.410	170	0.95
200	0.162	200	0.504
250	0.0419	250	0.197
300	0.0117	300	0.0802

Table 7.1: Summary of the signal mass points processes considered (with $\tan\beta = 20$) and their initial NLO cross-sections in pb. Cross-sections provided by the ATLAS Higgs cross-section working group [44, 45, 46, 47].

made.

7.1.1 Signal Monte Carlo Samples

The gluon-fusion production signal process was modelled using PYTHIA [39] with parton distribution functions (PDF) modelled by MRST [40]. SHERPA [41], with the CTEQ6L1 [42] PDF set was used to simulate A-boson production in association with b-jets. Tau decays were modelled using Tauola [43] for both production modes. Mass points of M_A = 90, 100, 110, 120, 130, 140, 150, 170, 200, 250 and 300 GeV were available for both production modes. Signal cross-sections (in pb) at $\tan\beta = 20$ are provided in table 7.1.

7.2 Backgrounds

With a true di-tau final state and very similar event kinematics, the $Z \to \tau\tau$ process is largely irreducible and therefore provides the dominant source of background to the analysis. It is particularly important in low mass scenarios where

the signal falls on the tail of the Z-peak.

W+jets decays provide the other main source of background due to its large production cross-section and the possibility to have a lepton plus missing transverse energy in the final state (in the case of $W \rightarrow e/\mu/\tau_l + \nu$). Hadronic jets accompanying this process can fake a hadronic tau.

The $t\bar{t}$ process ($t\bar{t}\rightarrow WbWb$, $W \rightarrow e/\mu/\tau + \nu$ or jets, see figure 6.4) gains in importance as M_A increases. This mechanism provides the possibility to have real leptons or hadronic taus in the final state. There are b-jets present in both the signal and $t\bar{t}$ processes. In addition to this problem, there is also potential for leptonic b-decays to be reconstructed as leptonic tau decays. Finally, there is the possibility for jets in the event to fake hadronic taus.

Single top production (see figure 7.1) will also contribute as a background to the analysis, predominantly via the t-channel which has the largest cross-section, and by associated production, where the presence of a second W-boson in the event provides further scope for reconstructing a lepton plus hadronic tau final state. The single top process also includes one or two b-jets in the final state.

Other contributing processes include $Z \rightarrow ee$, $Z \rightarrow \mu\mu$, and QCD jet production. All background processes considered and their corresponding cross-sections are listed in table 7.2.

7.2.1 Background Monte Carlo Samples

W and Z backgrounds were modelled using CTEQ6L1 and ALPGEN [48], which employs the MLM technique [49] to match the hard process (calculated with a leading-order matrix element for up to 5 jets) to the parton shower of HERWIG [36]. The $t\bar{t}$ and single top processes were generated with MC@NLO [38] and CTEQ6.6 [42]. QCD processes were simulated using PYTHIA, with MRST to model the PDF. Samples with a filter requiring at least one lepton in the event was applied to the QCD samples to avoid the generation of events which will be rejected at the first cut were also available. Tau decays in all processes were

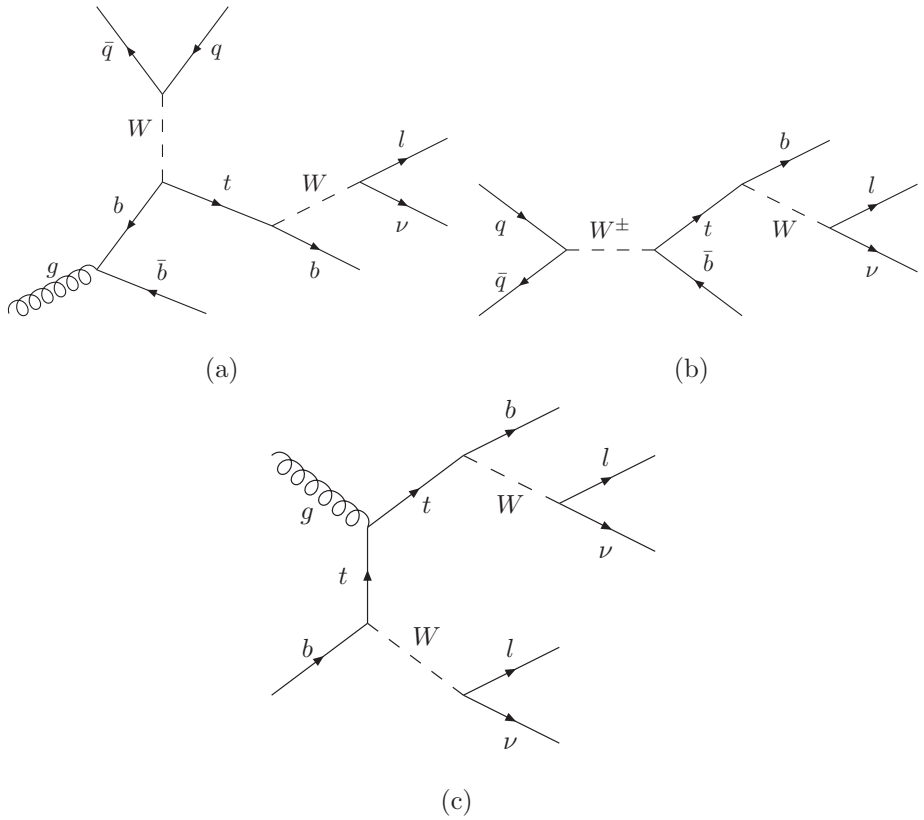

Figure 7.1: Feynman representations of single top production; t-channel (a), s-channel (b) and associated production (c).

simulated using TAUOLA [43]. The analysis was done using a full GEANT [50] simulation of the ATLAS detector, including realistic misalignments and distortions.

7.3 Lepton Selection

The final state should include either an electron or a muon and these objects are used to trigger on candidate events. The lowest pre-scaled triggers expected for the 2010-2011 LHC run for each object are a 'medium-quality' electron with $p_T > 10$ GeV or a muon with $p_T > 10$ GeV. The triggered electron (muon) candidates are required to meet the requirements detailed in section 5.1 (5.2). A further cut of 15 GeV on the lepton p_T is made to reduce background contributions (pre-

Process	Cross-Section (pb)
$W \rightarrow e\nu_e$	1.06 $\times 10^4$
$W \rightarrow \mu\nu_\mu$	1.06 $\times 10^4$
$W \rightarrow \tau\nu_\tau$	1.05 $\times 10^4$
$Z \rightarrow ee$	1.04 $\times 10^3$
$Z \rightarrow \mu\mu$	1.03 $\times 10^3$
$Z \rightarrow \tau\tau$	1.03 $\times 10^3$
$t\bar{t}$	87.4
Single Top (associated production)	14.6
Single Top (t-channel, $W \rightarrow e/\mu/\tau$)	21.5
Single Top (s-channel, $W \rightarrow e/\mu/\tau$)	1.41
QCD di-jet production ($\hat{p_T} \geq$8 GeV)	1.047$\times 10^9$
QCD (single electron filter, 17$\leq \hat{p_T} <$140 GeV)	1.170$\times 10^6$
QCD (single muon filter, $\hat{p_T} \geq$8 GeV)	1.887$\times 10^6$
QCD (filter for fake electron objects, $\hat{p_T} \geq$17 GeV)	9.769$\times 10^7$

Table 7.2: Background processes considered and their initial NLO (LO for QCD) cross-sections in pb. For the QCD samples, $\hat{p_T}$ is the transverse momentum of the two partons involved in the hard scatter.

dominantly from QCD) from low p_T leptons. The transverse momentum spectra of electrons and muons for signal and QCD (single lepton filter) background are shown in figure 7.2.

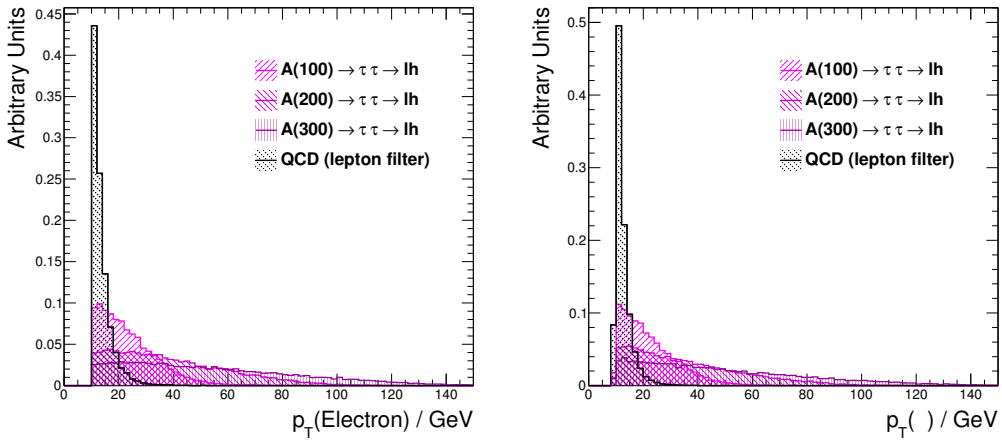

(a) Electron p_T (b) Muon p_T

Figure 7.2: Lepton p_T for signal (M_A = 100, 200, 300 GeV) and QCD (single lepton filter) processes.

7.4 Choice of Tau ID Variable

Since this analysis is concerned with discovery and exclusion prospects of the MSSM Higgs during the early LHC data-taking period (up to 1 fb^{-1}at $\sqrt{s}$ = 7 TeV), a fully optimised, likelihood based tau ID will not be available and so a simpler safe tau ID should be used.

Two different algorithms for tau identification are available at ATLAS - one which uses only calorimeter based variables ('TauCutSafeCalo'), and the other which uses information from both the calorimeter and tracking detectors ('TauCutSafe'). Each of these is available in three settings - loose (high efficiency but poor rejection against fakes), medium and tight (low efficiency but high purity). A full review of tau identification at ATLAS, including strategies for the early data-taking period, can be found in section 5.3.1.

When only those backgrounds which contain real taus (e.g. $Z \to \tau\tau$) are considered, better performance using the 'loose' levels of tau-ID is observed. Taking into account only 'fake tau backgrounds' (i.e. those where an object (*e.g.* a jet) fakes a hadronic tau - $t\overline{t}$, $W \to e\nu$, $W \to \mu\nu$, $W \to \tau_l\nu$ and QCD) the 'tight' levels provide a larger significance ($S/\sqrt{B}$), as expected. Once all background processes are taken into account we observe that the medium level provides the best significance.

The performance of the two different 'medium' safe tau identification variables as a function of tau p_T is evaluated, using $S/\sqrt{B}$ as the figure of merit. The results for $M_A = 120$ GeV are shown in figure 7.3(a). From this we observe that the 'TauCutSafeMedium' identification provides a better performance. A cut at 20 GeV is made at the object pre-selection stage (which gives rise to the flat section in the 0-20 GeV region in figure 7.3(a)) but this is tightened to 30 GeV to improve the signal-to-background ratio. The p_T distributions for signal and QCD processes (the dominant source of fake taus) are shown in figure 7.3(b).

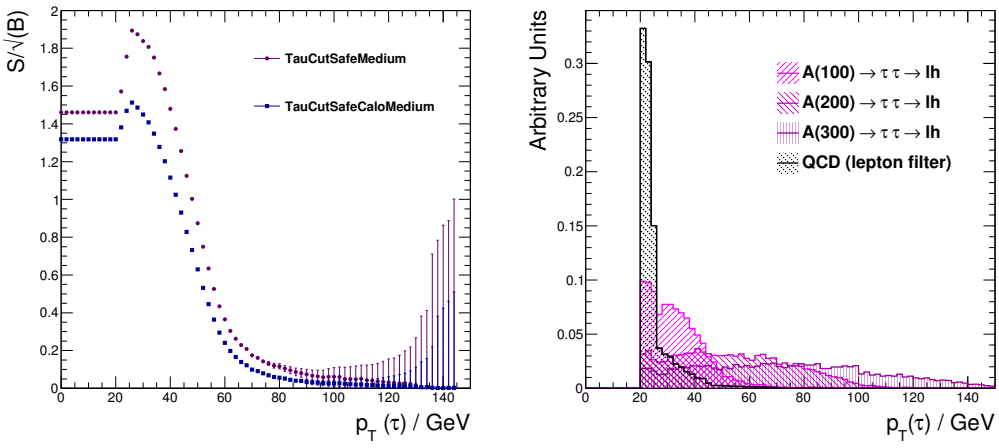

(a) (b)

Figure 7.3: 7.3(a): Significance ($S/\sqrt{B}$) as a function of tau p_T for two choices of tau ID - one which utilises only information from the calorimeter ('TauCutSafeCaloMedium'), and one which uses both tracking and calorimeter variables ('TauCutSafeMedium') - for a Higgs mass of 120 GeV. 7.3(b): Tau p_T for signal (M_A = 100, 200, 300 GeV) and QCD (single lepton filter) processes.

7.5 Missing Energy

There should always be a significant amount of missing transverse energy in any process involving taus, due to the presence of neutrinos. To suppress contributions from processes with no true missing energy (QCD and $Z \rightarrow ee/\mu\mu$), at least 20 GeV of missing E_T is required. Missing E_T distributions for signal (M_A = 100, 200 and 300 GeV), $Z \rightarrow ee/\mu\mu$, and QCD (single lepton filter) are shown in figure 7.4.

7.6 Angular Correlations

Fundamental differences in decay topology can be exploited to separate signal from background. Since the parent particle ($h/A/H$) is many times heavier than the taus it is decaying into, one would expect that these taus would be heavily

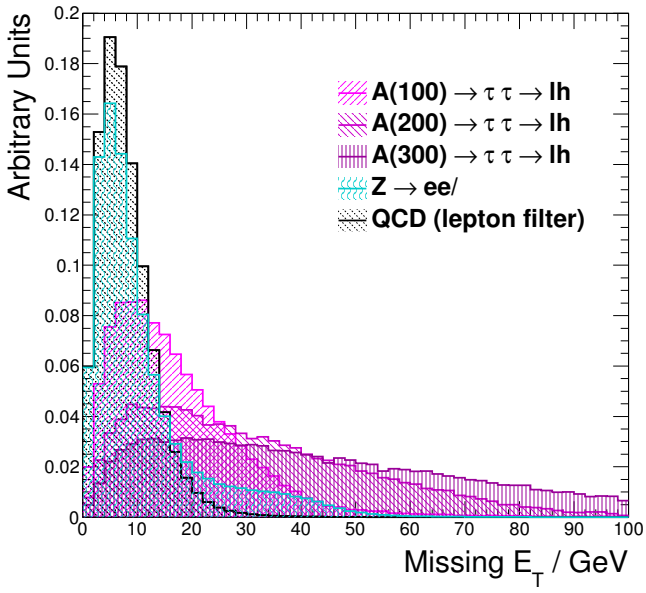

Figure 7.4: Missing E_T distributions for signal (M_A = 100,200 and 300 GeV), $Z \to ee/\mu\mu$, and QCD (single lepton filter)

boosted and the tau decay products can therefore be approximated to have the same trajectory as the taus themselves. Furthermore, it is likely that the taus will be back-to-back.

A leptonically decaying tau will be accompanied by two neutrinos, whereas a hadronically decaying tau will produce just one. Thus, in the lepton-hadron decay mode considered in this analysis, the difference in the amount of missing transverse energy ($\not\!\!E_T$) from each parent tau should result in an imbalance in the overall direction of the total missing E_T. This is illustrated in figure 7.5.

Figure 7.6 shows the different distributions of $cos(\phi_{lepton} - \phi_{\not\!\!E_T})$ vs. $cos(\phi_\tau - \phi_{\not\!\!E_T})$ for signal and major background processes. The plots are made after requiring that events have exactly one lepton with $p_T >$ 15 GeV, exactly one 'TauCutSafeCaloMedium' tau-jet (see section 5.3.1) with $p_T >$ 20 GeV and opposite charge to the lepton, and finally, at least 20 GeV of missing transverse energy in the event.

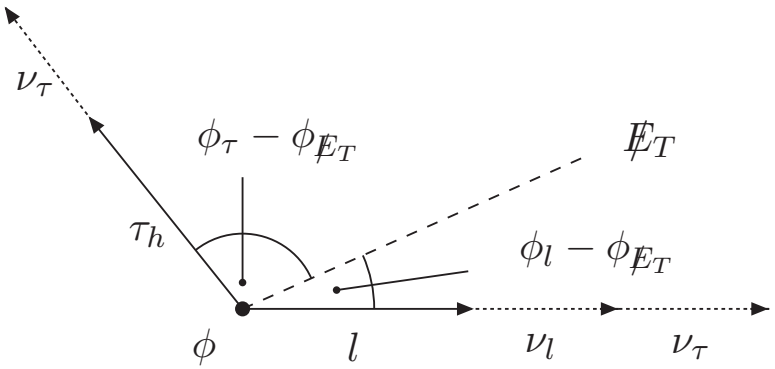

Figure 7.5: A schematic of $A \to \tau\tau$ decay in the detector.

$Z \to \tau\tau$ has a very similar distribution to the signal process, as expected because of its virtually identical event topology. Other backgrounds have very different distributions to the signal though, and it is these differences which can be exploited to further reduce the total background contribution. Applying a cut based on these variables is simplified by rotating these distributions by 90° ($\pi/4$), in either a clockwise ($\theta = -\pi/4$) or anti-clockwise direction ($\theta = +\pi/4$) as described below:

$$\begin{pmatrix} x \\ y \end{pmatrix} = \begin{pmatrix} cos(\phi_l - \phi_{\not\!\!E_T}) \\ cos(\phi_\tau - \phi_{\not\!\!E_T}) \end{pmatrix}$$

$$\begin{pmatrix} x' \\ y' \end{pmatrix} = \begin{pmatrix} cos\theta & -sin\theta \\ sin\theta & cos\theta \end{pmatrix} \begin{pmatrix} x \\ y \end{pmatrix}$$

Thus x' solves to:

$$x' = \frac{1}{\sqrt{2}} \left(cos(\phi_l - \phi_{\not\!\!E_T}) + cos(\phi_\tau - \phi_{\not\!\!E_T}) \right), \text{ for } \theta = -\frac{\pi}{4}$$

and

$$x' = \frac{1}{\sqrt{2}} \left(cos(\phi_l - \phi_{\not\!\!E_T}) - cos(\phi_\tau - \phi_{\not\!\!E_T}) \right), \text{ for } \theta = +\frac{\pi}{4}.$$

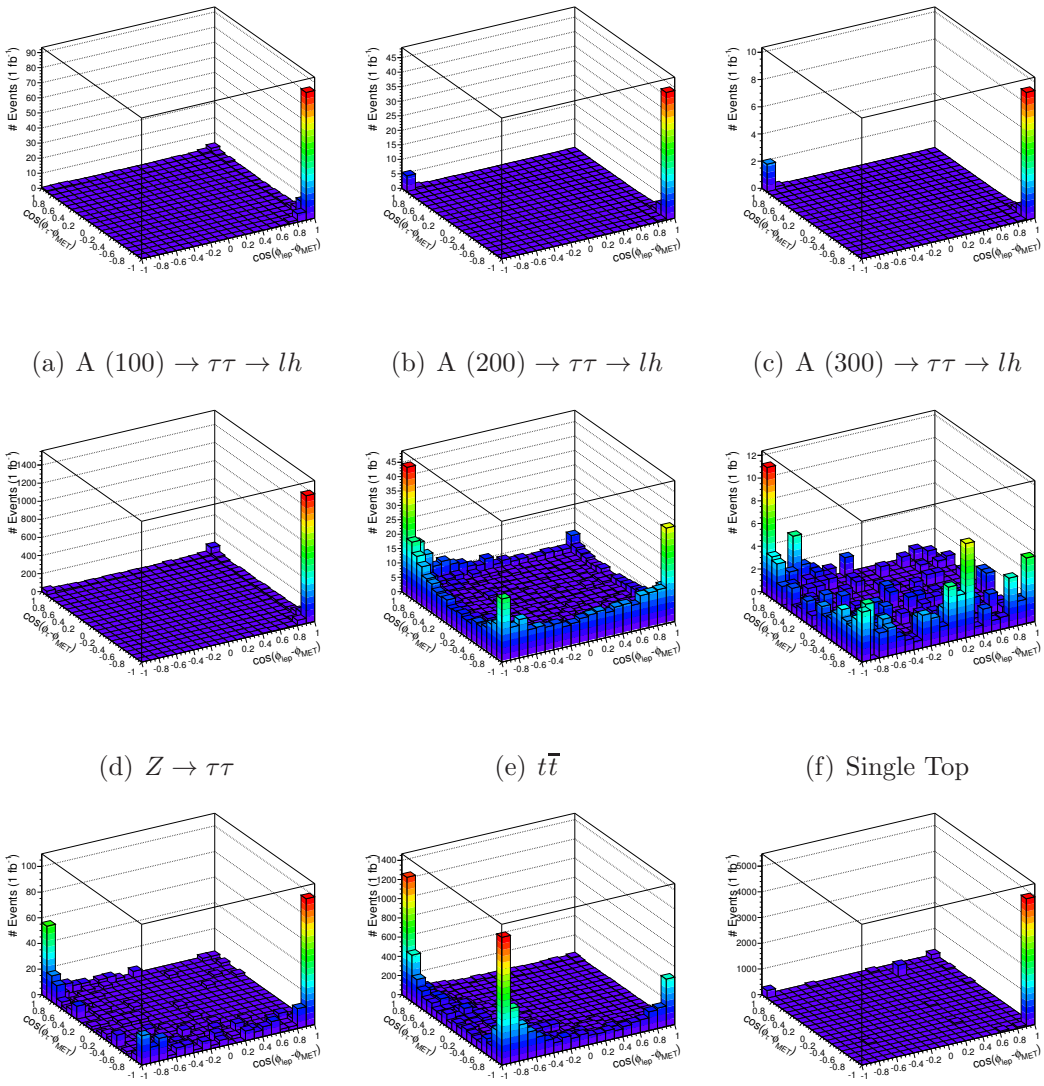

(a) A (100) $\rightarrow \tau\tau \rightarrow lh$ (b) A (200) $\rightarrow \tau\tau \rightarrow lh$ (c) A (300) $\rightarrow \tau\tau \rightarrow lh$

(d) $Z \rightarrow \tau\tau$ (e) $t\bar{t}$ (f) Single Top

(g) $Z \rightarrow ee/\mu\mu$ (h) $W \rightarrow e/\mu/\tau_l + \nu$ (i) QCD

Figure 7.6: Distributions of $cos(\phi_l - \phi_{\not\!\!E_T})$ vs. $cos(\phi_\tau - \phi_{\not\!\!E_T}))$ for signal and background processes.

The transverse mass between the lepton and the missing E_T can also be used to separate signal from W and $t\bar{t}$ backgrounds (in the latter because the lepton and missing E_T originate from a W-boson decay). The transverse mass is defined to be:

$$M_T = \sqrt{2p_T(l) \cdot \not{E}_T \cdot \Big(1 - cos(\phi_l - \phi_{\not{E}_T})\Big)}$$

From figures 7.6(a)-7.6(c) it is clear that the majority of the signal is clustered in the $cos(\phi_l - \phi_{\not{E}_T}) = +1$, $cos(\phi_\tau - \phi_{\not{E}_T}) = -1$ region. Since the equation for transverse mass also includes a $cos(\phi_l - \phi_{\not{E}_T})$ term, the transverse mass should be small for the signal process.

Plots of the distributions of $cos(\phi_l - \phi_{\not{E}_T}) + cos(\phi_\tau - \phi_{\not{E}_T})$ (clockwise rotation) and $cos(\phi_l - \phi_{\not{E}_T}) - cos(\phi_\tau - \phi_{\not{E}_T})$ (anti-clockwise rotation) for signal and backgrounds ($W \to e/\mu/\tau_l + \nu$, $t\bar{t}$, single top, and $Z \to ee/\mu\mu$) are shown in figures 7.7(a) and 7.7(b) respectively. Also shown are the distributions for $cos(\phi_l - \phi_\tau)$ in figure 7.7(c) and the transverse mass between the lepton and the missing E_T in figure 7.7(d). $Z \to \tau\tau$ is not shown because it is kinematically similar to the $\phi \to \tau\tau$ process and has a similar distribution (see figure 7.6). It is however considered when calculating efficiencies and significances, see below.

The figure of merit $S/\sqrt{B}$ (at 1 fb^{-1}) is plotted for each of the variables after requiring lepton-hadron type events with at least 20 GeV of missing E_T (cuts 1 to 9 in section 7.9). No QCD samples were included due to the low available statistics of these samples after the event selection cuts have been made. The results obtained with and without the QCD samples are consistent (within errors), but the study should be repeated using a clean sample of QCD extracted from data.

Performance of the different methods for a range of values of M_A are plotted in figure 7.8, together with the corresponding efficiencies (for sample masses of

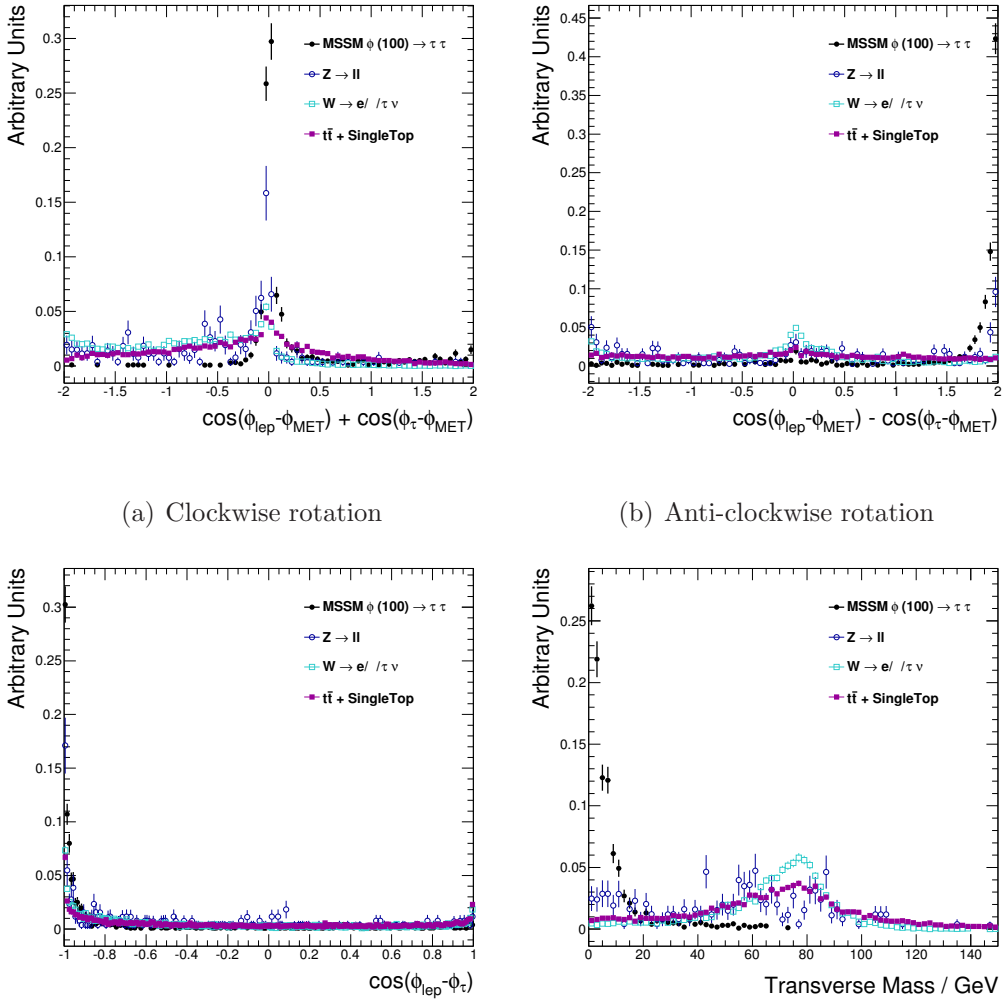

(a) Clockwise rotation

(b) Anti-clockwise rotation

(c) $cos(\phi_l - \phi_\tau)$

(d) Transverse mass

Figure 7.7: Signal (M_A =120 GeV) and background (W, $t\overline{t}$, single top, and $Z \rightarrow ee/\mu\mu$- QCD is not included because of low statistics) distributions of (a) $cos(\phi_l - \phi_{\not\!\!E_T}) + cos(\phi_\tau - \phi_{\not\!\!E_T})$ (corresponding to a clockwise rotation), (b) $cos(\phi_l - \phi_{\not\!\!E_T}) - cos(\phi_\tau - \phi_{\not\!\!E_T})$ (anti-clockwise rotation), (c) $cos(\phi_l - \phi_\tau)$ and (d) the transverse mass between the lepton and the missing E_T.

100, 150, 200 and 300 GeV) in figures 7.9 - 7.12. From these it is observed that a cut on the transverse mass will provide the best performance at lower values of M_A, and comparable performance with other methods at higher M_A.

It should be noted that the general trend indicates that a cut on $cos(\phi_l - \phi_{\not{E}_T}) - cos(\phi_\tau - \phi_{\not{E}_T})$ (anti-clockwise rotation) may be a more suitable choice for a high mass ($M_A >$ ~300 GeV) analysis. At the time of writing, no Monte Carlo simulations of signal processes with $M_A >$ 300 GeV are available and so this is beyond the scope of the analysis.

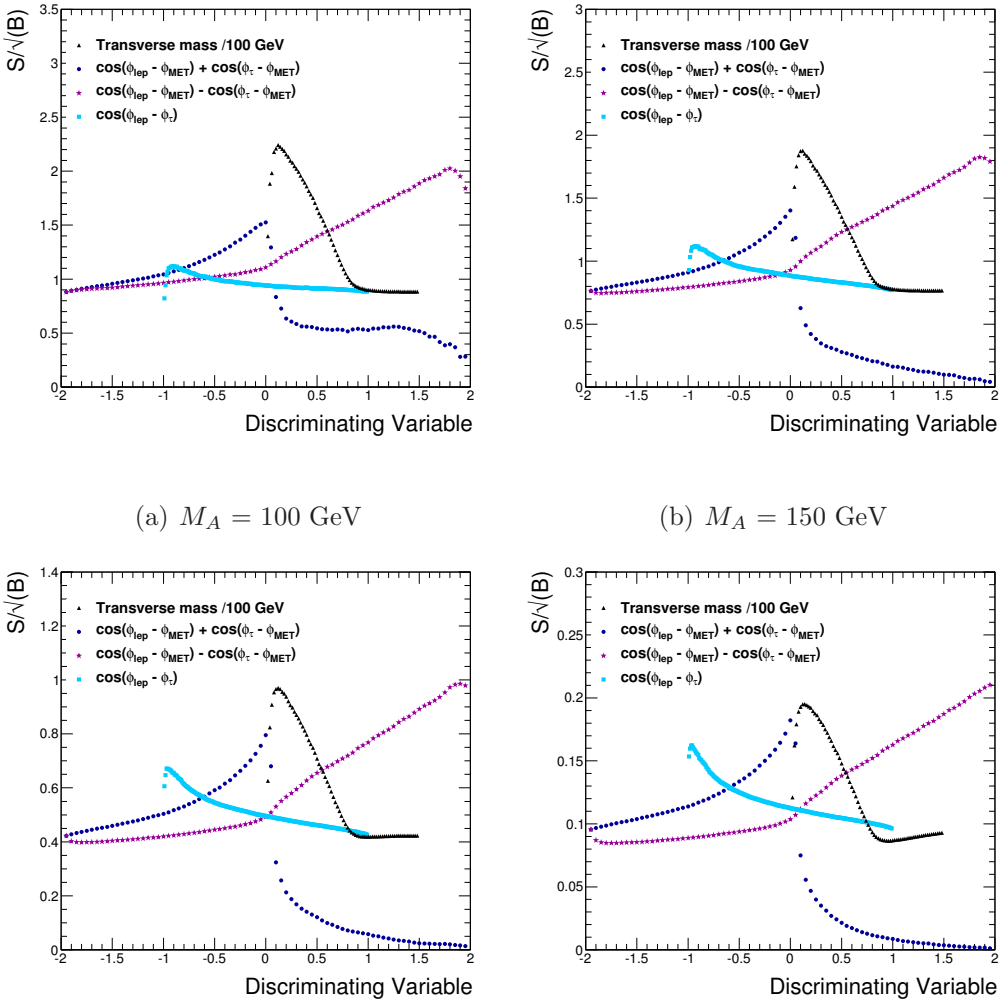

(a) $M_A = 100$ GeV

(b) $M_A = 150$ GeV

(c) $M_A = 200$ GeV

(d) $M_A = 300$ GeV

Figure 7.8: $S/\sqrt{B}$ using different methods to exploit angular correlations between leptons, taus and $\not{E}_T$.

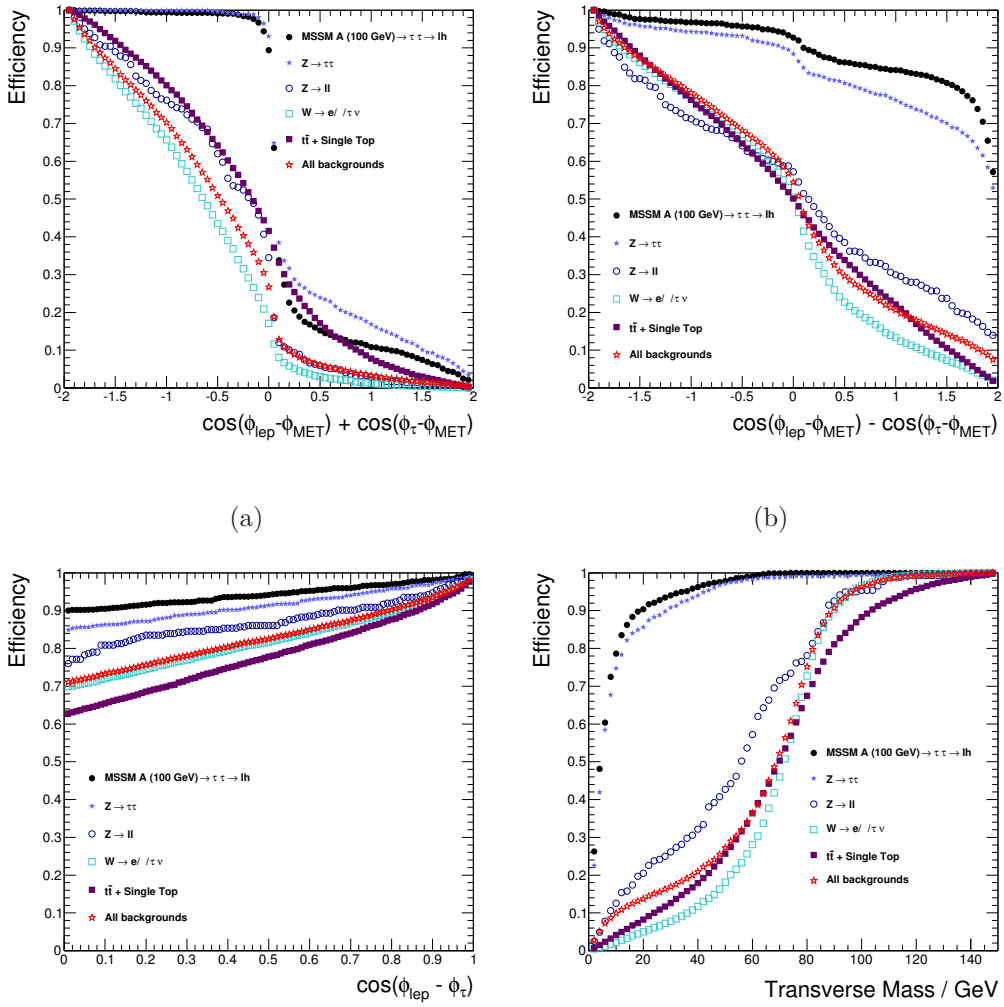

(a) (b)

(c) (d)

Figure 7.9: Efficiencies using different methods to exploit angular correlations between leptons, taus and $\not\!\!E_T$, for $M_A = 100$ GeV.

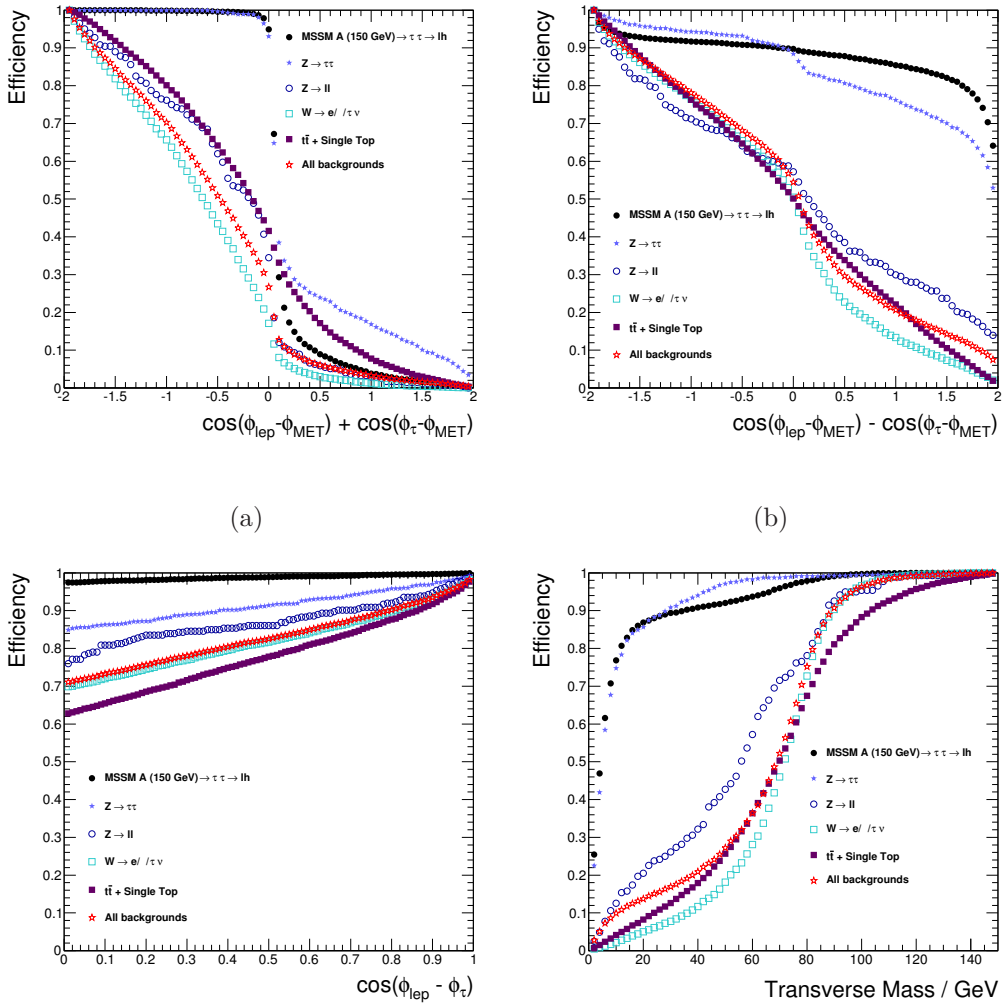

(a) (b)

(c) (d)

Figure 7.10: Efficiencies using different methods to exploit angular correlations between leptons, taus and $\not\!\!E_T$, for $M_A = 150$ GeV.

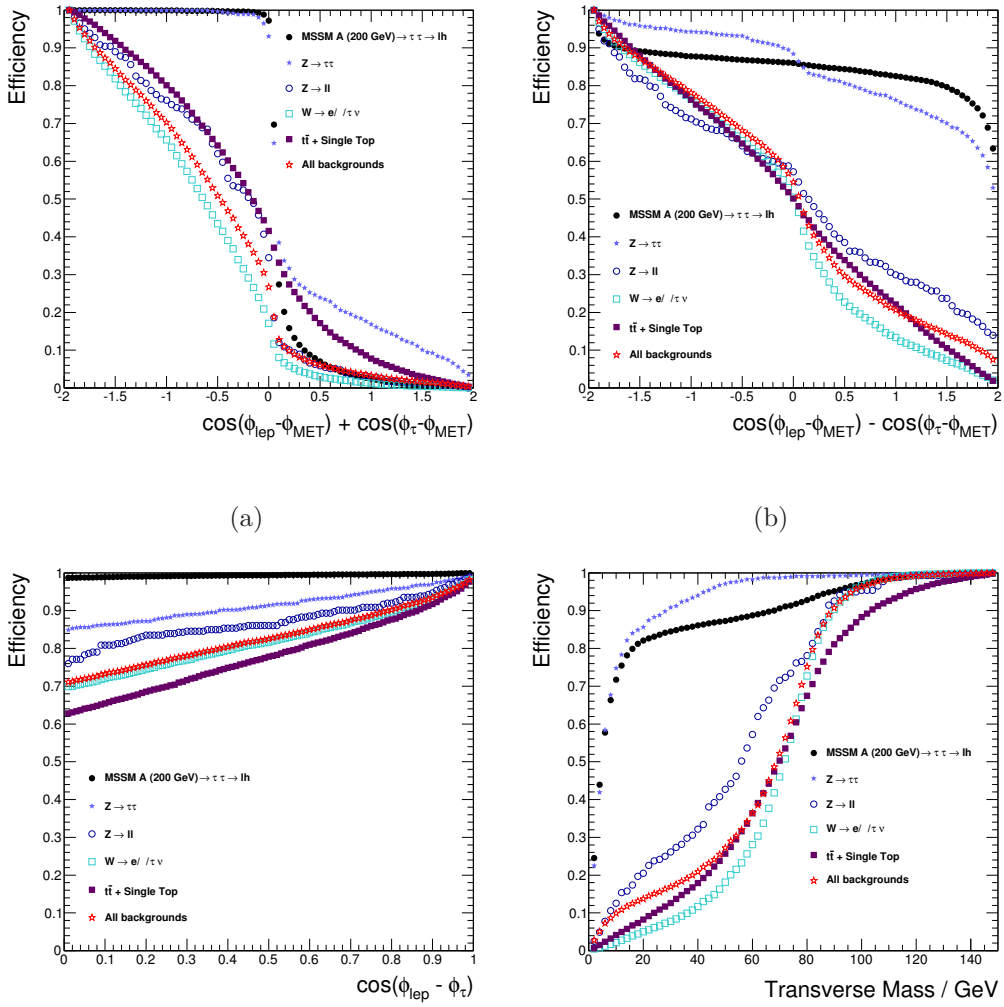

(a) (b)

(c) (d)

Figure 7.11: Efficiencies using different methods to exploit angular correlations between leptons, taus and $\not\!\!E_T$, for $M_A = 200$ GeV.

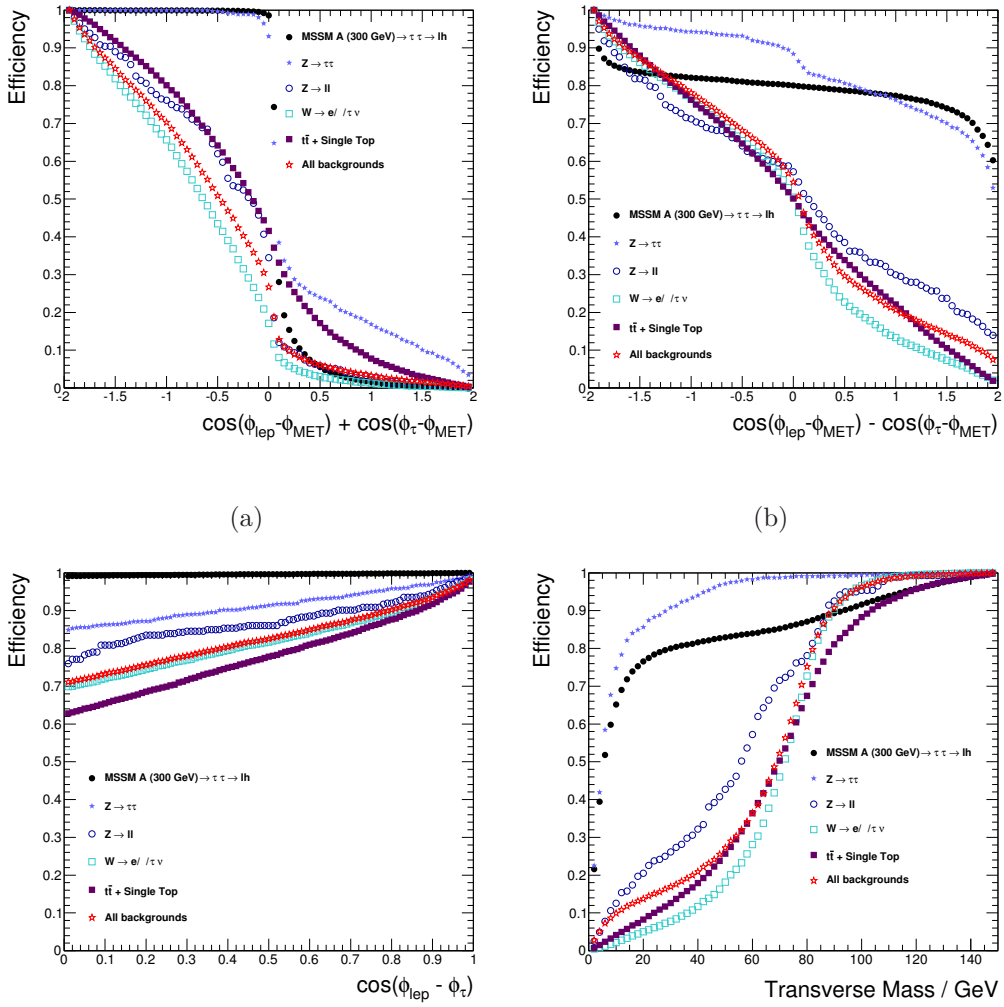

Figure 7.12: Efficiencies using different methods to exploit angular correlations between leptons, taus and $\not\!\!E_T$, for $M_A = 300$ GeV.

7.7 Jet multiplicity

Figure 7.13 shows the jet multiplicity for signal, $t\bar{t}$ and single top background processes. Events were required to have passed the trigger, but no other cuts were imposed.

A cut on the number of jets at $N_{jets} < 3$ removes 74% of $t\bar{t}$ events and 63% of single top events, while maintaining a signal efficiency of approximately 97%.

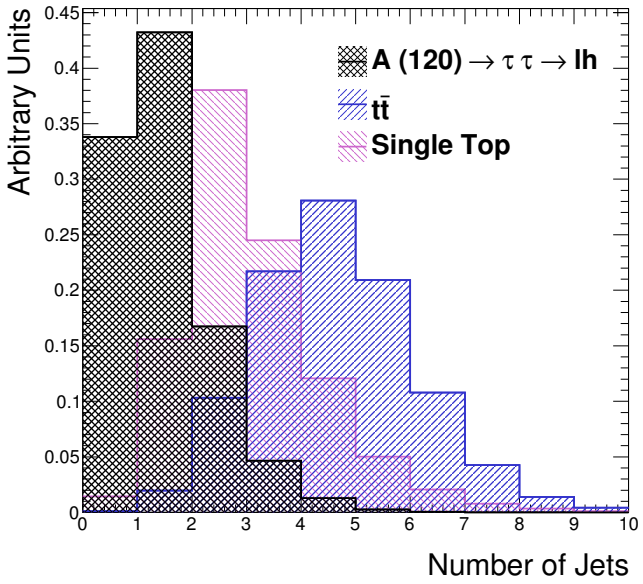

Figure 7.13: Jet multiplicity for signal ($m_\phi = 120\ GeV$), $t\bar{t}$ and single top (s- and t-channels, and associated production) processes.

7.8 Mass Reconstruction

Although the collinear approximation (see appendix A) is used in the VBF $H \rightarrow \tau\tau$ analysis with some success, it's usefulness in the MSSM analysis is unclear for several reasons.

Firstly, the Higgs boson produced via vector boson fusion is heavily boosted and has a higher p_T than its MSSM counterparts and the taus are therefore less back-to-back in the VBF scenario. The collinear approximation breaks down when the angle between the taus approaches 180° and requirements must be made to remove any events with this topology. As was shown in section 7.6, the majority of $A \rightarrow \tau\tau$ decays are produced with the taus produced back-to-back, and indeed exploiting this feature is one of the most powerful tools available for background rejection.

In addition, requirements on the fraction of momentum carried by the visible tau daughter with respect to its parent tau ($x_{l,h}$) must be made. Even with the loosest possible cuts ($\cos\Delta\phi_{\tau-\tau} < 0.95$, $0 < x_l, x_h < 1$) a significant proportion of signal events will be discarded even before a mass window cut is applied. Figure 7.14 shows the distribution of $\cos(\Delta\phi_{\tau-\tau})$, while the distributions of x_l and x_h are given in figure 7.15.

The second motivation for choosing an alternative method of mass reconstruction is to have something simple which can be fully understood during the early stages of data-taking. Two other options are the 'visible' mass (the invariant mass of the visible tau daughters) and the 'effective mass' (the visible mass, plus the missing E_T), both of which are used in other ATLAS analyses. Another option is to try to reconstruct the mass using the collinear approximation where possible, but if this fails the pre-requirements or the mass window cut then the effective mass is taken.

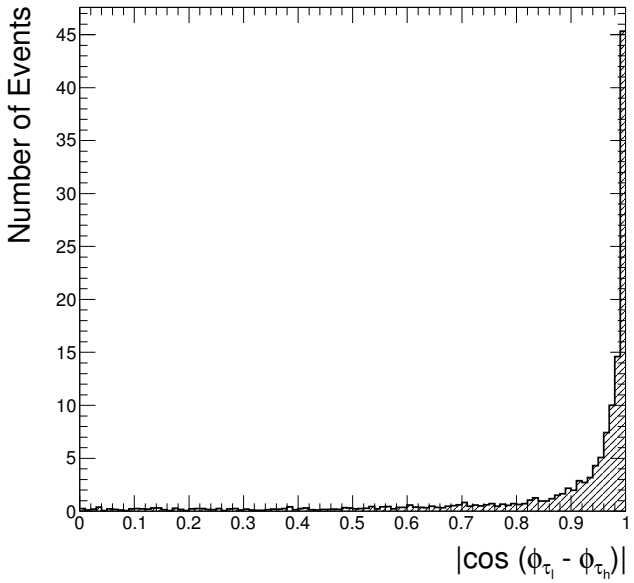

Figure 7.14: Angular separation between the visible tau daughters.

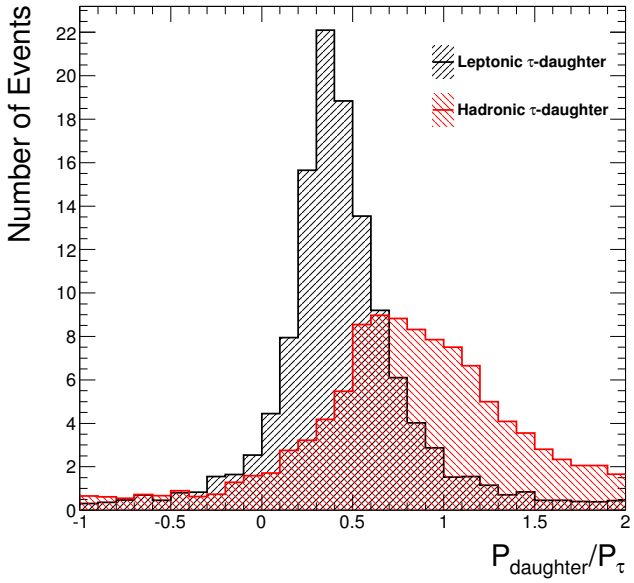

Figure 7.15: Fraction of parent tau's momentum carried by visible daughter.

7.8.1 Corrections to the 'Effective' Mass

The effective mass (M_{eff}) is defined to be the sum of the visible mass (M_{vis}) and the missing E_T, as in the equation below:

$$M_{eff} = M_{vis} + \not{E}_T$$

This assumes that the visible mass and the missing E_T are directly inversely proportional (*i.e.* that if the two variables are plotted against each other then the slope of the line should be equal to -1). Figure 7.16 shows that this is not in fact the case and gradients varying between 0.4 and 0.6 are measured. A 'corrected effective mass' (M_{cor}) can therefore be defined to be:

$$M_{cor} = M_{vis} + \frac{\not{E}_T}{2}$$

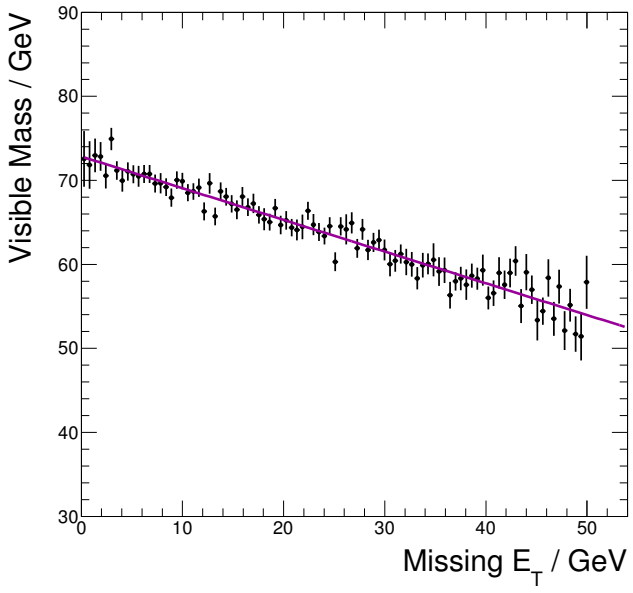

Figure 7.16: Fit to missing E_T as a function of visible mass, for $M_A = 120$ GeV. A cut on $\not{E}_T < 50$ GeV is made to avoid the small number of events which do not meet this criterion skewing the fit of the line.

	Visible		Effective		Corr. Eff.		Collinear	
M_A (GeV)	Low	High	Low	High	Low	High	Low	High
90	30	70	60	100	50	90	70	100
100	40	80	60	110	60	100	70	150
110	50	90	80	110	70	100	90	150
120	60	100	90	130	70	110	100	150
130	60	110	90	140	80	120	110	150
140	60	110	100	140	80	130	120	150
150	70	120	100	150	80	140	130	150
170	80	130	120	170	90	150	130	210
200	80	160	120	200	110	170	190	210
250	90	210	150	240	120	230	190	300
300	100	250	190	290	130	280	280	300

Table 7.3: Summary of the mass window cuts applied when using different methods of mass reconstruction.

7.8.2 Optimisation of Mass Windows

Five different methods of mass reconstruction are considered, as discussed above:

- Visible mass
- Effective mass
- Corrected effective mass
- Collinear approximation
- Combination mass (take the collinear approximation where possible, otherwise try the effective mass)

Mass windows were optimised for each different method at every mass point, using $S/\sqrt{B}$ as the figure of merit and trying all possible combinations of mass window in 10 GeV steps. QCD samples were not included, due to the lack of available statistics. The choice of mass windows for each M_A are summarised in table 7.3. Distributions for the different methods across a range of M_A values are displayed in figures 7.17-7.22.

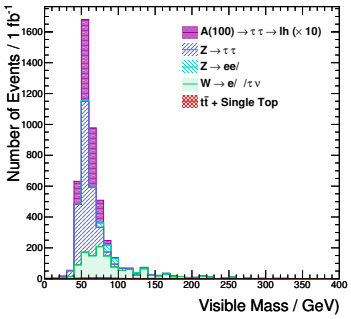

(a) Visible Mass

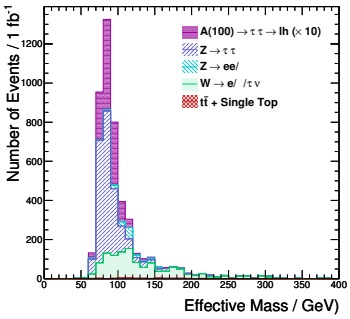

(b) Effective Mass

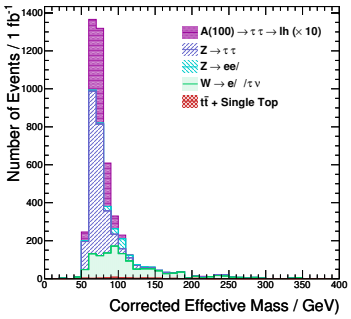

(c) Corrected Effective Mass

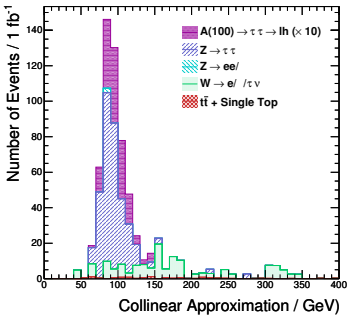

(d) Collinear Approx.

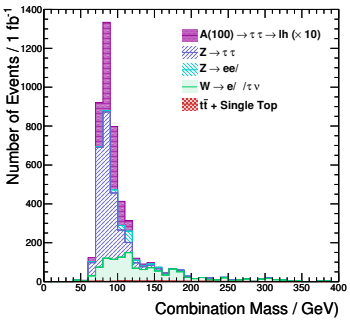

(e) Combination Mass

Figure 7.17: Using different methods to reconstruct the Higgs mass, for $M_A = 100$ GeV.

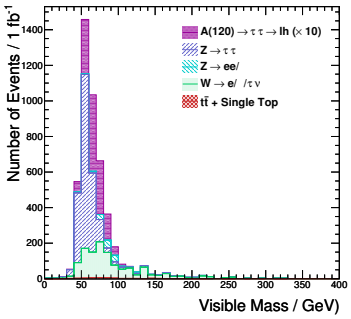

(a) Visible Mass

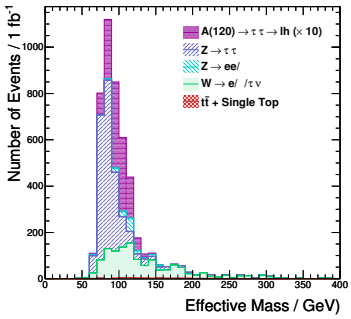

(b) Effective Mass

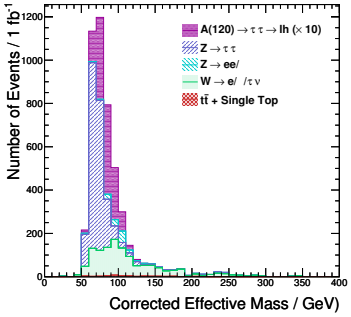

(c) Corrected Effective Mass

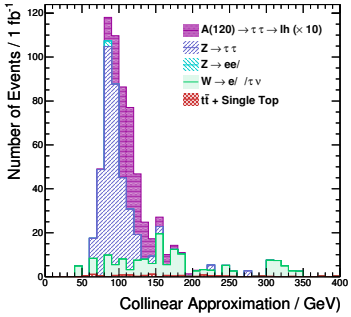

(d) Collinear Approx.

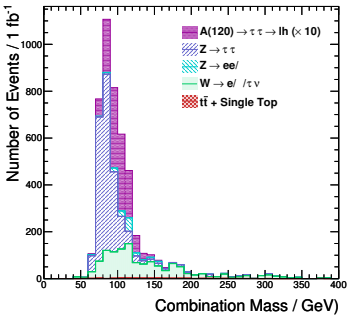

(e) Combination Mass

Figure 7.18: Using different methods to reconstruct the Higgs mass, for $M_A = 120$ GeV.

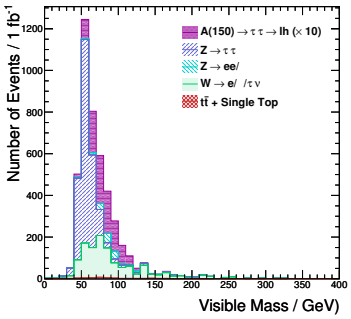

(a) Visible Mass

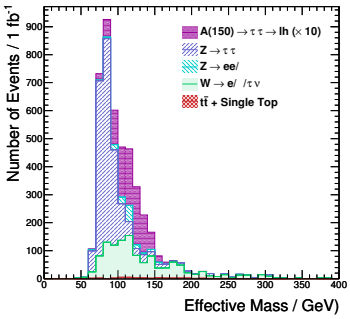

(b) Effective Mass

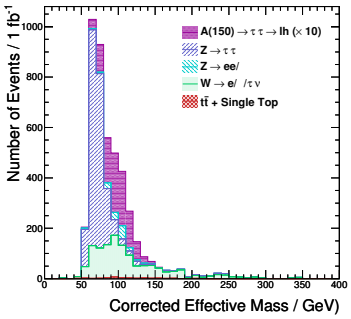

(c) Corrected Effective Mass

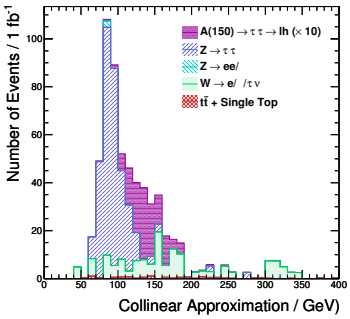

(d) Collinear Approx.

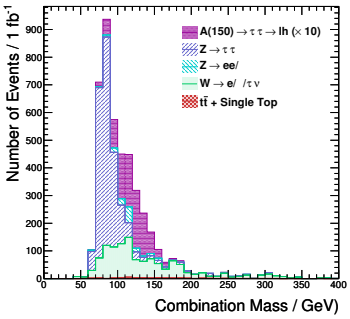

(e) Combination Mass

Figure 7.19: Using different methods to reconstruct the Higgs mass, for $M_A = 150$ GeV.

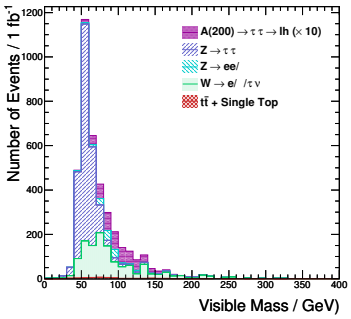

(a) Visible Mass

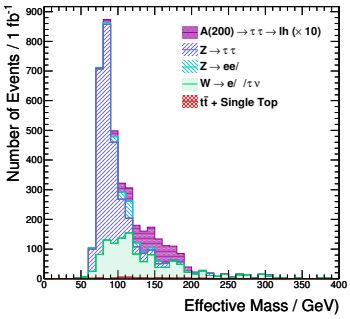

(b) Effective Mass

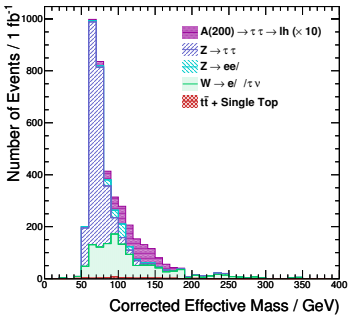

(c) Corrected Effective Mass

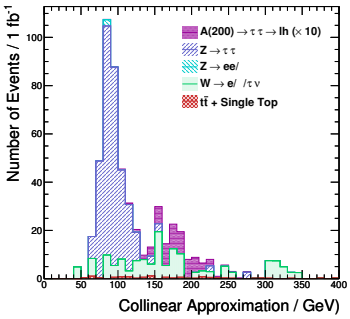

(d) Collinear Approx.

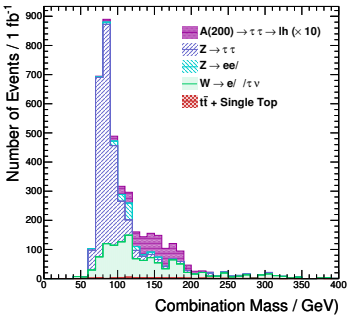

(e) Combination Mass

Figure 7.20: Using different methods to reconstruct the Higgs mass, for $M_A = 200$ GeV.

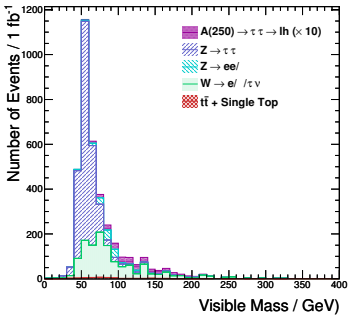

(a) Visible Mass

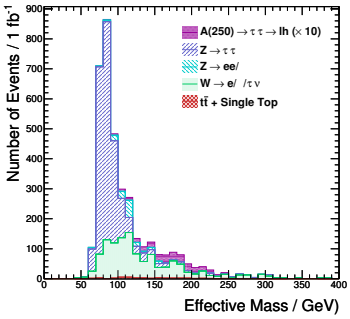

(b) Effective Mass

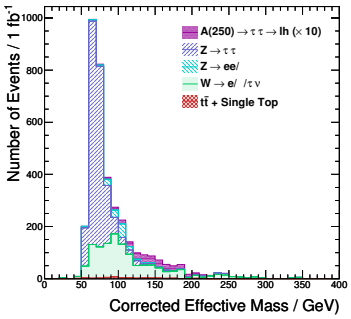

(c) Corrected Effective Mass

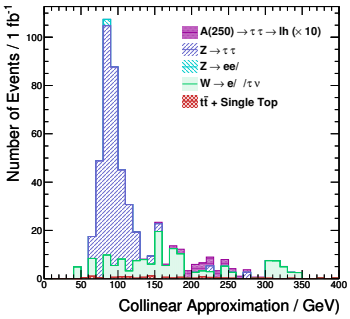

(d) Collinear Approx.

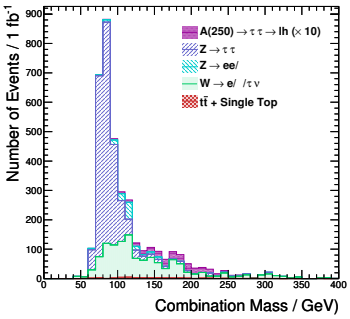

(e) Combination Mass

Figure 7.21: Using different methods to reconstruct the Higgs mass, for $M_A = 250$ GeV.

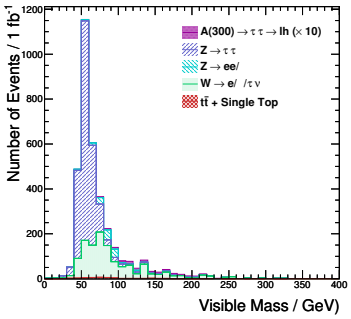

(a) Visible Mass

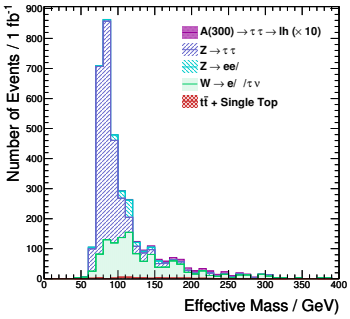

(b) Effective Mass

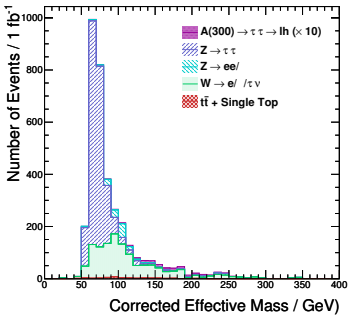

(c) Corrected Effective Mass

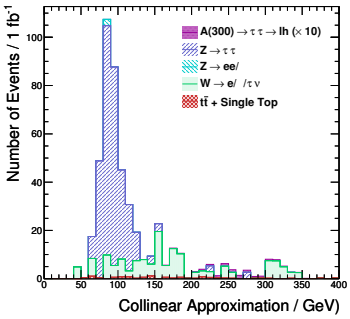

(d) Collinear Approx.

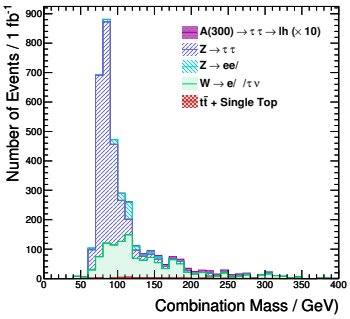

(e) Combination Mass

Figure 7.22: Using different methods to reconstruct the Higgs mass, for $M_A = 300$ GeV.

M_A (GeV)	Visible	Effective	Corr. Eff.	Collinear	Combination
90	2.08	2.08	2.10	1.21	2.11
100	2.33	2.34	2.36	0.84	2.34
110	2.65	2.71	2.77	1.19	2.73
120	2.55	2.72	2.74	1.32	2.82
130	2.66	2.88	2.79	1.41	2.97
140	2.71	2.95	2.89	1.43	3.05
150	2.43	2.66	2.61	1.25	2.75
170	2.13	2.35	2.25	1.06	2.55
200	1.59	1.75	1.74	0.84	1.81
250	0.87	0.95	0.97	0.50	0.96
300	0.43	0.50	0.46	0.24	0.53

Table 7.4: Final $S/\sqrt{B}$ achieved when using each of the different mass reconstruction methods, with 1 fb^{-1} data.

7.8.3 Choice of Mass Reconstruction Method

From table 7.4 it is immediately apparent that the collinear approximation is indeed a poor choice for this analysis across much of the mass range. However, when used in combination with the effective mass it may have some potential for use, although there is little gain in performance compared to using the effective mass alone. When assessing the analysis performance using a simple counting method as was done here (comparing the number of signal and background events in a pre-defined mass window), little difference is observed in the analysis performance by taking either the effective or corrected effective mass over the visible mass, particularly for lower M_A. It was therefore decided to use the visible mass in the analysis, since this is the simplest to understand and has no dependence on the missing E_T (and no associated systematic uncertainty).

7.9 Summary of the event selection

The final event selection is summarised below:

1. **Trigger:** Medium electron with $p_T > 10$ GeV, or muon with $p_T > 10$ GeV.

2. **Primary Vertex Requirement:** The event must have at least one vertex with three or more tracks associated to it. The vertex must be within ±150 mm of $z = 0$.

3. **Event Cleaning:** Jets are cleaned from detector effects. Any event containing a 'bad' jet with $p_T > 10$ GeV is rejected. Jets are flagged as 'bad' if they coincide with noisy cells in the hadronic endcap calorimeter, are indicative of coherent noise in the EM calorimeter, or have large out-of-time energy deposits (*e.g.* from cosmic rays).

4. **Dead Regions:** Events containing an electron candidate whose associated cluster is in a known problem region of the detector are vetoed.

5. **Lepton Selection:** The triggered lepton must have $p_T > 15$ GeV and pass the requirements described in 5.1/5.2 (electrons/muons).

6. **Di-lepton Veto:** The number of leptons in the event must be exactly equal to one.

7. **Tau ID:** Exactly one 'TauCutSafeMedium' (see section 5.3.2) tau with $p_T > 30$ GeV and opposite charge to the lepton.

8. **Charge Correlation:** The tau and the lepton must have opposite charges.

9. **Missing Transverse Energy:** At least 20 GeV of missing E_T in the event.

10. **Transverse Mass:** Transverse mass between lepton and missing $E_T < 25$ GeV.

11. **Jet Multiplicity:** $N_{jets} < 3$

12. **Mass Reconstruction:** The invariant mass of the visible tau daughters is taken.

7.10 Results

The number of expected signal and background events in 1 fb^{-1} data at the visible mass window are given in table 7.5. The results are shown separately for each jet multiplicity bin. The significances ($S/\sqrt{B}$) are also given. QCD samples were not included, due to the lack of available statistics. The final significance is calculated by summing in quadrature the significances for each jet multiplicity. Complete cut flow tables detailing the expected number of events with 1 fb^{-1} data for individual signal and background processes are given in appendix B.

7.11 Comparison with Data

Comparisons with data are made using 1.02 pb^{-1} data for the electron channel and 1.15 pb^{-1} data in the muon channel. Several changes are made to the analysis, either to increase the acceptance while there is a limited amount of data, or to comply with official ATLAS recommendations for running on the first data. These are summarised below.

- **Good Run List:** Luminosity blocks were required to be flagged as 'GOOD' by the electron, muon, tau and jet combined performance groups. This effectively means that the inner detector, both calorimeters and the muon chambers were working correctly and that both magnets were on and at the correct current. An overview of Data Quality Monitoring at ATLAS can be found in chapter 4.

- **Trigger:** The lowest pre-scaled triggers are chosen to maximise the acceptance. For the electron channel, a photon trigger with a minimum p_T requirement of 10 GeV is used, since this is very similar to the electron trigger, but without the tracking requirements. The muon channel uses the level 1 10 GeV muon trigger.

M_A / GeV	$S/\sqrt{B}$	N_{jets}	N_{signal}	$N_{background}$	$S/\sqrt{B}$
90	2.08	0	64.7	148	1.68
		1	23.9	521	1.05
		2	11.1	298	0.64
100	2.35	0	83.1	1720	2.01
		1	26.8	596	1.10
		2	9.22	294	0.54
110	2.67	0	91.9	1580	2.31
		1	27.2	521	1.19
		2	8.94	237	0.58
120	2.60	0	66.4	861	2.26
		1	20.8	298	1.21
		2	5.42	157	0.44
130	2.71	0	70.6	890	2.37
		1	22.3	323	1.24
		2	6.17	173	0.47
140	2.75	0	69.1	890	2.32
		1	25.0	323	1.39
		2	6.84	173	0.52
150	2.50	0	48.3	516	2.13
		1	17.7	202	1.24
		2	4.96	131	0.43
170	2.23	0	31.5	288	1.85
		1	13.4	129	1.18
		2	3.94	108	0.38
200	1.65	0	25.3	351	1.35
		1	11.7	171	0.89
		2	3.55	124	0.32
250	0.88	0	10.9	254	0.69
		1	6.50	159	0.51
		2	2.13	97.7	0.22
300	0.44	0	4.68	192	0.34
		1	2.96	133	0.26
		2	1.09	91.9	0.11

Table 7.5: Expected number of signal and background events and $S/\sqrt{B}$ in visible mass window for each jet-multiplicity bin, plus final $S/\sqrt{B}$ achieved at each mass point, with 1 fb^{-1} data.

- **Looser Cuts:** The lepton p_T cuts are lowered to 10 GeV, and the tau p_T cut is lowered to 20 GeV. The transverse mass is required to be less than 30 GeV.

- **Jet Calibration:** Jets are re-weighted to the electromagnetic scale and a jet energy scale factor which depends on the jet p_T and η is applied.

- **Missing $\mathbf{E_T}$:** The missing transverse energy is calculated using the ATLAS 'LocHadTopo' algorithm, where the $\not\!\!E_T$ is reconstructed as a vector sum over topological energy clusters. For the muon channel, the contribution from muons is also added

7.11.1 QCD Normalisation

QCD multi-jet processes are expected to provide a significant source of background to the analysis, but there are large uncertainties related to the size and effect of their contribution. The processes are generated at leading order and are therefore not expected to correctly describe the normalised cross-section. In addition, the production of leptons in QCD processes is not well understood either. A scale factor must therefore calculated to normalise the QCD to data.

Control regions where certain backgrounds will dominate can be defined, and in this way a clean sample of a given background can be obtained. Since the majority of signal and $Z \rightarrow \tau\tau$events should have opposite-sign charge (OS) between the lepton and tau, requiring that the lepton and tau have the same-sign charge (SS) should provide a sample of events mostly free of these types of events. Two separate regions can therefore be defined:

1. Opposite-sign charge between lepton and tau.

2. Same-sign charge between lepton and tau.

Tables 7.6 and 7.7 give the expected number of signal and background events and observed number of data events in the different regions, after the tau ID cut.

Sample	Opposite-Sign	Same-Sign
Data	861	828
$A(100) \to \tau\tau$	0.504 $\pm$0.008	0.013 $\pm$0.001
$A(150) \to \tau\tau$	0.174 $\pm$0.002	0.0043 $\pm$0.0003
$A(200) \to \tau\tau$	0.0672 $\pm$0.0008	0.0019 $\pm$0.0001
$A(300) \to \tau\tau$	0.0116 $\pm$0.0001	3.1×10^{-4} $\pm 2\times10^{-5}$
$W \to e\mu\tau + \nu$	33.6 $\pm$0.4	16.0 $\pm$0.3
$Z \to ll$	9.2 $\pm$0.2	2.52 $\pm$0.08
$Z \to \tau\tau$	11.7 $\pm$0.2	0.70 $\pm$0.04
$t\bar{t}$	1.34 $\pm$0.01	0.524 $\pm$0.007
Single Top	0.28 $\pm$0.02	0.14 $\pm$0.01
QCD	2541 $\pm$147	2233 $\pm$138
Total Non-QCD Backgrounds	56.1 $\pm$0.5	19.9 $\pm$0.3

Table 7.6: Electron channel: Expected number of signal and background events in same-sign and opposite-sign regions with 1.02 pb^{-1} data.

From these, we can see that the same-sign region is predominantly composed of QCD backgrounds, with negligible contribution from signal events. Filters for single leptons were applied to the QCD di-jet samples at generator level. The single muon filter sample was generated with the transverse momentum of the two partons involved in the hard scatter ($\hat{p_T}$) required to be at least 8 GeV, with no upper limit. For the equivalent sample filtered for electrons, simulations are only available in the range 17 GeV $\leq$ $\hat{p_T}$ $\leq$ 140 GeV. A QCD di-jet sample filtered to be very electromagnetic at generator level (*i.e.* contain many objects which can fake electrons and photons) was also included, but this does not cover the low p_T region ($\hat{p_T}$ $\geq$ 17 GeV.

Although the same-sign control region is relatively pure QCD ($\sim$95%), contributions from other backgrounds should also be taken into account. A normalisation factor, to scale the QCD Monte Carlo to what should be expected in data can therefore be defined as:

$$F_{Normalisation} = \frac{N_{Data} - N_{non-QCD}}{N_{QCD}}$$

where N_{Data}, $N_{non-QCD}$ and N_{QCD} are the observed number of data events, expected number of non-QCD background events and number of QCD Monte Carlo

Sample	Opposite-Sign	Same-Sign
Data	1079	934
$A(100) \to \tau\tau$	0.67 $\pm$0.01	0.016 $\pm$0.002
$A(150) \to \tau\tau$	0.216 $\pm$0.003	0.0039 $\pm$0.0003
$A(200) \to \tau\tau$	0.0840 $\pm$0.0009	0.0015 $\pm$0.0001
$A(300) \to \tau\tau$	0.0135 $\pm$0.0002	2.5×10^{-4} $\pm 2\times10^{-5}$
$W \to e\mu\tau + \nu$	57.7 $\pm$0.6	25.3 $\pm$0.4
$Z \to ll$	6.8 $\pm$0.1	2.25 $\pm$0.08
$Z \to \tau\tau$	17.1 $\pm$0.2	0.63 $\pm$0.04
$t\bar{t}$	1.98 $\pm$0.01	0.738 $\pm$0.009
Single Top	0.36 $\pm$0.02	0.15 $\pm$0.01
QCD	2095 $\pm$56	1950 $\pm$54
Total Non-QCD Backgrounds	84.0 $\pm$0.6	29.1 $\pm$0.4

Table 7.7: Muon channel: Expected number of signal and background events in same-sign and opposite-sign regions with 1.15 pb^{-1} data.

		Data	QCD	non-QCD	$F_{Normalisation}$
Electron Channel	OS	861	2541 $\pm$147	56.1 $\pm$0.5	0.34 +/-0.02
	SS	828	2233 $\pm$138	19.9 $\pm$0.3	0.37 +/-0.02
Muon Channel	OS	1079	2095 $\pm$56	84.0 $\pm$0.6	0.52 +/-0.01
	SS	934	1950 $\pm$54	29.1 $\pm$0.4	0.48 +/-0.01

Table 7.8: Observed number of data events, and expected number of QCD and non-QCD background events in the opposite-sign and same-sign regions. The normalisation factor to be applied to the QCD Monte Carlo ($F_{Normalisation}$) is also given.

events (respectively) in the same-sign region. The number of signal events in this region is negligible, even for the highest cross-section processes, and therefore not included. The results are summarised in table 7.8. Results for the opposite-sign region are also included for completeness. A scale factor of 0.37 is applied to the QCD Monte Carlo in the electron channel, and 0.48 in the muon channel. Similar methods are used in other ATLAS analyses, for example reference [51], where similar conclusions are drawn.

The missing E_T distributions in the same-sign and opposite regions for each channel are shown in figure 7.23. Better agreement is observed in the muon

channel than the electron channel, probably due to the fact that the QCD di-jet samples filtered for muons cover the entire $\hat{p_T}$ range, whereas there are no samples available to model the low $\hat{p_T}$ region (< 17 GeV) in the electron channel. This is supported by the observation that, in the electron channel, the agreement is significantly worse at the lower end of the missing E_T spectrum than at higher missing E_T. Single electron filter samples should therefore be generated for the entire $\hat{p_T}$ range, to allow for better normalisation of the QCD Monte Carlo simulations.

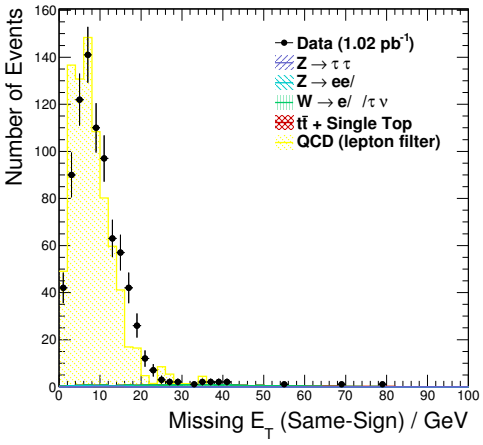

(a) Electron channel, same-sign region.

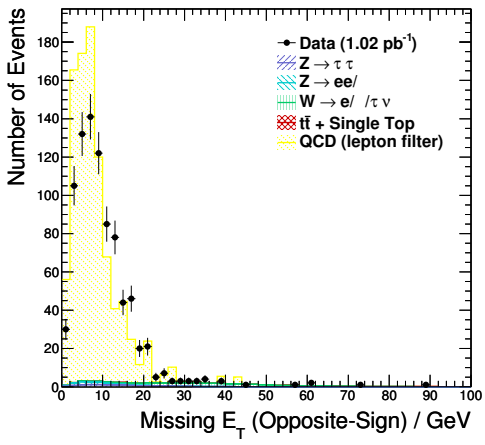

(b) Electron channel, opposite-sign region.

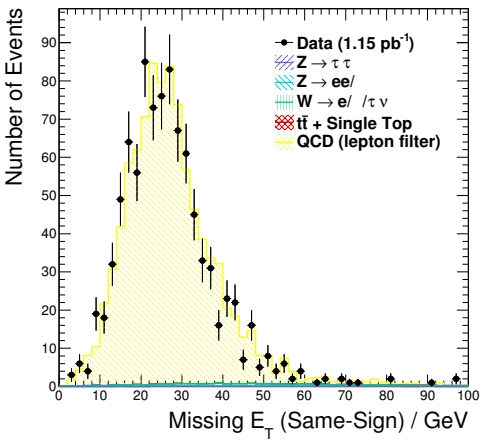

(c) Muon channel, same-sign region.

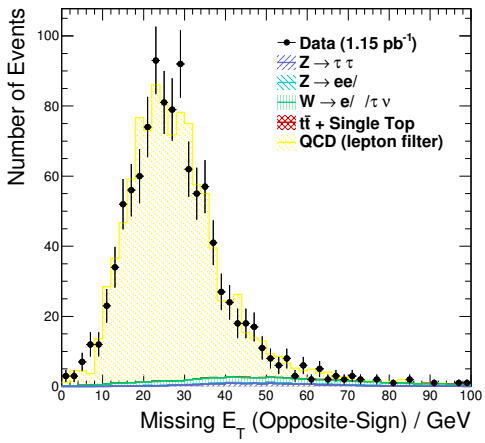

(d) Muon channel, opposite-sign region.

Figure 7.23: Missing E_T distributions for the same-sign (a, c) and opposite-sign (b, d) regions of the electron (a, b) and muon (c, d) channels.

7.11.2 Data-Monte Carlo Comparisons

Applying the normalisation factors to the simulated QCD samples, comparisons are made between the data and Monte Carlo. Results are shown in figures 7.24-7.34. Variables were plotted after the tau ID requirements had been made, but before the charge correlation cut, to be consistent with the QCD normalisation figure calculations. The statistics are therefore limited, particularly for the QCD simulations, where single events can have a very large weight due to the large cross-section of the process. As a result, it is difficult to say at this stage whether any observed discrepancies are real effects, or are simply due to a lack of statistics.

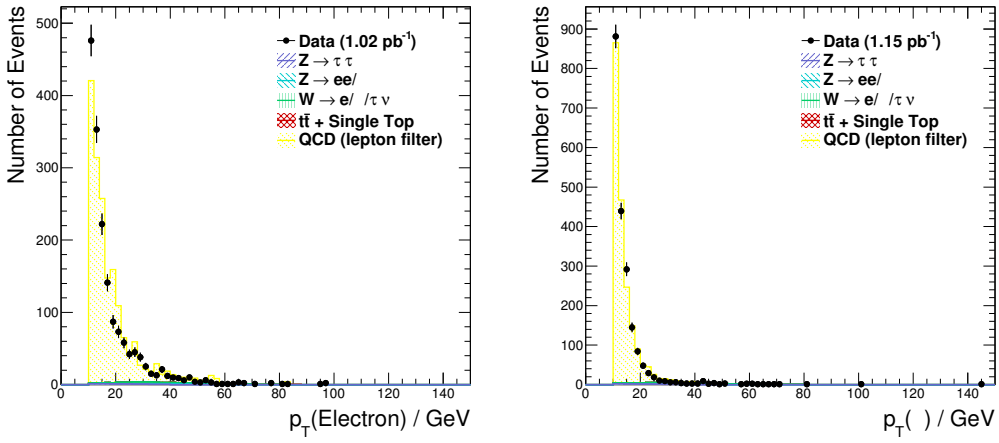

(a) Electron p_T (b) Muon p_T

Figure 7.24: Lepton p_T distributions.

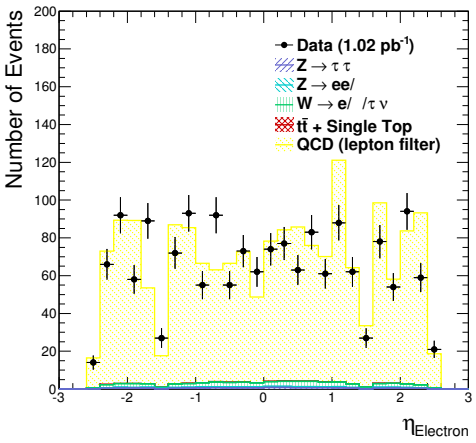

(a) Electron η

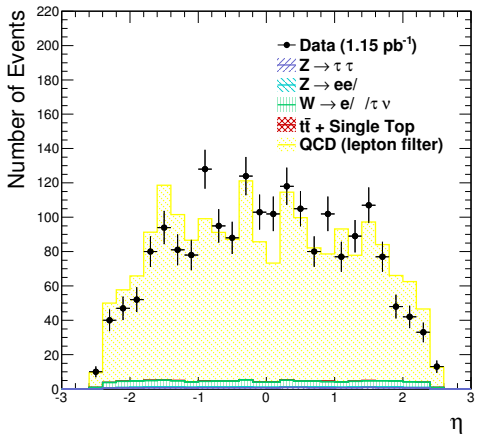

(b) Muon η

Figure 7.25: Lepton η distributions.

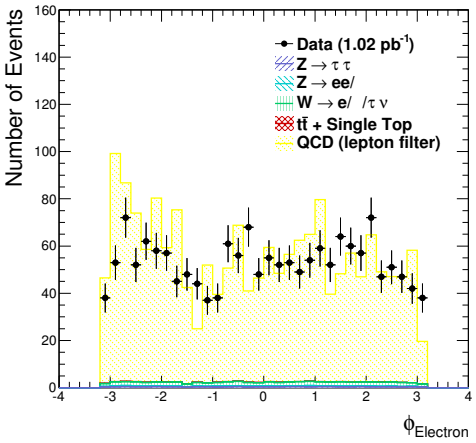

(a) Electron ϕ

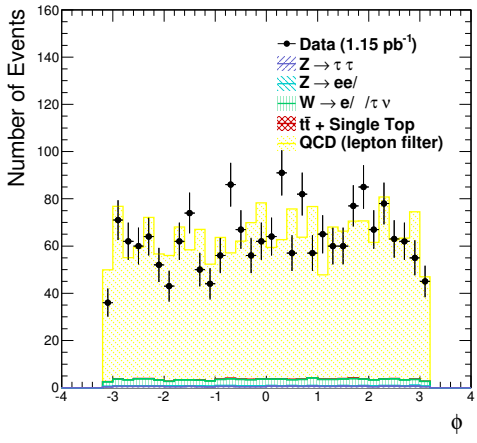

(b) Muon ϕ

Figure 7.26: Lepton ϕ distributions.

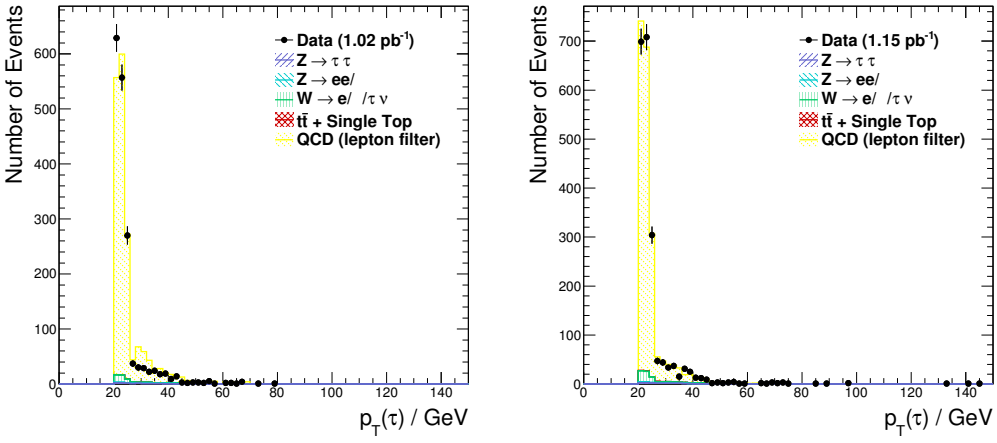

(a) Electron Channel (b) Muon Channel

Figure 7.27: Tau p_T distributions.

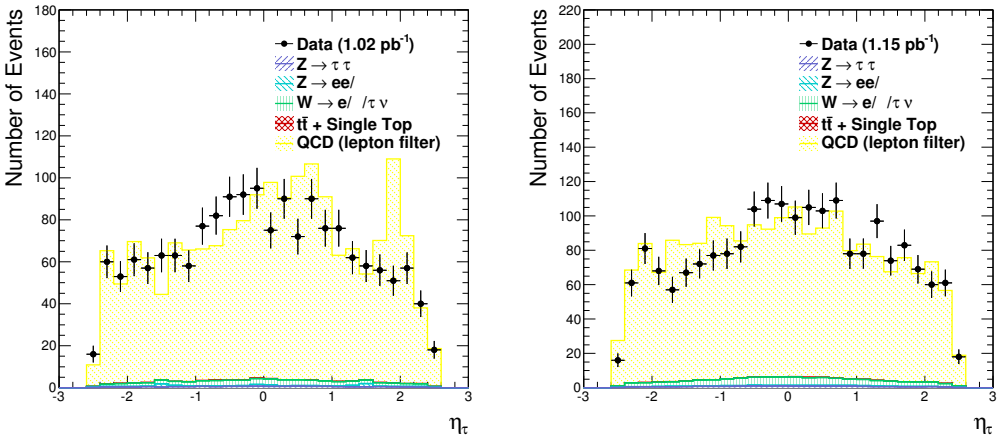

(a) Electron Channel (b) Muon Channel

Figure 7.28: Tau η distributions.

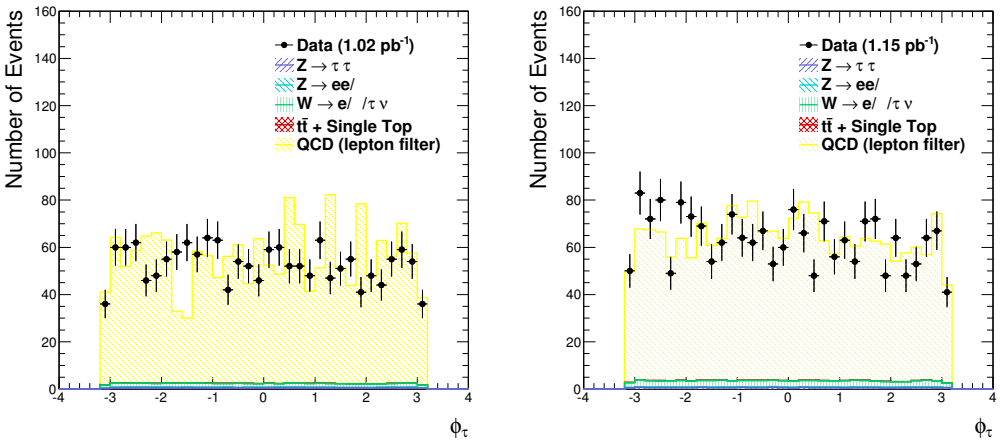

(a) Electron Channel (b) Muon Channel

Figure 7.29: Tau ϕ distributions.

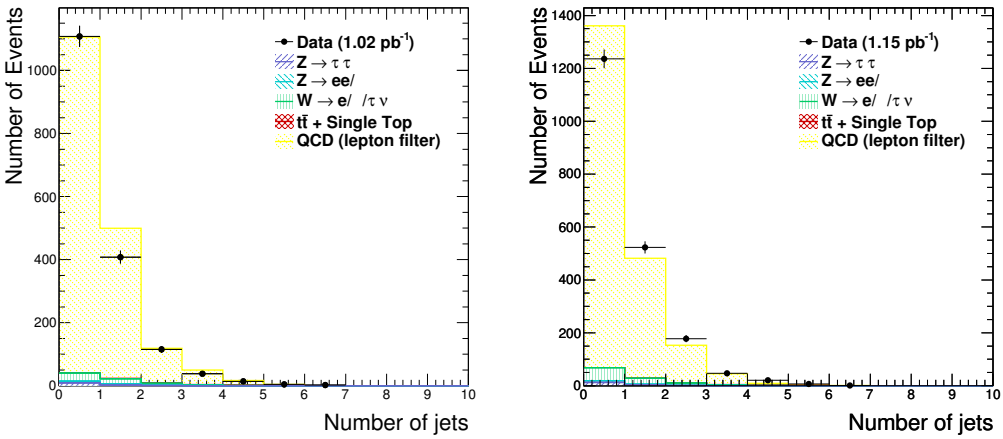

(a) Electron Channel (b) Muon Channel

Figure 7.30: Jet multiplicity

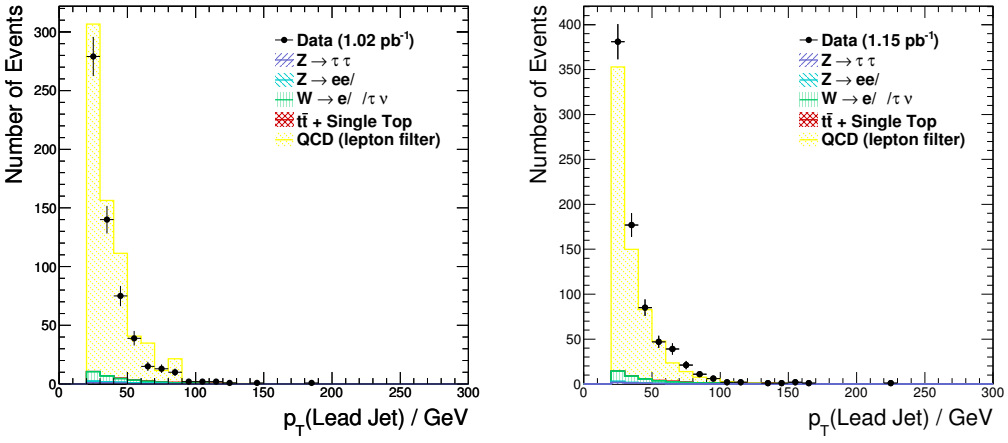

(a) Electron Channel (b) Muon Channel

Figure 7.31: Lead jet p_T distributions.

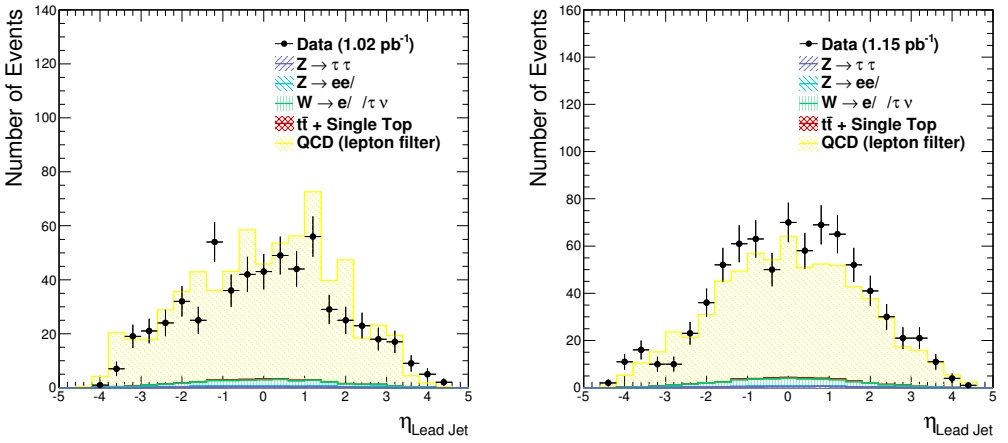

(a) Electron Channel (b) Muon Channel

Figure 7.32: Lead jet η distributions.

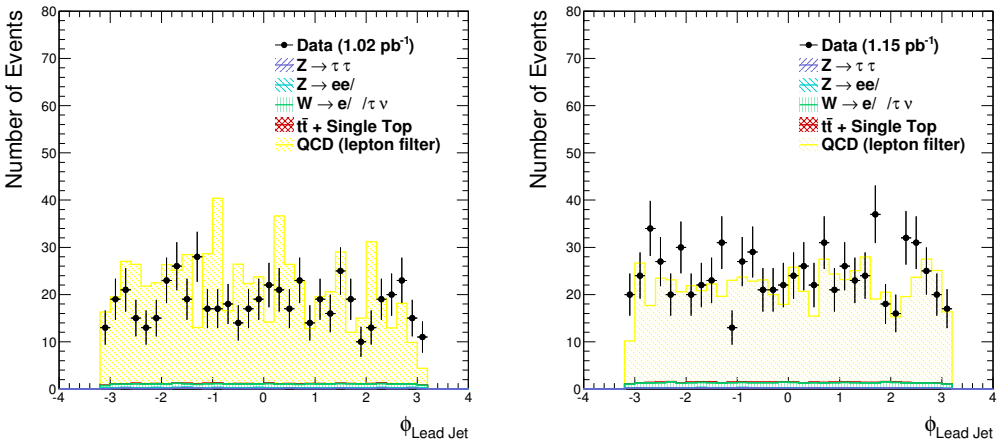

(a) Electron Channel (b) Muon Channel

Figure 7.33: Lead jet ϕ distributions.

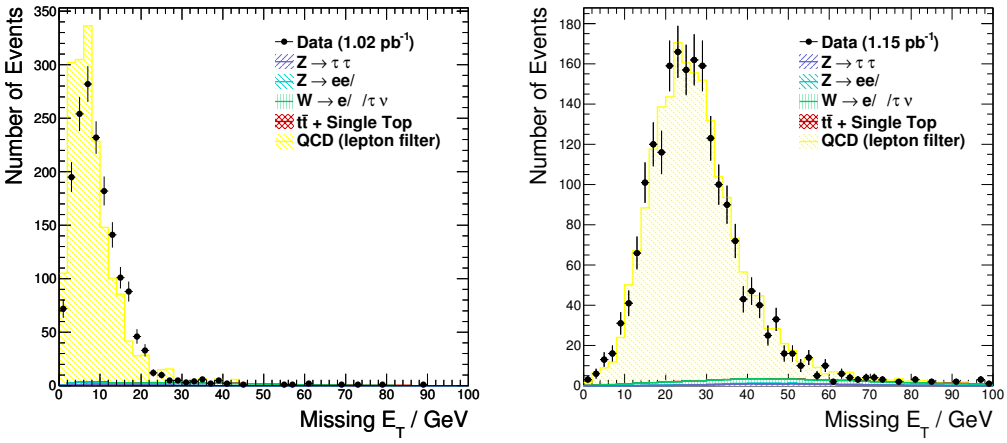

(a) Electron Channel (b) Muon Channel

Figure 7.34: Missing transverse energy distributions.

7.12 Summary and Outlook

Methods have been developed to optimise the discovery/exclusion potential for an MSSM Higgs boson. Focus has been maintained on ensuring that the analysis is 'robust' during the 2010-2011 LHC run. The use of variables which are unlikely to be well understood during the early data-taking period have therefore been avoided. Angular correlations between the signal and W and top backgrounds have been exploited with great success to provide excellent discrimination and boost the signal sensitivity. It is desirable to obtain estimates of background contributions from data wherever possible, rather than relying entirely on Monte Carlo simulations. The potential of these angular correlation variables for use in extracting a clean sample of a given background from data should be exploited.

The cuts applied to select the signal are very effective at suppressing the QCD backgrounds, with the result that there are too few events left to estimate its overall contribution. Low statistics, coupled with a large cross-section gives rise to strange structures in distributions and can provide mis-leading results. For this reason, QCD backgrounds were not considered when optimising the angular correlation cuts, mass windows or when presenting the final significances and number of events. It will be essential to obtain an estimate of the QCD background from data. Since more than 99% of signal events will have opposite-sign tau daughters, but QCD will have a 50:50 split between opposite-sign and same-sign events, a clean sample of QCD events can be obtained by requiring only same-sign type events. A cut on the transverse mass can then be made to reject any W-events. This sample can then be used to determine the QCD distributions of variables used in the analysis and make an estimate of the overall contribution. A full description of the method can be found in reference [52].

The presence of b-jets in the signal can be exploited to further improve the analysis performance. Since the cases where there are no jets present, and where there are jets but none of them are identified as b-jets (either because no b-jets are

present, or because they have been missed) must also be considered, the signal events can be divided into three categories:

1. There are no jets in the event
2. There is no b-jet present in the event, or the b-jet has not been reconstructed.
3. One or more b-jets are found.

Using this method, the analysis can be optimised separately for each different final state, for example by using harsher cuts on the transverse mass in the '0-jet' and '0-b-jet' analyses to better reject W-backgrounds. This has not been implemented at this time due to the large uncertainty in the distribution of b-tagging weights in QCD, which should be extracted from data using the method described above.

Systematic uncertainties must also be taken into account when the full analysis is performed. At the time of writing, the main sources of systematic uncertainty and their contributions are expected to be uncertainties related to the luminosity measurement (11%), and uncertainties on the electron, muon, tau and jet energy scales (8%, 7%, 10% and 1-21% respectively) [52].

Chapter 8

Summary & Outlook

Indirect evidence indicates that the Standard Model, if it holds true, favours a low mass Higgs boson of approximately 120 GeV. In this region the VBF $H \rightarrow \tau\tau$ search mode will be of particular importance. The decay is also one of only two possible decays which can access the fermion couplings of the Higgs boson. Techniques to improve the analysis performance have been presented, together with methods to estimate background contributions and reject contributions from the $t\bar{t}$ process - one of the dominant backgrounds to the analysis.

For extensions to the Standard Model that realise supersymmetry, such as the MSSM, decays to third generation fermions are enhanced for much of the phase space and the di-tau search channel is important across the entire mass range. The cross-section for MSSM Higgs boson production is large enough that competitive limits should be able to be placed on the MSSM phase space using data from the 2010-2011 LHC run (1 fb^{-1} expected with 7 TeV centre-of-mass collisions). A search strategy has been presented to optimise acceptance in the $A \rightarrow \tau\tau \rightarrow lh$ channel, ensuring that the analysis will be robust during the early data-taking period and using only variables which can be fully understood and validated during this period.

Comparisons with approximately 1 pb^{-1} data have been made and show reasonable agreement with the Monte Carlo, although further effort is needed to

better normalise the QCD Monte Carlo samples to data. Lack of available statistics for QCD has been one of the main problems in this analysis, but with around 10 pb^{-1} data, there should be enough events to define a control region to obtain an estimate of the QCD contribution directly from data. The LHC continues to deliver proton-proton collisions to ATLAS (and the other LHC experiments) and at the time of writing has delivered a total of 3.69 pb^{-1}, of which 3.46 pb^{-1} has been recorded by ATLAS (see figure 8.1).

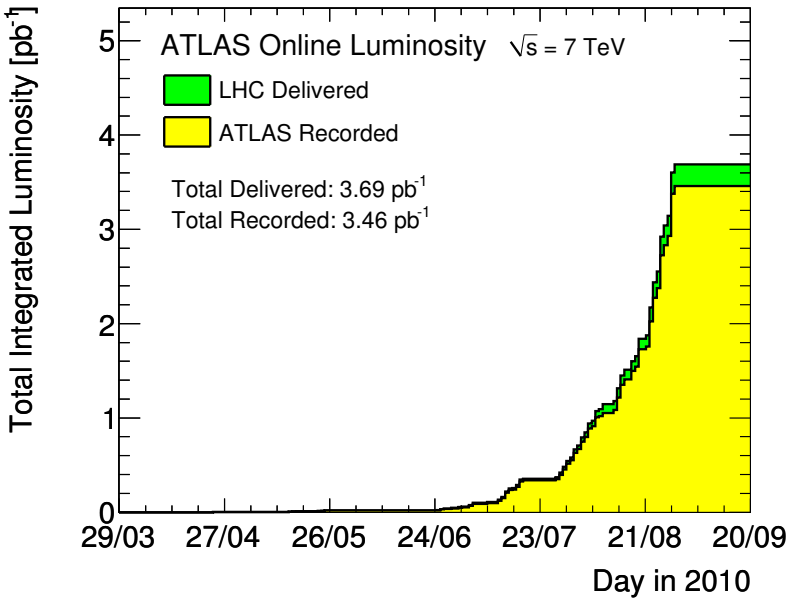

Figure 8.1: Cumulative luminosity versus day delivered to and recorded by ATLAS during stable beams at a 7 TeV centre-of-mass energy [53].

Data quality monitoring is on-going and is an essential part of the data-taking and process. The DCS Calculator is a key component of the data quality monitoring framework at ATLAS and its output is crucial when deciding the overall data-quality status for any given run or luminosity block. It has been running fully automatically since the first LHC switch-on in September 2008 and is used by almost all sub-detector systems.

Reliable data quality monitoring is essential for all analyses, to prevent misinterpretation of results. Because of the complexity of di-tau analyses, such as

those presented in this thesis, practically all sub-detectors are required to be well understood and providing good quality data. With this in place, taus will then become a valid probe for new physics at ATLAS.

Appendix A

Collinear Approximation

The invariant mass of the di-tau pair cannot be reconstructed directly due to the prescence of neutrinos in the tau decay. However, if the assumption is made that the tau decay products are collinear with the parent tau in the laboratory frame. This is a good approximation since $m_H/2 \gg m_\tau$ and the taus are therefore highly boosted.

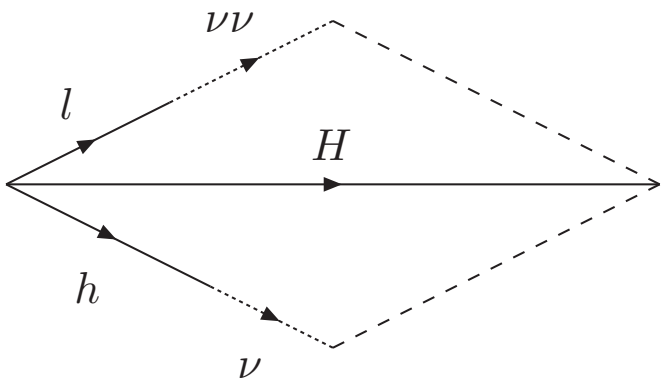

Figure A.1:

The invariant mass of the di-tau pair is defined as:

$$m_{\tau\tau} = \sqrt{2E_{\tau_l}E_{\tau_h}(1 - cos\theta_{lh})} \tag{A.1}$$

Since $E_{\tau_l} = E_l + E_{\nu_l}$ and $E_{\tau_h} = E_h + E_{\nu_h}$, this can be re-written as:

$$m_{\tau\tau} = \sqrt{2(E_l + E_{\nu_l})(E_h + E_{\nu_h})(1 - cos\theta_{lh})} \tag{A.2}$$

The $E_{\nu_{l,h}}$ terms are unknown, but can be expressed in terms of the fraction of the parent tau's momentum carried by the visible daughter, $x_{l,h}$, where

$$\begin{aligned} x_l &= \frac{E_l}{E_l + E_{\nu_l}} \\ &= \frac{E_x(h)E_y(l) - E_y(h)E_x(l)}{E_x(h)E_y(l) - E_x(miss)E_y(h) - E_y(h)E_x(l) + E_y(miss)E_x(h)} \end{aligned} \tag{A.3}$$

and

$$\begin{aligned} x_h &= \frac{E_h}{E_h + E_{\nu_h}} \\ &= \frac{E_x(h)E_y(l) - E_y(h)E_x(l)}{E_x(h)E_y(l) + E_x(miss)E_y(l) - E_y(h)E_x(l) - E_y(miss)E_x(l)} \end{aligned} \tag{A.4}$$

Re-arranging for $E_{\nu_{l,h}}$ and substituting into equation A.2 gives:

$$m_{\tau\tau} = \sqrt{2\left(E_l + \frac{E_l(1-x_l)}{x_l}\right)\left(E_h + \frac{E_h(1-x_h)}{x_h}\right)(1 - cos\theta_{lh})} \tag{A.5}$$

Which then solves to:

$$m_{\tau\tau} = \frac{\sqrt{2E_lE_h(1 - cos\theta_{lh})}}{\sqrt{x_lx_h}} \tag{A.6}$$

And we arrrive finally at:

$$m_{\tau\tau} = \frac{m_{lh}}{\sqrt{x_lx_h}} \tag{A.7}$$

If the two taus are back-to back then x_l and x_h cannot be resolved because the two equations become linearly dependent. For this reason, events with back-to-back tau pairs are excluded. Events that come from the process $X \to \tau\tau$ with no other physical sources of missing E_T should have $0 < x_l, x_h < 1$, though missing E_T resolution effects can can lead to unphysical solutions outside these bounds [9].

Appendix B

MSSM Analysis Cut Flow Tables

	$ggA(90) \to \tau\tau$			$bbA(90) \to \tau\tau$			$Z \to \tau\tau$		
Start	1.06e+04 ± 4.35e+01			7790 ± 35			1.03e+06 ± 8.36e+05		
Trigger	3740 ± 26			3149 ± 22			2.10e+05 ± 1.62e+05		
Vertex Requirement	3698 ± 26			3117 ± 22			2.07e+05 ± 1.60e+05		
Event Cleaning	3695 ± 26			3114 ± 22			2.07e+05 ± 1.60e+05		
Dead Regions	3580 ± 25			3021 ± 22			2.02e+05 ± 1.56e+05		
Lepton p_T	2194 ± 20			1811 ± 17			1.10e+05 ± 8.17e+04		
$Di-lepton\ Veto$	1900 ± 18			1786 ± 17			9.85e+04 ± 7.34e+04		
Tau ID	231 ± 6			246 ± 6			8556 ± 6243		
Charge Correlation	225 ± 6			244 ± 6			8306 ± 6152		
Missing p_T	69.4 ± 3.5			56.2 ± 3.0			2463 ± 1564		
Transverse Mass	61.1 ± 3.3			51.5 ± 2.8			2191 ± 1489		
	$0-jet$	$1-jet$	$2-jet$	$0-jet$	$1-jet$	$2-jet$	$0-jet$	$1-jet$	$2-jet$
N_{Jets}	32.3 ± 2.4	15.8 ± 1.7	8.87 ± 1.26	36.7 ± 2.4	9.98 ± 1.25	3.28 ± 0.71	1366 ± 60	464 ± 38	258 ± 26
Visible Mass	30.7 ± 2.3	14.7 ± 1.6	7.99 ± 1.19	34.0 ± 2.3	9.20 ± 1.20	3.12 ± 0.70	1214 ± 57	402 ± 35	235 ± 25

Table 1: Number of events in 1 fb^{-1} data for signal and $Z \to \tau\tau$ background to MSSM $h/A/H(90\ GeV) \to \tau\tau \to lh$ analysis.

	$Z \to ll$			$W \to e/\mu/\tau\nu$		
Start	2.07e+06 ± 1.15e+06			3.18e+07 ± 1.37e+07		
Trigger	1.66e+06 ± 9.14e+05			1.39e+07 ± 6.66e+06		
Vertex Requirement	1.64e+06 ± 9.02e+05			1.37e+07 ± 6.56e+06		
Event Cleaning	1.64e+06 ± 9.01e+05			1.37e+07 ± 6.56e+06		
Dead Regions	1.57e+06 ± 8.66e+05			1.33e+07 ± 6.35e+06		
Lepton p_T	1.31e+06 ± 7.17e+05			1.07e+07 ± 5.33e+06		
$Di-lepton\ Veto$	6.37e+05 ± 3.46e+05			1.07e+07 ± 5.32e+06		
Tau ID	7883 ± 3792			4.86e+04 ± 1.86e+04		
Charge Correlation	6670 ± 3496			3.66e+04 ± 1.41e+04		
Missing p_T	682 ± 243			3.12e+04 ± 1.21e+04		
Transverse Mass	155 ± 71			2025 ± 672		
	$0-jet$	$1-jet$	$2-jet$	$0-jet$	$1-jet$	$2-jet$
N_{Jets}	105 ± 17	23.0 ± 7.7	17.7 ± 6.7	659 ± 61	345 ± 32	187 ± 21
Visible Mass	7.69 ± 4.44	7.66 ± 4.42	5.07 ± 3.58	257 ± 39	108 ± 18	46.3 ± 10.6

Table 2: Number of events in 1 fb^{-1} data for $Z \to ll$ and $W \to e/\mu/\tau\nu$ backgrounds to MSSM $h/A/H(90\ GeV) \to \tau\tau \to lh$ analysis.

	$t\bar{t}$			*Single Top* (Wt)			*Single Top* ($s+t-channels$)		
Start	8.74e+04 ± 8.74e+01			1.46e+04 ± 1.19e+02			2.29e+04 ± 1.25e+02		
Trigger	5.75e+04 ± 7.09e+01			5921 ± 76			1.31e+04 ± 9.52e+01		
Vertex Requirement	5.69e+04 ± 7.05e+01			5846 ± 75			1.29e+04 ± 9.47e+01		
Event Cleaning	5.69e+04 ± 7.05e+01			5842 ± 75			1.29e+04 ± 9.47e+01		
Dead Regions	5.49e+04 ± 6.93e+01			5651 ± 74			1.25e+04 ± 9.31e+01		
Lepton p_T	4.31e+04 ± 6.14e+01			4059 ± 63			9845 ± 83		
$Di-lepton\ Veto$	3.76e+04 ± 5.73e+01			3519 ± 58			9749 ± 82		
Tau ID	1766 ± 12			190 ± 14			168 ± 11		
Charge Correlation	1430 ± 11			149 ± 12			121 ± 9		
Missing p_T	1303 ± 11			133 ± 11			109 ± 9		
Transverse Mass	134 ± 3			10.7 ± 3.2			9.44 ± 2.58		
	$0-jet$	$1-jet$	$2-jet$	$0-jet$	$1-jet$	$2-jet$	$0-jet$	$1-jet$	$2-jet$
N_{Jets}	0.17 ± 0.12	5.60 ± 0.70	28.8 ± 1.6	0.0 ± 0.0	0.97 ± 0.97	3.89 ± 1.94	0.72 ± 0.72	5.72 ± 2.02	2.91 ± 1.43
Visible Mass	0.09 ± 0.09	1.22 ± 0.33	7.79 ± 0.83	0.0 ± 0.0	0.0 ± 0.0	1.94 ± 1.38	0.0 ± 0.0	2.15 ± 1.24	1.43 ± 1.01

Table 3: Number of events in 1 fb^{-1} data for $t\bar{t}$ and single top backgrounds to MSSM $h/A/H(90\ GeV) \rightarrow \tau\tau \rightarrow lh$ analysis.

	QCD			*QCD* (*single lepton filter*)		
Start	1.05e+13 ± 8.26e+09			3.06e+09 ± 2.64e+06		
Trigger	2.94e+09 ± 8.73e+07			8.24e+08 ± 1.31e+06		
Vertex Requirement	2.89e+09 ± 8.64e+07			8.14e+08 ± 1.30e+06		
Event Cleaning	2.89e+09 ± 8.64e+07			8.14e+08 ± 1.30e+06		
Dead Regions	2.84e+09 ± 8.50e+07			8.09e+08 ± 1.29e+06		
Lepton p_T	1.52e+08 ± 1.56e+07			6.02e+07 ± 3.48e+05		
$Di-lepton\ Veto$	1.51e+08 ± 1.55e+07			5.93e+07 ± 3.46e+05		
Tau ID	3.54e+05 ± 9.79e+04			1.40e+05 ± 1.04e+04		
Charge Correlation	2.23e+05 ± 7.81e+04			6.46e+04 ± 6.83e+03		
Missing p_T	1962 ± 1577			6471 ± 2315		
Transverse Mass	190 ± 109			5914 ± 2303		
	$0-jet$	$1-jet$	$2-jet$	$0-jet$	$1-jet$	$2-jet$
N_{Jets}	0.0 ± 0.0	0.03 ± 0.03	62.9 ± 62.9	4721 ± 2246	797 ± 464	132 ± 82
Visible Mass	0.0 ± 0.0	0.0 ± 0.0	0.0 ± 0.0	2575 ± 1750	558 ± 449	0.0 ± 0.0

Table 4: Number of events in 1 fb^{-1} data for QCD backgrounds to MSSM $h/A/H(90\ GeV) \rightarrow \tau\tau \rightarrow lh$ analysis.

	$ggA(100) \to \tau\tau$			$bbA(100) \to \tau\tau$			$Z \to \tau\tau$		
Start	6328 ± 32			5672 ± 25			1.03e+06 ± 8.36e+05		
Trigger	2325 ± 19			2470 ± 17			2.10e+05 ± 1.62e+05		
Vertex Requirement	2301 ± 19			2443 ± 17			2.07e+05 ± 1.60e+05		
Event Cleaning	2299 ± 19			2439 ± 17			2.07e+05 ± 1.60e+05		
Dead Regions	2224 ± 19			2365 ± 16			2.02e+05 ± 1.56e+05		
Lepton p_T	1394 ± 15			1493 ± 13			1.10e+05 ± 8.17e+04		
$Di-lepton\ Veto$	1213 ± 14			1471 ± 13			9.85e+04 ± 7.34e+04		
Tau ID	186 ± 5			259 ± 5			8556 ± 6243		
Charge Correlation	183 ± 5			256 ± 5			8306 ± 6152		
Missing p_T	59.5 ± 3.1			79.1 ± 3.0			2463 ± 1564		
Transverse Mass	53.5 ± 2.9			75.1 ± 2.9			2191 ± 1489		
	$0-jet$	$1-jet$	$2-jet$	$0-jet$	$1-jet$	$2-jet$	$0-jet$	$1-jet$	$2-jet$
N_{Jets}	30.4 ± 2.2	14.4 ± 1.5	5.38 ± 0.92	55.5 ± 2.5	13.8 ± 1.3	4.43 ± 0.71	1366 ± 60	464 ± 38	258 ± 26
Visible Mass	29.6 ± 2.2	13.3 ± 1.5	4.91 ± 0.88	53.6 ± 2.5	13.5 ± 1.2	4.31 ± 0.70	1294 ± 59	435 ± 37	209 ± 23

Table 5: Number of events in 1 fb^{-1} data for signal and $Z \to \tau\tau$ background to MSSM $h/A/H(100\ GeV) \to \tau\tau \to lh$ analysis.

	$Z \to ll$			$W \to e/\mu/\tau\nu$		
Start	2.07e+06 ± 1.15e+06			3.18e+07 ± 1.37e+07		
Trigger	1.66e+06 ± 9.14e+05			1.39e+07 ± 6.66e+06		
Vertex Requirement	1.64e+06 ± 9.02e+05			1.37e+07 ± 6.56e+06		
Event Cleaning	1.64e+06 ± 9.01e+05			1.37e+07 ± 6.56e+06		
Dead Regions	1.57e+06 ± 8.66e+05			1.33e+07 ± 6.35e+06		
Lepton p_T	1.31e+06 ± 7.17e+05			1.07e+07 ± 5.33e+06		
$Di-lepton\ Veto$	6.37e+05 ± 3.46e+05			1.07e+07 ± 5.32e+06		
Tau ID	7883 ± 3792			4.86e+04 ± 1.86e+04		
Charge Correlation	6670 ± 3496			3.66e+04 ± 1.41e+04		
Missing p_T	682 ± 243			3.12e+04 ± 1.21e+04		
Transverse Mass	155 ± 71			2025 ± 672		
	$0-jet$	$1-jet$	$2-jet$	$0-jet$	$1-jet$	$2-jet$
N_{Jets}	105 ± 17	23.0 ± 7.7	17.7 ± 6.7	659 ± 61	345 ± 32	187 ± 21
Visible Mass	31.3 ± 9.0	10.2 ± 5.1	7.61 ± 4.39	391 ± 48	146 ± 21	63.3 ± 12.4

Table 6: Number of events in 1 fb^{-1} data for $Z \to ll$ and $W \to e/\mu/\tau\nu$ backgrounds to MSSM $h/A/H(100\ GeV) \to \tau\tau \to lh$ analysis.

	$t\bar{t}$			*Single Top* (Wt)			*Single Top* ($s+t-channels$)		
Start	8.74e+04 ± 8.74e+01			1.46e+04 ± 1.19e+02			2.29e+04 ± 1.25e+02		
Trigger	5.75e+04 ± 7.09e+01			5921 ± 76			1.31e+04 ± 9.52e+01		
Vertex Requirement	5.69e+04 ± 7.05e+01			5846 ± 75			1.29e+04 ± 9.47e+01		
Event Cleaning	5.69e+04 ± 7.05e+01			5842 ± 75			1.29e+04 ± 9.47e+01		
Dead Regions	5.49e+04 ± 6.93e+01			5651 ± 74			1.25e+04 ± 9.31e+01		
Lepton p_T	4.31e+04 ± 6.14e+01			4059 ± 63			9845 ± 83		
$Di-lepton\ Veto$	3.76e+04 ± 5.73e+01			3519 ± 58			9749 ± 82		
Tau ID	1766 ± 12			190 ± 14			168 ± 11		
Charge Correlation	1430 ± 11			149 ± 12			121 ± 9		
Missing p_T	1303 ± 11			133 ± 11			109 ± 9		
Transverse Mass	134 ± 3			10.7 ± 3.2			9.44 ± 2.58		
	$0-jet$	$1-jet$	$2-jet$	$0-jet$	$1-jet$	$2-jet$	$0-jet$	$1-jet$	$2-jet$
N_{Jets}	0.17 ± 0.12	5.60 ± 0.70	28.8 ± 1.6	0.0 ± 0.0	0.97 ± 0.97	3.89 ± 1.94	0.72 ± 0.72	5.72 ± 2.02	2.91 ± 1.43
Visible Mass	0.09 ± 0.09	1.31 ± 0.34	10.8 ± 1.0	0.0 ± 0.0	0.0 ± 0.0	1.94 ± 1.38	0.72 ± 0.72	2.87 ± 1.43	1.47 ± 1.01

Table 7: Number of events in 1 fb^{-1} data for $t\bar{t}$ and single top backgrounds to MSSM $h/A/H(100\ GeV) \to \tau\tau \to lh$ analysis.

	QCD			*QCD* (*single lepton filter*)		
Start	1.05e+13 ± 8.26e+09			3.06e+09 ± 2.64e+06		
Trigger	2.94e+09 ± 8.73e+07			8.24e+08 ± 1.31e+06		
Vertex Requirement	2.89e+09 ± 8.64e+07			8.14e+08 ± 1.30e+06		
Event Cleaning	2.89e+09 ± 8.64e+07			8.14e+08 ± 1.30e+06		
Dead Regions	2.84e+09 ± 8.50e+07			8.09e+08 ± 1.29e+06		
Lepton p_T	1.52e+08 ± 1.56e+07			6.02e+07 ± 3.48e+05		
$Di-lepton\ Veto$	1.51e+08 ± 1.55e+07			5.93e+07 ± 3.46e+05		
Tau ID	3.54e+05 ± 9.79e+04			1.40e+05 ± 1.04e+04		
Charge Correlation	2.23e+05 ± 7.81e+04			6.46e+04 ± 6.83e+03		
Missing p_T	1962 ± 1577			6471 ± 2315		
Transverse Mass	190 ± 109			5914 ± 2303		
	$0-jet$	$1-jet$	$2-jet$	$0-jet$	$1-jet$	$2-jet$
N_{Jets}	0.0 ± 0.0	0.03 ± 0.03	62.9 ± 62.9	4721 ± 2246	797 ± 464	132 ± 82
Visible Mass	0.0 ± 0.0	0.0 ± 0.0	0.0 ± 0.0	2575 ± 1750	174 ± 100	7.77 ± 5.49

Table 8: Number of events in 1 fb^{-1} data for QCD backgrounds to MSSM $h/A/H(100\ GeV) \to \tau\tau \to lh$ analysis.

	$ggA(110) \to \tau\tau$			$bbA(110) \to \tau\tau$			$Z \to \tau\tau$		
Start	3974 ± 16			4217 ± 19			1.03e+06 ± 8.36e+05		
Trigger	1516 ± 10			1971 ± 13			2.10e+05 ± 1.62e+05		
Vertex Requirement	1500 ± 10			1948 ± 13			2.07e+05 ± 1.60e+05		
Event Cleaning	1498 ± 10			1945 ± 13			2.07e+05 ± 1.60e+05		
Dead Regions	1446 ± 10			1883 ± 13			2.02e+05 ± 1.56e+05		
Lepton p_T	954 ± 8			1236 ± 10			1.10e+05 ± 8.17e+04		
$Di-lepton\ Veto$	818 ± 7			1217 ± 10			9.85e+04 ± 7.34e+04		
Tau ID	152 ± 3			272 ± 5			8556 ± 6243		
Charge Correlation	150 ± 3			270 ± 5			8306 ± 6152		
Missing p_T	56.9 ± 1.9			99.3 ± 2.9			2463 ± 1564		
Transverse Mass	51.8 ± 1.9			92.5 ± 2.8			2191 ± 1489		
	$0-jet$	$1-jet$	$2-jet$	$0-jet$	$1-jet$	$2-jet$	$0-jet$	$1-jet$	$2-jet$
N_{Jets}	31.3 ± 1.4	12.7 ± 0.9	5.50 ± 0.60	68.1 ± 2.4	18.3 ± 1.2	4.81 ± 0.64	1366 ± 60	464 ± 38	258 ± 26
Visible Mass	29.2 ± 1.4	10.7 ± 0.8	4.64 ± 0.55	62.7 ± 2.3	16.4 ± 1.2	4.30 ± 0.60	1106 ± 54	340 ± 32	126 ± 18

Table 9: Number of events in 1 fb^{-1} data for signal and $Z \to \tau\tau$ background to MSSM $h/A/H(110\ GeV) \to \tau\tau \to lh$ analysis.

	$Z \to ll$			$W \to e/\mu/\tau\nu$		
Start	2.07e+06 ± 1.15e+06			3.18e+07 ± 1.37e+07		
Trigger	1.66e+06 ± 9.14e+05			1.39e+07 ± 6.66e+06		
Vertex Requirement	1.64e+06 ± 9.02e+05			1.37e+07 ± 6.56e+06		
Event Cleaning	1.64e+06 ± 9.01e+05			1.37e+07 ± 6.56e+06		
Dead Regions	1.57e+06 ± 8.66e+05			1.33e+07 ± 6.35e+06		
Lepton p_T	1.31e+06 ± 7.17e+05			1.07e+07 ± 5.33e+06		
$Di-lepton\ Veto$	6.37e+05 ± 3.46e+05			1.07e+07 ± 5.32e+06		
Tau ID	7883 ± 3792			4.86e+04 ± 1.86e+04		
Charge Correlation	6670 ± 3496			3.66e+04 ± 1.41e+04		
Missing p_T	682 ± 243			3.12e+04 ± 1.21e+04		
Transverse Mass	155 ± 71			2025 ± 672		
	$0-jet$	$1-jet$	$2-jet$	$0-jet$	$1-jet$	$2-jet$
N_{Jets}	105 ± 17	23.0 ± 7.7	17.7 ± 6.7	659 ± 61	345 ± 32	187 ± 21
Visible Mass	57.9 ± 12.3	17.9 ± 6.8	12.7 ± 5.7	414 ± 49	158 ± 22	82.8 ± 14.2

Table 10: Number of events in 1 fb^{-1} data for $Z \to ll$ and $W \to e/\mu/\tau\nu$ backgrounds to MSSM $h/A/H(110\ GeV) \to \tau\tau \to lh$ analysis.

	$t\bar{t}$			*Single Top* (Wt)			*Single Top* ($s+t-channels$)		
Start	8.74e+04 ± 8.74e+01			1.46e+04 ± 1.19e+02			2.29e+04 ± 1.25e+02		
Trigger	5.75e+04 ± 7.09e+01			5921 ± 76			1.31e+04 ± 9.52e+01		
Vertex Requirement	5.69e+04 ± 7.05e+01			5846 ± 75			1.29e+04 ± 9.47e+01		
Event Cleaning	5.69e+04 ± 7.05e+01			5842 ± 75			1.29e+04 ± 9.47e+01		
Dead Regions	5.49e+04 ± 6.93e+01			5651 ± 74			1.25e+04 ± 9.31e+01		
Lepton p_T	4.31e+04 ± 6.14e+01			4059 ± 63			9845 ± 83		
$Di-lepton\ Veto$	3.76e+04 ± 5.73e+01			3519 ± 58			9749 ± 82		
Tau ID	1766 ± 12			190 ± 14			168 ± 11		
Charge Correlation	1430 ± 11			149 ± 12			121 ± 9		
Missing p_T	1303 ± 11			133 ± 11			109 ± 9		
Transverse Mass	134 ± 3			10.7 ± 3.2			9.44 ± 2.58		
	$0-jet$	$1-jet$	$2-jet$	$0-jet$	$1-jet$	$2-jet$	$0-jet$	$1-jet$	$2-jet$
N_{Jets}	0.17 ± 0.12	5.60 ± 0.70	28.8 ± 1.6	0.0 ± 0.0	0.97 ± 0.97	3.89 ± 1.94	0.72 ± 0.72	5.72 ± 2.02	2.91 ± 1.43
Visible Mass	0.09 ± 0.09	1.57 ± 0.37	11.3 ± 1.0	0.0 ± 0.0	0.0 ± 0.0	2.92 ± 1.68	0.72 ± 0.72	2.87 ± 1.43	2.19 ± 1.24

Table 11: Number of events in 1 fb^{-1} data for $t\bar{t}$ and single top backgrounds to MSSM $h/A/H(110\ GeV) \to \tau\tau \to lh$ analysis.

	QCD			*QCD* (*single lepton filter*)		
Start	1.05e+13 ± 8.26e+09			3.06e+09 ± 2.64e+06		
Trigger	2.94e+09 ± 8.73e+07			8.24e+08 ± 1.31e+06		
Vertex Requirement	2.89e+09 ± 8.64e+07			8.14e+08 ± 1.30e+06		
Event Cleaning	2.89e+09 ± 8.64e+07			8.14e+08 ± 1.30e+06		
Dead Regions	2.84e+09 ± 8.50e+07			8.09e+08 ± 1.29e+06		
Lepton p_T	1.52e+08 ± 1.56e+07			6.02e+07 ± 3.48e+05		
$Di-lepton\ Veto$	1.51e+08 ± 1.55e+07			5.93e+07 ± 3.46e+05		
Tau ID	3.54e+05 ± 9.79e+04			1.40e+05 ± 1.04e+04		
Charge Correlation	2.23e+05 ± 7.81e+04			6.46e+04 ± 6.83e+03		
Missing p_T	1962 ± 1577			6471 ± 2315		
Transverse Mass	190 ± 109			5914 ± 2303		
	$0-jet$	$1-jet$	$2-jet$	$0-jet$	$1-jet$	$2-jet$
N_{Jets}	0.0 ± 0.0	0.03 ± 0.03	62.9 ± 62.9	4721 ± 2246	797 ± 464	132 ± 82
Visible Mass	0.0 ± 0.0	0.0 ± 0.0	0.0 ± 0.0	2575 ± 1750	232 ± 116	65.6 ± 58.1

Table 12: Number of events in 1 fb^{-1} data for QCD backgrounds to MSSM $h/A/H(110\ GeV) \to \tau\tau \to lh$ analysis.

	$ggA(120) \to \tau\tau$			$bbA(120) \to \tau\tau$			$Z \to \tau\tau$		
Start	2563 ± 8			3137 ± 10			1.03e+06 ± 8.36e+05		
Trigger	1009 ± 5			1546 ± 7			2.10e+05 ± 1.62e+05		
Vertex Requirement	998 ± 5			1529 ± 7			2.07e+05 ± 1.60e+05		
Event Cleaning	997 ± 5			1527 ± 7			2.07e+05 ± 1.60e+05		
Dead Regions	964 ± 5			1478 ± 7			2.02e+05 ± 1.56e+05		
Lepton p_T	656 ± 4			1000 ± 6			1.10e+05 ± 8.17e+04		
$Di-lepton\ Veto$	560 ± 4			984 ± 6			9.85e+04 ± 7.34e+04		
Tau ID	119 ± 2			247 ± 3			8556 ± 6243		
Charge Correlation	117 ± 2			244 ± 3			8306 ± 6152		
Missing p_T	47.3 ± 1.1			97.7 ± 1.8			2463 ± 1564		
Transverse Mass	42.4 ± 1.0			90.3 ± 1.7			2191 ± 1489		
	$0-jet$	$1-jet$	$2-jet$	$0-jet$	$1-jet$	$2-jet$	$0-jet$	$1-jet$	$2-jet$
N_{Jets}	26.9 ± 0.8	10.7 ± 0.5	3.38 ± 0.29	64.6 ± 1.4	19.6 ± 0.8	5.25 ± 0.41	1366 ± 60	464 ± 38	258 ± 26
Visible Mass	19.1 ± 0.7	7.33 ± 0.43	2.08 ± 0.23	47.3 ± 1.2	13.5 ± 0.7	3.34 ± 0.33	435 ± 34	133 ± 20	45.6 ± 10.7

Table 13: Number of events in 1 fb^{-1} data for signal and $Z \to \tau\tau$ background to MSSM $h/A/H(120\ GeV) \to \tau\tau \to lh$ analysis.

	$Z \to ll$			$W \to e/\mu/\tau\nu$		
Start	2.07e+06 ± 1.15e+06			3.18e+07 ± 1.37e+07		
Trigger	1.66e+06 ± 9.14e+05			1.39e+07 ± 6.66e+06		
Vertex Requirement	1.64e+06 ± 9.02e+05			1.37e+07 ± 6.56e+06		
Event Cleaning	1.64e+06 ± 9.01e+05			1.37e+07 ± 6.56e+06		
Dead Regions	1.57e+06 ± 8.66e+05			1.33e+07 ± 6.35e+06		
Lepton p_T	1.31e+06 ± 7.17e+05			1.07e+07 ± 5.33e+06		
$Di-lepton\ Veto$	6.37e+05 ± 3.46e+05			1.07e+07 ± 5.32e+06		
Tau ID	7883 ± 3792			4.86e+04 ± 1.86e+04		
Charge Correlation	6670 ± 3496			3.66e+04 ± 1.41e+04		
Missing p_T	682 ± 243			3.12e+04 ± 1.21e+04		
Transverse Mass	155 ± 71			2025 ± 672		
	$0-jet$	$1-jet$	$2-jet$	$0-jet$	$1-jet$	$2-jet$
N_{Jets}	105 ± 17	23.0 ± 7.7	17.7 ± 6.7	659 ± 61	345 ± 32	187 ± 21
Visible Mass	87.1 ± 15.2	17.9 ± 6.8	15.2 ± 6.2	338 ± 44	143 ± 20	80.3 ± 14.0

Table 14: Number of events in 1 fb^{-1} data for $Z \to ll$ and $W \to e/\mu/\tau\nu$ backgrounds to MSSM $h/A/H(120\ GeV) \to \tau\tau \to lh$ analysis.

	$t\bar{t}$			*Single Top* (Wt)			*Single Top* ($s+t-channels$)		
Start	8.74e+04 ± 8.74e+01			1.46e+04 ± 1.19e+02			2.29e+04 ± 1.25e+02		
Trigger	5.75e+04 ± 7.09e+01			5921 ± 76			1.31e+04 ± 9.52e+01		
Vertex Requirement	5.69e+04 ± 7.05e+01			5846 ± 75			1.29e+04 ± 9.47e+01		
Event Cleaning	5.69e+04 ± 7.05e+01			5842 ± 75			1.29e+04 ± 9.47e+01		
Dead Regions	5.49e+04 ± 6.93e+01			5651 ± 74			1.25e+04 ± 9.31e+01		
Lepton p_T	4.31e+04 ± 6.14e+01			4059 ± 63			9845 ± 83		
$Di-lepton\ Veto$	3.76e+04 ± 5.73e+01			3519 ± 58			9749 ± 82		
Tau ID	1766 ± 12			190 ± 14			168 ± 11		
Charge Correlation	1430 ± 11			149 ± 12			121 ± 9		
Missing p_T	1303 ± 11			133 ± 11			109 ± 9		
Transverse Mass	134 ± 3			10.7 ± 3.2			9.44 ± 2.58		
	$0-jet$	$1-jet$	$2-jet$	$0-jet$	$1-jet$	$2-jet$	$0-jet$	$1-jet$	$2-jet$
N_{Jets}	0.17 ± 0.12	5.60 ± 0.70	28.8 ± 1.6	0.0 ± 0.0	0.97 ± 0.97	3.89 ± 1.94	0.72 ± 0.72	5.72 ± 2.02	2.91 ± 1.43
Visible Mass	0.09 ± 0.09	1.66 ± 0.38	11.2 ± 1.0	0.0 ± 0.0	0.0 ± 0.0	2.92 ± 1.68	0.72 ± 0.72	2.86 ± 1.43	1.48 ± 1.01

Table 15: Number of events in 1 fb^{-1} data for $t\bar{t}$ and single top backgrounds to MSSM $h/A/H(120\ GeV) \to \tau\tau \to lh$ analysis.

	QCD			*QCD* (*single lepton filter*)		
Start	1.05e+13 ± 8.26e+09			3.06e+09 ± 2.64e+06		
Trigger	2.94e+09 ± 8.73e+07			8.24e+08 ± 1.31e+06		
Vertex Requirement	2.89e+09 ± 8.64e+07			8.14e+08 ± 1.30e+06		
Event Cleaning	2.89e+09 ± 8.64e+07			8.14e+08 ± 1.30e+06		
Dead Regions	2.84e+09 ± 8.50e+07			8.09e+08 ± 1.29e+06		
Lepton p_T	1.52e+08 ± 1.56e+07			6.02e+07 ± 3.48e+05		
$Di-lepton\ Veto$	1.51e+08 ± 1.55e+07			5.93e+07 ± 3.46e+05		
Tau ID	3.54e+05 ± 9.79e+04			1.40e+05 ± 1.04e+04		
Charge Correlation	2.23e+05 ± 7.81e+04			6.46e+04 ± 6.83e+03		
Missing p_T	1962 ± 1577			6471 ± 2315		
Transverse Mass	190 ± 109			5914 ± 2303		
	$0-jet$	$1-jet$	$2-jet$	$0-jet$	$1-jet$	$2-jet$
N_{Jets}	0.0 ± 0.0	0.03 ± 0.03	62.9 ± 62.9	4721 ± 2246	797 ± 464	132 ± 82
Visible Mass	0.0 ± 0.0	0.0 ± 0.0	0.0 ± 0.0	3017 ± 1805	116 ± 82	65.6 ± 58.1

Table 16: Number of events in 1 fb^{-1} data for QCD backgrounds to MSSM $h/A/H(120\ GeV) \to \tau\tau \to lh$ analysis.

	$ggA(130) \to \tau\tau$			$bbA(130) \to \tau\tau$			$Z \to \tau\tau$		
Start	1652 ± 7			2438 ± 11			1.03e+06 ± 8.36e+05		
Trigger	667 ± 4			1255 ± 8			2.10e+05 ± 1.62e+05		
Vertex Requirement	659 ± 4			1241 ± 8			2.07e+05 ± 1.60e+05		
Event Cleaning	658 ± 4			1239 ± 8			2.07e+05 ± 1.60e+05		
Dead Regions	636 ± 4			1199 ± 8			2.02e+05 ± 1.56e+05		
Lepton p_T	444 ± 3			835 ± 6			1.10e+05 ± 8.17e+04		
$Di-lepton\ Veto$	376 ± 3			821 ± 6			9.85e+04 ± 7.34e+04		
Tau ID	92.2 ± 1.6			233 ± 3			8556 ± 6243		
Charge Correlation	90.4 ± 1.6			230 ± 3			8306 ± 6152		
Missing p_T	40.3 ± 1.1			100 ± 2			2463 ± 1564		
Transverse Mass	35.8 ± 1.0			91.4 ± 2.1			2191 ± 1489		
	$0-jet$	$1-jet$	$2-jet$	$0-jet$	$1-jet$	$2-jet$	$0-jet$	$1-jet$	$2-jet$
N_{Jets}	22.7 ± 0.8	9.87 ± 0.53	2.95 ± 0.29	64.7 ± 1.8	19.7 ± 1.0	4.88 ± 0.49	1366 ± 60	464 ± 38	258 ± 26
Visible Mass	18.5 ± 0.7	7.40 ± 0.46	2.41 ± 0.26	52.2 ± 1.6	14.9 ± 0.9	3.76 ± 0.43	440 ± 34	136 ± 20	47.9 ± 11.0

Table 17: Number of events in 1 fb^{-1} data for signal and $Z \to \tau\tau$ background to MSSM $h/A/H(130\ GeV) \to \tau\tau \to lh$ analysis.

	$Z \to ll$			$W \to e/\mu/\tau\nu$		
Start	2.07e+06 ± 1.15e+06			3.18e+07 ± 1.37e+07		
Trigger	1.66e+06 ± 9.14e+05			1.39e+07 ± 6.66e+06		
Vertex Requirement	1.64e+06 ± 9.02e+05			1.37e+07 ± 6.56e+06		
Event Cleaning	1.64e+06 ± 9.01e+05			1.37e+07 ± 6.56e+06		
Dead Regions	1.57e+06 ± 8.66e+05			1.33e+07 ± 6.35e+06		
Lepton p_T	1.31e+06 ± 7.17e+05			1.07e+07 ± 5.33e+06		
$Di-lepton\ Veto$	6.37e+05 ± 3.46e+05			1.07e+07 ± 5.32e+06		
Tau ID	7883 ± 3792			4.86e+04 ± 1.86e+04		
Charge Correlation	6670 ± 3496			3.66e+04 ± 1.41e+04		
Missing p_T	682 ± 243			3.12e+04 ± 1.21e+04		
Transverse Mass	155 ± 71			2025 ± 672		
	$0-jet$	$1-jet$	$2-jet$	$0-jet$	$1-jet$	$2-jet$
N_{Jets}	105 ± 17	23.0 ± 7.7	17.7 ± 6.7	659 ± 61	345 ± 32	187 ± 21
Visible Mass	92.4 ± 15.6	17.9 ± 6.8	15.2 ± 6.2	357 ± 45	165 ± 22	92.4 ± 15.0

Table 18: Number of events in 1 fb^{-1} data for $Z \to ll$ and $W \to e/\mu/\tau\nu$ backgrounds to MSSM $h/A/H(130\ GeV) \to \tau\tau \to lh$ analysis.

	$t\bar{t}$			*Single Top* (Wt)			*Single Top* ($s+t-channels$)		
Start	8.74e+04 ± 8.74e+01			1.46e+04 ± 1.19e+02			2.29e+04 ± 1.25e+02		
Trigger	5.75e+04 ± 7.09e+01			5921 ± 76			1.31e+04 ± 9.52e+01		
Vertex Requirement	5.69e+04 ± 7.05e+01			5846 ± 75			1.29e+04 ± 9.47e+01		
Event Cleaning	5.69e+04 ± 7.05e+01			5842 ± 75			1.29e+04 ± 9.47e+01		
Dead Regions	5.49e+04 ± 6.93e+01			5651 ± 74			1.25e+04 ± 9.31e+01		
Lepton p_T	4.31e+04 ± 6.14e+01			4059 ± 63			9845 ± 83		
$Di-lepton\ Veto$	3.76e+04 ± 5.73e+01			3519 ± 58			9749 ± 82		
Tau ID	1766 ± 12			190 ± 14			168 ± 11		
Charge Correlation	1430 ± 11			149 ± 12			121 ± 9		
Missing p_T	1303 ± 11			133 ± 11			109 ± 9		
Transverse Mass	134 ± 3			10.7 ± 3.2			9.44 ± 2.58		
	$0-jet$	$1-jet$	$2-jet$	$0-jet$	$1-jet$	$2-jet$	$0-jet$	$1-jet$	$2-jet$
N_{Jets}	0.17 ± 0.12	5.60 ± 0.70	28.8 ± 1.6	0.0 ± 0.0	0.97 ± 0.97	3.89 ± 1.94	0.72 ± 0.72	5.72 ± 2.02	2.91 ± 1.43
Visible Mass	0.09 ± 0.09	1.66 ± 0.38	12.9 ± 1.1	0.0 ± 0.0	0.0 ± 0.0	2.92 ± 1.68	0.72 ± 0.72	2.86 ± 1.43	1.48 ± 1.01

Table 19: Number of events in 1 fb^{-1} data for $t\bar{t}$ and single top backgrounds to MSSM $h/A/H(130\ GeV) \to \tau\tau \to lh$ analysis.

	QCD			*QCD* (*single lepton filter*)		
Start	1.05e+13 ± 8.26e+09			3.06e+09 ± 2.64e+06		
Trigger	2.94e+09 ± 8.73e+07			8.24e+08 ± 1.31e+06		
Vertex Requirement	2.89e+09 ± 8.64e+07			8.14e+08 ± 1.30e+06		
Event Cleaning	2.89e+09 ± 8.64e+07			8.14e+08 ± 1.30e+06		
Dead Regions	2.84e+09 ± 8.50e+07			8.09e+08 ± 1.29e+06		
Lepton p_T	1.52e+08 ± 1.56e+07			6.02e+07 ± 3.48e+05		
$Di-lepton\ Veto$	1.51e+08 ± 1.55e+07			5.93e+07 ± 3.46e+05		
Tau ID	3.54e+05 ± 9.79e+04			1.40e+05 ± 1.04e+04		
Charge Correlation	2.23e+05 ± 7.81e+04			6.46e+04 ± 6.83e+03		
Missing p_T	1962 ± 1577			6471 ± 2315		
Transverse Mass	190 ± 109			5914 ± 2303		
	$0-jet$	$1-jet$	$2-jet$	$0-jet$	$1-jet$	$2-jet$
N_{Jets}	0.0 ± 0.0	0.03 ± 0.03	62.9 ± 62.9	4721 ± 2246	797 ± 464	132 ± 82
Visible Mass	0.0 ± 0.0	0.0 ± 0.0	0.0 ± 0.0	3017 ± 1805	116 ± 82	65.6 ± 58.1

Table 20: Number of events in 1 fb^{-1} data for QCD backgrounds to MSSM $h/A/H(130\ GeV) \to \tau\tau \to lh$ analysis.

	$ggA(140) \to \tau\tau$			$bbA(140) \to \tau\tau$			$Z \to \tau\tau$		
Start	1157 ± 5			1894 ± 8			1.03e+06 ± 8.36e+05		
Trigger	482 ± 3			1013 ± 6			2.10e+05 ± 1.62e+05		
Vertex Requirement	476 ± 3			1002 ± 6			2.07e+05 ± 1.60e+05		
Event Cleaning	476 ± 3			1001 ± 6			2.07e+05 ± 1.60e+05		
Dead Regions	460 ± 3			967 ± 6			2.02e+05 ± 1.56e+05		
Lepton p_T	327 ± 3			689 ± 5			1.10e+05 ± 8.17e+04		
$Di-lepton\ Veto$	276 ± 2			676 ± 5			9.85e+04 ± 7.34e+04		
Tau ID	71.2 ± 1.2			210 ± 3			8556 ± 6243		
Charge Correlation	70.0 ± 1.2			208 ± 3			8306 ± 6152		
Missing p_T	35.1 ± 0.8			101 ± 2			2463 ± 1564		
Transverse Mass	31.7 ± 0.8			91.3 ± 1.9			2191 ± 1489		
	$0-jet$	$1-jet$	$2-jet$	$0-jet$	$1-jet$	$2-jet$	$0-jet$	$1-jet$	$2-jet$
N_{Jets}	19.6 ± 0.6	8.33 ± 0.40	2.85 ± 0.23	61.8 ± 1.5	21.7 ± 0.9	5.87 ± 0.47	1366 ± 60	464 ± 38	258 ± 26
Visible Mass	16.8 ± 0.6	6.90 ± 0.36	2.18 ± 0.21	52.4 ± 1.4	18.1 ± 0.8	4.66 ± 0.42	440 ± 34	136 ± 20	47.9 ± 11.0

Table 21: Number of events in 1 fb^{-1} data for signal and $Z \to \tau\tau$ background to MSSM $h/A/H(140\ GeV) \to \tau\tau \to lh$ analysis.

	$Z \to ll$			$W \to e/\mu/\tau\nu$		
Start	2.07e+06 ± 1.15e+06			3.18e+07 ± 1.37e+07		
Trigger	1.66e+06 ± 9.14e+05			1.39e+07 ± 6.66e+06		
Vertex Requirement	1.64e+06 ± 9.02e+05			1.37e+07 ± 6.56e+06		
Event Cleaning	1.64e+06 ± 9.01e+05			1.37e+07 ± 6.56e+06		
Dead Regions	1.57e+06 ± 8.66e+05			1.33e+07 ± 6.35e+06		
Lepton p_T	1.31e+06 ± 7.17e+05			1.07e+07 ± 5.33e+06		
$Di-lepton\ Veto$	6.37e+05 ± 3.46e+05			1.07e+07 ± 5.32e+06		
Tau ID	7883 ± 3792			4.86e+04 ± 1.86e+04		
Charge Correlation	6670 ± 3496			3.66e+04 ± 1.41e+04		
Missing p_T	682 ± 243			3.12e+04 ± 1.21e+04		
Transverse Mass	155 ± 71			2025 ± 672		
	$0-jet$	$1-jet$	$2-jet$	$0-jet$	$1-jet$	$2-jet$
N_{Jets}	105 ± 17	23.0 ± 7.7	17.7 ± 6.7	659 ± 61	345 ± 32	187 ± 21
Visible Mass	92.4 ± 15.6	17.9 ± 6.8	15.2 ± 6.2	357 ± 45	165 ± 22	92.4 ± 15.0

Table 22: Number of events in 1 fb^{-1} data for $Z \to ll$ and $W \to e/\mu/\tau\nu$ backgrounds to MSSM $h/A/H(140\ GeV) \to \tau\tau \to lh$ analysis.

	$t\bar{t}$			*Single Top* (Wt)			*Single Top* ($s+t-channels$)		
Start	8.74e+04 ± 8.74e+01			1.46e+04 ± 1.19e+02			2.29e+04 ± 1.25e+02		
Trigger	5.75e+04 ± 7.09e+01			5921 ± 76			1.31e+04 ± 9.52e+01		
Vertex Requirement	5.69e+04 ± 7.05e+01			5846 ± 75			1.29e+04 ± 9.47e+01		
Event Cleaning	5.69e+04 ± 7.05e+01			5842 ± 75			1.29e+04 ± 9.47e+01		
Dead Regions	5.49e+04 ± 6.93e+01			5651 ± 74			1.25e+04 ± 9.31e+01		
Lepton p_T	4.31e+04 ± 6.14e+01			4059 ± 63			9845 ± 83		
$Di-lepton\ Veto$	3.76e+04 ± 5.73e+01			3519 ± 58			9749 ± 82		
Tau ID	1766 ± 12			190 ± 14			168 ± 11		
Charge Correlation	1430 ± 11			149 ± 12			121 ± 9		
Missing p_T	1303 ± 11			133 ± 11			109 ± 9		
Transverse Mass	134 ± 3			10.7 ± 3.2			9.44 ± 2.58		
	$0-jet$	$1-jet$	$2-jet$	$0-jet$	$1-jet$	$2-jet$	$0-jet$	$1-jet$	$2-jet$
N_{Jets}	0.17 ± 0.12	5.60 ± 0.70	28.8 ± 1.6	0.0 ± 0.0	0.97 ± 0.97	3.89 ± 1.94	0.72 ± 0.72	5.72 ± 2.02	2.91 ± 1.43
Visible Mass	0.09 ± 0.09	1.66 ± 0.38	12.9 ± 1.1	0.0 ± 0.0	0.0 ± 0.0	2.92 ± 1.68	0.72 ± 0.72	2.86 ± 1.43	1.48 ± 1.01

Table 23: Number of events in 1 fb^{-1} data for $t\bar{t}$ and single top backgrounds to MSSM $h/A/H(140\ GeV) \to \tau\tau \to lh$ analysis.

	QCD			*QCD* (*single lepton filter*)		
Start	1.05e+13 ± 8.26e+09			3.06e+09 ± 2.64e+06		
Trigger	2.94e+09 ± 8.73e+07			8.24e+08 ± 1.31e+06		
Vertex Requirement	2.89e+09 ± 8.64e+07			8.14e+08 ± 1.30e+06		
Event Cleaning	2.89e+09 ± 8.64e+07			8.14e+08 ± 1.30e+06		
Dead Regions	2.84e+09 ± 8.50e+07			8.09e+08 ± 1.29e+06		
Lepton p_T	1.52e+08 ± 1.56e+07			6.02e+07 ± 3.48e+05		
$Di-lepton\ Veto$	1.51e+08 ± 1.55e+07			5.93e+07 ± 3.46e+05		
Tau ID	3.54e+05 ± 9.79e+04			1.40e+05 ± 1.04e+04		
Charge Correlation	2.23e+05 ± 7.81e+04			6.46e+04 ± 6.83e+03		
Missing p_T	1962 ± 1577			6471 ± 2315		
Transverse Mass	190 ± 109			5914 ± 2303		
	$0-jet$	$1-jet$	$2-jet$	$0-jet$	$1-jet$	$2-jet$
N_{Jets}	0.0 ± 0.0	0.03 ± 0.03	62.9 ± 62.9	4721 ± 2246	797 ± 464	132 ± 82
Visible Mass	0.0 ± 0.0	0.0 ± 0.0	0.0 ± 0.0	3017 ± 1805	116 ± 82	65.6 ± 58.1

Table 24: Number of events in 1 fb^{-1} data for QCD backgrounds to MSSM $h/A/H(140\ GeV) \to \tau\tau \to lh$ analysis.

	$ggA(150) \to \tau\tau$			$bbA(150) \to \tau\tau$			$Z \to \tau\tau$		
Start	804 ± 4			1488 ± 7			1.03e+06 ± 8.36e+05		
Trigger	339 ± 3			823 ± 5			2.10e+05 ± 1.62e+05		
Vertex Requirement	335 ± 3			813 ± 5			2.07e+05 ± 1.60e+05		
Event Cleaning	335 ± 3			812 ± 5			2.07e+05 ± 1.60e+05		
Dead Regions	323 ± 3			787 ± 5			2.02e+05 ± 1.56e+05		
Lepton p_T	232 ± 2			570 ± 4			1.10e+05 ± 8.17e+04		
$Di-lepton\ Veto$	195 ± 2			560 ± 4			9.85e+04 ± 7.34e+04		
Tau ID	55.0 ± 1.1			179 ± 2			8556 ± 6243		
Charge Correlation	53.8 ± 1.0			177 ± 2			8306 ± 6152		
Missing p_T	27.7 ± 0.7			92.4 ± 1.7			2463 ± 1564		
Transverse Mass	24.0 ± 0.7			82.1 ± 1.6			2191 ± 1489		
	$0-jet$	$1-jet$	$2-jet$	$0-jet$	$1-jet$	$2-jet$	$0-jet$	$1-jet$	$2-jet$
N_{Jets}	15.2 ± 0.6	6.00 ± 0.35	2.09 ± 0.21	53.7 ± 1.3	20.9 ± 0.8	5.54 ± 0.41	1366 ± 60	464 ± 38	258 ± 26
Visible Mass	10.1 ± 0.5	4.01 ± 0.28	1.45 ± 0.17	38.2 ± 1.1	13.7 ± 0.6	3.51 ± 0.32	125 ± 18	45.1 ± 11.7	14.8 ± 6.1

Table 25: Number of events in 1 fb^{-1} data for signal and $Z \to \tau\tau$ background to MSSM $h/A/H(150\ GeV) \to \tau\tau \to lh$ analysis.

	$Z \to ll$			$W \to e/\mu/\tau\nu$		
Start	2.07e+06 ± 1.15e+06			3.18e+07 ± 1.37e+07		
Trigger	1.66e+06 ± 9.14e+05			1.39e+07 ± 6.66e+06		
Vertex Requirement	1.64e+06 ± 9.02e+05			1.37e+07 ± 6.56e+06		
Event Cleaning	1.64e+06 ± 9.01e+05			1.37e+07 ± 6.56e+06		
Dead Regions	1.57e+06 ± 8.66e+05			1.33e+07 ± 6.35e+06		
Lepton p_T	1.31e+06 ± 7.17e+05			1.07e+07 ± 5.33e+06		
$Di-lepton\ Veto$	6.37e+05 ± 3.46e+05			1.07e+07 ± 5.32e+06		
Tau ID	7883 ± 3792			4.86e+04 ± 1.86e+04		
Charge Correlation	6670 ± 3496			3.66e+04 ± 1.41e+04		
Missing p_T	682 ± 243			3.12e+04 ± 1.21e+04		
Transverse Mass	155 ± 71			2025 ± 672		
	$0-jet$	$1-jet$	$2-jet$	$0-jet$	$1-jet$	$2-jet$
N_{Jets}	105 ± 17	23.0 ± 7.7	17.7 ± 6.7	659 ± 61	345 ± 32	187 ± 21
Visible Mass	95.1 ± 15.8	12.8 ± 5.7	10.1 ± 5.1	296 ± 41	140 ± 20	92.4 ± 15.0

Table 26: Number of events in 1 fb^{-1} data for $Z \to ll$ and $W \to e/\mu/\tau\nu$ backgrounds to MSSM $h/A/H(150\ GeV) \to \tau\tau \to lh$ analysis.

	$t\bar{t}$			*Single Top* (Wt)			*Single Top* ($s+t-channels$)		
Start	8.74e+04 ± 8.74e+01			1.46e+04 ± 1.19e+02			2.29e+04 ± 1.25e+02		
Trigger	5.75e+04 ± 7.09e+01			5921 ± 76			1.31e+04 ± 9.52e+01		
Vertex Requirement	5.69e+04 ± 7.05e+01			5846 ± 75			1.29e+04 ± 9.47e+01		
Event Cleaning	5.69e+04 ± 7.05e+01			5842 ± 75			1.29e+04 ± 9.47e+01		
Dead Regions	5.49e+04 ± 6.93e+01			5651 ± 74			1.25e+04 ± 9.31e+01		
Lepton p_T	4.31e+04 ± 6.14e+01			4059 ± 63			9845 ± 83		
$Di-lepton\ Veto$	3.76e+04 ± 5.73e+01			3519 ± 58			9749 ± 82		
Tau ID	1766 ± 12			190 ± 14			168 ± 11		
Charge Correlation	1430 ± 11			149 ± 12			121 ± 9		
Missing p_T	1303 ± 11			133 ± 11			109 ± 9		
Transverse Mass	134 ± 3			10.7 ± 3.2			9.44 ± 2.58		
	$0-jet$	$1-jet$	$2-jet$	$0-jet$	$1-jet$	$2-jet$	$0-jet$	$1-jet$	$2-jet$
N_{Jets}	0.17 ± 0.12	5.60 ± 0.70	28.8 ± 1.6	0.0 ± 0.0	0.97 ± 0.97	3.89 ± 1.94	0.72 ± 0.72	5.72 ± 2.02	2.91 ± 1.43
Visible Mass	0.09 ± 0.09	1.57 ± 0.37	11.2 ± 1.0	0.0 ± 0.0	0.0 ± 0.0	1.94 ± 1.38	0.72 ± 0.72	2.15 ± 1.24	0.76 ± 0.72

Table 27: Number of events in 1 fb^{-1} data for $t\bar{t}$ and single top backgrounds to MSSM $h/A/H(150\ GeV) \to \tau\tau \to lh$ analysis.

	QCD			*QCD* (*single lepton filter*)		
Start	1.05e+13 ± 8.26e+09			3.06e+09 ± 2.64e+06		
Trigger	2.94e+09 ± 8.73e+07			8.24e+08 ± 1.31e+06		
Vertex Requirement	2.89e+09 ± 8.64e+07			8.14e+08 ± 1.30e+06		
Event Cleaning	2.89e+09 ± 8.64e+07			8.14e+08 ± 1.30e+06		
Dead Regions	2.84e+09 ± 8.50e+07			8.09e+08 ± 1.29e+06		
Lepton p_T	1.52e+08 ± 1.56e+07			6.02e+07 ± 3.48e+05		
$Di-lepton\ Veto$	1.51e+08 ± 1.55e+07			5.93e+07 ± 3.46e+05		
Tau ID	3.54e+05 ± 9.79e+04			1.40e+05 ± 1.04e+04		
Charge Correlation	2.23e+05 ± 7.81e+04			6.46e+04 ± 6.83e+03		
Missing p_T	1962 ± 1577			6471 ± 2315		
Transverse Mass	190 ± 109			5914 ± 2303		
	$0-jet$	$1-jet$	$2-jet$	$0-jet$	$1-jet$	$2-jet$
N_{Jets}	0.0 ± 0.0	0.03 ± 0.03	62.9 ± 62.9	4721 ± 2246	797 ± 464	132 ± 82
Visible Mass	0.0 ± 0.0	0.0 ± 0.0	0.0 ± 0.0	884 ± 625	174 ± 100	65.6 ± 58.1

Table 28: Number of events in 1 fb^{-1} data for QCD backgrounds to MSSM $h/A/H(150\ GeV) \to \tau\tau \to lh$ analysis.

	$ggA(170) \to \tau\tau$			$bbA(170) \to \tau\tau$			$Z \to \tau\tau$		
Start	410 ± 2			949 ± 4			1.03e+06 ± 8.36e+05		
Trigger	181 ± 1			555 ± 3			2.10e+05 ± 1.62e+05		
Vertex Requirement	178 ± 1			549 ± 3			2.07e+05 ± 1.60e+05		
Event Cleaning	178 ± 1			548 ± 3			2.07e+05 ± 1.60e+05		
Dead Regions	172 ± 1			531 ± 3			2.02e+05 ± 1.56e+05		
Lepton p_T	126 ± 1			397 ± 3			1.10e+05 ± 8.17e+04		
$Di-lepton\ Veto$	107 ± 1			389 ± 3			9.85e+04 ± 7.34e+04		
Tau ID	33.7 ± 0.5			141 ± 2			8556 ± 6243		
Charge Correlation	33.1 ± 0.5			139 ± 2			8306 ± 6152		
Missing p_T	18.9 ± 0.4			78.9 ± 1.2			2463 ± 1564		
Transverse Mass	15.9 ± 0.3			67.8 ± 1.1			2191 ± 1489		
	$0-jet$	$1-jet$	$2-jet$	$0-jet$	$1-jet$	$2-jet$	$0-jet$	$1-jet$	$2-jet$
N_{Jets}	9.31 ± 0.25	4.54 ± 0.18	1.53 ± 0.10	42.2 ± 0.9	18.4 ± 0.6	5.18 ± 0.31	1366 ± 60	464 ± 38	258 ± 26
Visible Mass	5.61 ± 0.20	2.77 ± 0.14	0.88 ± 0.08	25.9 ± 0.7	10.7 ± 0.4	3.06 ± 0.24	46.9 ± 11.4	5.92 ± 4.21	14.8 ± 6.1

Table 29: Number of events in 1 fb^{-1} data for signal and $Z \to \tau\tau$ background to MSSM $h/A/H(170\ GeV) \to \tau\tau \to lh$ analysis.

	$Z \to ll$			$W \to e/\mu/\tau\nu$		
Start	2.07e+06 ± 1.15e+06			3.18e+07 ± 1.37e+07		
Trigger	1.66e+06 ± 9.14e+05			1.39e+07 ± 6.66e+06		
Vertex Requirement	1.64e+06 ± 9.02e+05			1.37e+07 ± 6.56e+06		
Event Cleaning	1.64e+06 ± 9.01e+05			1.37e+07 ± 6.56e+06		
Dead Regions	1.57e+06 ± 8.66e+05			1.33e+07 ± 6.35e+06		
Lepton p_T	1.31e+06 ± 7.17e+05			1.07e+07 ± 5.33e+06		
$Di-lepton\ Veto$	6.37e+05 ± 3.46e+05			1.07e+07 ± 5.32e+06		
Tau ID	7883 ± 3792			4.86e+04 ± 1.86e+04		
Charge Correlation	6670 ± 3496			3.66e+04 ± 1.41e+04		
Missing p_T	682 ± 243			3.12e+04 ± 1.21e+04		
Transverse Mass	155 ± 71			2025 ± 672		
	$0-jet$	$1-jet$	$2-jet$	$0-jet$	$1-jet$	$2-jet$
N_{Jets}	105 ± 17	23.0 ± 7.7	17.7 ± 6.7	659 ± 61	345 ± 32	187 ± 21
Visible Mass	74.1 ± 14.0	12.8 ± 5.7	10.1 ± 5.0	167 ± 30	107 ± 18	72.9 ± 13.3

Table 30: Number of events in 1 fb^{-1} data for $Z \to ll$ and $W \to e/\mu/\tau\nu$ backgrounds to MSSM $h/A/H(170\ GeV) \to \tau\tau \to lh$ analysis.

	$t\bar{t}$			*Single Top* (Wt)			*Single Top* ($s+t-channels$)		
Start	8.74e+04 ± 8.74e+01			1.46e+04 ± 1.19e+02			2.29e+04 ± 1.25e+02		
Trigger	5.75e+04 ± 7.09e+01			5921 ± 76			1.31e+04 ± 9.52e+01		
Vertex Requirement	5.69e+04 ± 7.05e+01			5846 ± 75			1.29e+04 ± 9.47e+01		
Event Cleaning	5.69e+04 ± 7.05e+01			5842 ± 75			1.29e+04 ± 9.47e+01		
Dead Regions	5.49e+04 ± 6.93e+01			5651 ± 74			1.25e+04 ± 9.31e+01		
Lepton p_T	4.31e+04 ± 6.14e+01			4059 ± 63			9845 ± 83		
$Di-lepton\ Veto$	3.76e+04 ± 5.73e+01			3519 ± 58			9749 ± 82		
Tau ID	1766 ± 12			190 ± 14			168 ± 11		
Charge Correlation	1430 ± 11			149 ± 12			121 ± 9		
Missing p_T	1303 ± 11			133 ± 11			109 ± 9		
Transverse Mass	134 ± 3			10.7 ± 3.2			9.44 ± 2.58		
	$0-jet$	$1-jet$	$2-jet$	$0-jet$	$1-jet$	$2-jet$	$0-jet$	$1-jet$	$2-jet$
N_{Jets}	0.17 ± 0.12	5.60 ± 0.70	28.8 ± 1.6	0.0 ± 0.0	0.97 ± 0.97	3.89 ± 1.94	0.72 ± 0.72	5.72 ± 2.02	2.91 ± 1.43
Visible Mass	0.09 ± 0.09	1.66 ± 0.38	8.83 ± 0.88	0.0 ± 0.0	0.0 ± 0.0	0.97 ± 0.97	0.0 ± 0.0	1.43 ± 1.01	0.72 ± 0.72

Table 31: Number of events in 1 fb^{-1} data for $t\bar{t}$ and single top backgrounds to MSSM $h/A/H(170\ GeV) \to \tau\tau \to lh$ analysis.

	QCD			*QCD* (*single lepton filter*)		
Start	1.05e+13 ± 8.26e+09			3.06e+09 ± 2.64e+06		
Trigger	2.94e+09 ± 8.73e+07			8.24e+08 ± 1.31e+06		
Vertex Requirement	2.89e+09 ± 8.64e+07			8.14e+08 ± 1.30e+06		
Event Cleaning	2.89e+09 ± 8.64e+07			8.14e+08 ± 1.30e+06		
Dead Regions	2.84e+09 ± 8.50e+07			8.09e+08 ± 1.29e+06		
Lepton p_T	1.52e+08 ± 1.56e+07			6.02e+07 ± 3.48e+05		
$Di-lepton\ Veto$	1.51e+08 ± 1.55e+07			5.93e+07 ± 3.46e+05		
Tau ID	3.54e+05 ± 9.79e+04			1.40e+05 ± 1.04e+04		
Charge Correlation	2.23e+05 ± 7.81e+04			6.46e+04 ± 6.83e+03		
Missing p_T	1962 ± 1577			6471 ± 2315		
Transverse Mass	190 ± 109			5914 ± 2303		
	$0-jet$	$1-jet$	$2-jet$	$0-jet$	$1-jet$	$2-jet$
N_{Jets}	0.0 ± 0.0	0.03 ± 0.03	62.9 ± 62.9	4721 ± 2246	797 ± 464	132 ± 82
Visible Mass	0.0 ± 0.0	0.0 ± 0.0	0.0 ± 0.0	884 ± 625	174 ± 100	57.9 ± 57.9

Table 32: Number of events in 1 fb^{-1} data for QCD backgrounds to MSSM $h/A/H(170\ GeV) \to \tau\tau \to lh$ analysis.

	$ggA(200) \to \tau\tau$			$bbA(200) \to \tau\tau$			$Z \to \tau\tau$		
Start	162 ± 1			504 ± 2			1.03e+06 ± 8.36e+05		
Trigger	74.9 ± 0.6			314 ± 2			2.10e+05 ± 1.62e+05		
Vertex Requirement	74.1 ± 0.5			310 ± 2			2.07e+05 ± 1.60e+05		
Event Cleaning	74.0 ± 0.5			310 ± 2			2.07e+05 ± 1.60e+05		
Dead Regions	71.3 ± 0.5			299 ± 2			2.02e+05 ± 1.56e+05		
Lepton p_T	53.7 ± 0.5			231 ± 2			1.10e+05 ± 8.17e+04		
$Di-lepton\ Veto$	44.7 ± 0.4			226 ± 2			9.85e+04 ± 7.34e+04		
Tau ID	15.7 ± 0.3			90.4 ± 1.0			8556 ± 6243		
Charge Correlation	15.3 ± 0.2			89.2 ± 0.9			8306 ± 6152		
Missing p_T	9.55 ± 0.20			56.9 ± 0.8			2463 ± 1564		
Transverse Mass	7.81 ± 0.18			47.6 ± 0.7			2191 ± 1489		
	$0-jet$	$1-jet$	$2-jet$	$0-jet$	$1-jet$	$2-jet$	$0-jet$	$1-jet$	$2-jet$
N_{Jets}	4.51 ± 0.14	2.31 ± 0.10	0.71 ± 0.05	28.7 ± 0.5	13.4 ± 0.4	4.02 ± 0.20	1366 ± 60	464 ± 38	258 ± 26
Visible Mass	3.45 ± 0.12	1.69 ± 0.08	0.54 ± 0.05	21.8 ± 0.5	9.97 ± 0.32	3.01 ± 0.17	60.7 ± 13.0	5.92 ± 4.21	14.8 ± 6.1

Table 33: Number of events in 1 fb^{-1} data for signal and $Z \to \tau\tau$ background to MSSM $h/A/H(200\ GeV) \to \tau\tau \to lh$ analysis.

	$Z \to ll$			$W \to e/\mu/\tau\nu$		
Start	2.07e+06 ± 1.15e+06			3.18e+07 ± 1.37e+07		
Trigger	1.66e+06 ± 9.14e+05			1.39e+07 ± 6.66e+06		
Vertex Requirement	1.64e+06 ± 9.02e+05			1.37e+07 ± 6.56e+06		
Event Cleaning	1.64e+06 ± 9.01e+05			1.37e+07 ± 6.56e+06		
Dead Regions	1.57e+06 ± 8.66e+05			1.33e+07 ± 6.35e+06		
Lepton p_T	1.31e+06 ± 7.17e+05			1.07e+07 ± 5.33e+06		
$Di-lepton\ Veto$	6.37e+05 ± 3.46e+05			1.07e+07 ± 5.32e+06		
Tau ID	7883 ± 3792			4.86e+04 ± 1.86e+04		
Charge Correlation	6670 ± 3496			3.66e+04 ± 1.41e+04		
Missing p_T	682 ± 243			3.12e+04 ± 1.21e+04		
Transverse Mass	155 ± 71			2025 ± 672		
	$0-jet$	$1-jet$	$2-jet$	$0-jet$	$1-jet$	$2-jet$
N_{Jets}	105 ± 17	23.0 ± 7.7	17.7 ± 6.7	659 ± 61	345 ± 32	187 ± 21
Visible Mass	74.1 ± 14.0	12.8 ± 5.7	10.1 ± 5.0	216 ± 34	146 ± 20	85.1 ± 14.4

Table 34: Number of events in 1 fb^{-1} data for $Z \to ll$ and $W \to e/\mu/\tau\nu$ backgrounds to MSSM $h/A/H(200\ GeV) \to \tau\tau \to lh$ analysis.

	$t\bar{t}$			*Single Top* (Wt)			*Single Top* ($s+t-channels$)		
Start	8.74e+04 ± 8.74e+01			1.46e+04 ± 1.19e+02			2.29e+04 ± 1.25e+02		
Trigger	5.75e+04 ± 7.09e+01			5921 ± 76			1.31e+04 ± 9.52e+01		
Vertex Requirement	5.69e+04 ± 7.05e+01			5846 ± 75			1.29e+04 ± 9.47e+01		
Event Cleaning	5.69e+04 ± 7.05e+01			5842 ± 75			1.29e+04 ± 9.47e+01		
Dead Regions	5.49e+04 ± 6.93e+01			5651 ± 74			1.25e+04 ± 9.31e+01		
Lepton p_T	4.31e+04 ± 6.14e+01			4059 ± 63			9845 ± 83		
$Di-lepton\ Veto$	3.76e+04 ± 5.73e+01			3519 ± 58			9749 ± 82		
Tau ID	1766 ± 12			190 ± 14			168 ± 11		
Charge Correlation	1430 ± 11			149 ± 12			121 ± 9		
Missing p_T	1303 ± 11			133 ± 11			109 ± 9		
Transverse Mass	134 ± 3			10.7 ± 3.2			9.44 ± 2.58		
	$0-jet$	$1-jet$	$2-jet$	$0-jet$	$1-jet$	$2-jet$	$0-jet$	$1-jet$	$2-jet$
N_{Jets}	0.17 ± 0.12	5.60 ± 0.70	28.8 ± 1.6	0.0 ± 0.0	0.97 ± 0.97	3.89 ± 1.94	0.72 ± 0.72	5.72 ± 2.02	2.91 ± 1.43
Visible Mass	0.09 ± 0.09	2.45 ± 0.46	11.9 ± 1.0	0.0 ± 0.0	0.97 ± 0.97	0.97 ± 0.97	0.0 ± 0.0	2.14 ± 1.24	0.72 ± 0.72

Table 35: Number of events in 1 fb^{-1} data for $t\bar{t}$ and single top backgrounds to MSSM $h/A/H(200\ GeV) \to \tau\tau \to lh$ analysis.

	QCD			*QCD* (*single lepton filter*)		
Start	1.05e+13 ± 8.26e+09			3.06e+09 ± 2.64e+06		
Trigger	2.94e+09 ± 8.73e+07			8.24e+08 ± 1.31e+06		
Vertex Requirement	2.89e+09 ± 8.64e+07			8.14e+08 ± 1.30e+06		
Event Cleaning	2.89e+09 ± 8.64e+07			8.14e+08 ± 1.30e+06		
Dead Regions	2.84e+09 ± 8.50e+07			8.09e+08 ± 1.29e+06		
Lepton p_T	1.52e+08 ± 1.56e+07			6.02e+07 ± 3.48e+05		
$Di-lepton\ Veto$	1.51e+08 ± 1.55e+07			5.93e+07 ± 3.46e+05		
Tau ID	3.54e+05 ± 9.79e+04			1.40e+05 ± 1.04e+04		
Charge Correlation	2.23e+05 ± 7.81e+04			6.46e+04 ± 6.83e+03		
Missing p_T	1962 ± 1577			6471 ± 2315		
Transverse Mass	190 ± 109			5914 ± 2303		
	$0-jet$	$1-jet$	$2-jet$	$0-jet$	$1-jet$	$2-jet$
N_{Jets}	0.0 ± 0.0	0.03 ± 0.03	62.9 ± 62.9	4721 ± 2246	797 ± 464	132 ± 82
Visible Mass	0.0 ± 0.0	0.0 ± 0.0	0.0 ± 0.0	2146 ± 1409	174 ± 100	61.8 ± 58.0

Table 36: Number of events in 1 fb^{-1} data for QCD backgrounds to MSSM $h/A/H(200\ GeV) \to \tau\tau \to lh$ analysis.

	$ggA(250) \to \tau\tau$			$bbA(250) \to \tau\tau$			$Z \to \tau\tau$		
Start	41.9 ± 0.2			197 ± 1			1.03e+06 ± 8.36e+05		
Trigger	20.2 ± 0.1			131 ± 1			2.10e+05 ± 1.62e+05		
Vertex Requirement	20.0 ± 0.1			129 ± 1			2.07e+05 ± 1.60e+05		
Event Cleaning	20.0 ± 0.1			129 ± 1			2.07e+05 ± 1.60e+05		
Dead Regions	19.2 ± 0.1			124 ± 1			2.02e+05 ± 1.56e+05		
Lepton p_T	14.9 ± 0.1			99.2 ± 0.6			1.10e+05 ± 8.17e+04		
$Di-lepton\ Veto$	12.3 ± 0.1			96.6 ± 0.6			9.85e+04 ± 7.34e+04		
Tau ID	4.70 ± 0.06			41.3 ± 0.4			8556 ± 6243		
Charge Correlation	4.60 ± 0.06			40.8 ± 0.4			8306 ± 6152		
Missing p_T	3.24 ± 0.05			29.0 ± 0.3			2463 ± 1564		
Transverse Mass	2.50 ± 0.04			23.1 ± 0.3			2191 ± 1489		
	$0-jet$	$1-jet$	$2-jet$	$0-jet$	$1-jet$	$2-jet$	$0-jet$	$1-jet$	$2-jet$
N_{Jets}	1.31 ± 0.03	0.80 ± 0.02	0.29 ± 0.01	12.6 ± 0.2	7.30 ± 0.17	2.40 ± 0.10	1366 ± 60	464 ± 38	258 ± 26
Visible Mass	1.03 ± 0.03	0.63 ± 0.02	0.23 ± 0.01	9.91 ± 0.20	5.87 ± 0.15	1.90 ± 0.09	51.5 ± 11.8	14.1 ± 6.4	9.78 ± 4.89

Table 37: Number of events in 1 fb^{-1} data for signal and $Z \to \tau\tau$ background to MSSM $h/A/H(250\ GeV) \to \tau\tau \to lh$ analysis.

	$Z \to ll$			$W \to e/\mu/\tau\nu$		
Start	2.07e+06 ± 1.15e+06			3.18e+07 ± 1.37e+07		
Trigger	1.66e+06 ± 9.14e+05			1.39e+07 ± 6.66e+06		
Vertex Requirement	1.64e+06 ± 9.02e+05			1.37e+07 ± 6.56e+06		
Event Cleaning	1.64e+06 ± 9.01e+05			1.37e+07 ± 6.56e+06		
Dead Regions	1.57e+06 ± 8.66e+05			1.33e+07 ± 6.35e+06		
Lepton p_T	1.31e+06 ± 7.17e+05			1.07e+07 ± 5.33e+06		
$Di-lepton\ Veto$	6.37e+05 ± 3.46e+05			1.07e+07 ± 5.32e+06		
Tau ID	7883 ± 3792			4.86e+04 ± 1.86e+04		
Charge Correlation	6670 ± 3496			3.66e+04 ± 1.41e+04		
Missing p_T	682 ± 243			3.12e+04 ± 1.21e+04		
Transverse Mass	155 ± 71			2025 ± 672		
	$0-jet$	$1-jet$	$2-jet$	$0-jet$	$1-jet$	$2-jet$
N_{Jets}	105 ± 17	23.0 ± 7.7	17.7 ± 6.7	659 ± 61	345 ± 32	187 ± 21
Visible Mass	42.4 ± 10.6	5.13 ± 3.63	4.99 ± 3.53	160 ± 29	135 ± 19	70.5 ± 13.1

Table 38: Number of events in 1 fb^{-1} data for $Z \to ll$ and $W \to e/\mu/\tau\nu$ backgrounds to MSSM $h/A/H(250\ GeV) \to \tau\tau \to lh$ analysis.

	$t\bar{t}$			*Single Top* (Wt)			*Single Top* ($s+t-channels$)		
Start	8.74e+04 ± 8.74e+01			1.46e+04 ± 1.19e+02			2.29e+04 ± 1.25e+02		
Trigger	5.75e+04 ± 7.09e+01			5921 ± 76			1.31e+04 ± 9.52e+01		
Vertex Requirement	5.69e+04 ± 7.05e+01			5846 ± 75			1.29e+04 ± 9.47e+01		
Event Cleaning	5.69e+04 ± 7.05e+01			5842 ± 75			1.29e+04 ± 9.47e+01		
Dead Regions	5.49e+04 ± 6.93e+01			5651 ± 74			1.25e+04 ± 9.31e+01		
Lepton p_T	4.31e+04 ± 6.14e+01			4059 ± 63			9845 ± 83		
$Di-lepton\ Veto$	3.76e+04 ± 5.73e+01			3519 ± 58			9749 ± 82		
Tau ID	1766 ± 12			190 ± 14			168 ± 11		
Charge Correlation	1430 ± 11			149 ± 12			121 ± 9		
Missing p_T	1303 ± 11			133 ± 11			109 ± 9		
Transverse Mass	134 ± 3			10.7 ± 3.2			9.44 ± 2.58		
	$0-jet$	$1-jet$	$2-jet$	$0-jet$	$1-jet$	$2-jet$	$0-jet$	$1-jet$	$2-jet$
N_{Jets}	0.17 ± 0.12	5.60 ± 0.70	28.8 ± 1.6	0.0 ± 0.0	0.97 ± 0.97	3.89 ± 1.94	0.72 ± 0.72	5.72 ± 2.02	2.91 ± 1.43
Visible Mass	0.09 ± 0.09	2.54 ± 0.47	11.7 ± 1.0	0.0 ± 0.0	0.97 ± 0.97	0.0 ± 0.0	0.0 ± 0.0	1.43 ± 1.01	0.72 ± 0.72

Table 39: Number of events in 1 fb^{-1} data for $t\bar{t}$ and single top backgrounds to MSSM $h/A/H(250\ GeV) \to \tau\tau \to lh$ analysis.

	QCD			*QCD* (*single lepton filter*)		
Start	1.05e+13 ± 8.26e+09			3.06e+09 ± 2.64e+06		
Trigger	2.94e+09 ± 8.73e+07			8.24e+08 ± 1.31e+06		
Vertex Requirement	2.89e+09 ± 8.64e+07			8.14e+08 ± 1.30e+06		
Event Cleaning	2.89e+09 ± 8.64e+07			8.14e+08 ± 1.30e+06		
Dead Regions	2.84e+09 ± 8.50e+07			8.09e+08 ± 1.29e+06		
Lepton p_T	1.52e+08 ± 1.56e+07			6.02e+07 ± 3.48e+05		
$Di-lepton\ Veto$	1.51e+08 ± 1.55e+07			5.93e+07 ± 3.46e+05		
Tau ID	3.54e+05 ± 9.79e+04			1.40e+05 ± 1.04e+04		
Charge Correlation	2.23e+05 ± 7.81e+04			6.46e+04 ± 6.83e+03		
Missing p_T	1962 ± 1577			6471 ± 2315		
Transverse Mass	190 ± 109			5914 ± 2303		
	$0-jet$	$1-jet$	$2-jet$	$0-jet$	$1-jet$	$2-jet$
N_{Jets}	0.0 ± 0.0	0.03 ± 0.03	62.9 ± 62.9	4721 ± 2246	797 ± 464	132 ± 82
Visible Mass	0.0 ± 0.0	0.0 ± 0.0	62.9 ± 62.9	2146 ± 1409	116 ± 82	4.16 ± 3.89

Table 40: Number of events in 1 fb^{-1} data for QCD backgrounds to MSSM $h/A/H(250\ GeV) \to \tau\tau \to lh$ analysis.

	$ggA(300) \to \tau\tau$			$bbA(300) \to \tau\tau$			$Z \to \tau\tau$		
Start	11.7 ± 0.1			80.2 ± 0.4			1.03e+06 ± 8.36e+05		
Trigger	5.90 ± 0.06			55.8 ± 0.3			2.10e+05 ± 1.62e+05		
Vertex Requirement	5.83 ± 0.06			55.1 ± 0.3			2.07e+05 ± 1.60e+05		
Event Cleaning	5.82 ± 0.06			55.0 ± 0.3			2.07e+05 ± 1.60e+05		
Dead Regions	5.57 ± 0.06			53.1 ± 0.3			2.02e+05 ± 1.56e+05		
Lepton p_T	4.40 ± 0.05			43.5 ± 0.3			1.10e+05 ± 8.17e+04		
$Di-lepton\ Veto$	3.59 ± 0.05			42.2 ± 0.3			9.85e+04 ± 7.34e+04		
Tau ID	1.43 ± 0.03			18.4 ± 0.2			8556 ± 6243		
Charge Correlation	1.41 ± 0.03			18.2 ± 0.2			8306 ± 6152		
Missing p_T	1.07 ± 0.03			13.9 ± 0.1			2463 ± 1564		
Transverse Mass	0.80 ± 0.02			10.7 ± 0.1			2191 ± 1489		
	$0-jet$	$1-jet$	$2-jet$	$0-jet$	$1-jet$	$2-jet$	$0-jet$	$1-jet$	$2-jet$
N_{Jets}	0.41 ± 0.02	0.26 ± 0.01	0.10 ± 0.01	5.40 ± 0.09	3.50 ± 0.07	1.22 ± 0.04	1366 ± 60	464 ± 38	258 ± 26
Visible Mass	0.32 ± 0.01	0.20 ± 0.01	0.08 ± 0.01	4.36 ± 0.08	2.76 ± 0.07	1.01 ± 0.04	35.6 ± 9.9	14.1 ± 6.4	9.78 ± 4.89

Table 41: Number of events in 1 fb^{-1} data for signal and $Z \to \tau\tau$ background to MSSM $h/A/H(300\ GeV) \to \tau\tau \to lh$ analysis.

	$Z \to ll$			$W \to e/\mu/\tau\nu$		
Start	2.07e+06 ± 1.15e+06			3.18e+07 ± 1.37e+07		
Trigger	1.66e+06 ± 9.14e+05			1.39e+07 ± 6.66e+06		
Vertex Requirement	1.64e+06 ± 9.02e+05			1.37e+07 ± 6.56e+06		
Event Cleaning	1.64e+06 ± 9.01e+05			1.37e+07 ± 6.56e+06		
Dead Regions	1.57e+06 ± 8.66e+05			1.33e+07 ± 6.35e+06		
Lepton p_T	1.31e+06 ± 7.17e+05			1.07e+07 ± 5.33e+06		
$Di-lepton\ Veto$	6.37e+05 ± 3.46e+05			1.07e+07 ± 5.32e+06		
Tau ID	7883 ± 3792			4.86e+04 ± 1.86e+04		
Charge Correlation	6670 ± 3496			3.66e+04 ± 1.41e+04		
Missing p_T	682 ± 243			3.12e+04 ± 1.21e+04		
Transverse Mass	155 ± 71			2025 ± 672		
	$0-jet$	$1-jet$	$2-jet$	$0-jet$	$1-jet$	$2-jet$
N_{Jets}	105 ± 17	23.0 ± 7.7	17.7 ± 6.7	659 ± 61	345 ± 32	187 ± 21
Visible Mass	10.6 ± 5.3	2.56 ± 2.56	2.46 ± 2.46	145 ± 29	112 ± 17	68.1 ± 12.9

Table 42: Number of events in 1 fb^{-1} data for $Z \to ll$ and $W \to e/\mu/\tau\nu$ backgrounds to MSSM $h/A/H(300\ GeV) \to \tau\tau \to lh$ analysis.

	$t\bar{t}$			*Single Top* (Wt)			*Single Top* ($s+t-channels$)		
Start	8.74e+04 ± 8.74e+01			1.46e+04 ± 1.19e+02			2.29e+04 ± 1.25e+02		
Trigger	5.75e+04 ± 7.09e+01			5921 ± 76			1.31e+04 ± 9.52e+01		
Vertex Requirement	5.69e+04 ± 7.05e+01			5846 ± 75			1.29e+04 ± 9.47e+01		
Event Cleaning	5.69e+04 ± 7.05e+01			5842 ± 75			1.29e+04 ± 9.47e+01		
Dead Regions	5.49e+04 ± 6.93e+01			5651 ± 74			1.25e+04 ± 9.31e+01		
Lepton p_T	4.31e+04 ± 6.14e+01			4059 ± 63			9845 ± 83		
$Di-lepton\ Veto$	3.76e+04 ± 5.73e+01			3519 ± 58			9749 ± 82		
Tau ID	1766 ± 12			190 ± 14			168 ± 11		
Charge Correlation	1430 ± 11			149 ± 12			121 ± 9		
Missing p_T	1303 ± 11			133 ± 11			109 ± 9		
Transverse Mass	134 ± 3			10.7 ± 3.2			9.44 ± 2.58		
	$0-jet$	$1-jet$	$2-jet$	$0-jet$	$1-jet$	$2-jet$	$0-jet$	$1-jet$	$2-jet$
N_{Jets}	0.17 ± 0.12	5.60 ± 0.70	28.8 ± 1.6	0.0 ± 0.0	0.97 ± 0.97	3.89 ± 1.94	0.72 ± 0.72	5.72 ± 2.02	2.91 ± 1.43
Visible Mass	0.0 ± 0.0	2.45 ± 0.46	10.8 ± 1.0	0.0 ± 0.0	0.97 ± 0.97	0.0 ± 0.0	0.0 ± 0.0	0.71 ± 0.71	0.72 ± 0.72

Table 43: Number of events in 1 fb^{-1} data for $t\bar{t}$ and single top backgrounds to MSSM $h/A/H(300\ GeV) \to \tau\tau \to lh$ analysis.

	QCD			*QCD* (*single lepton filter*)		
Start	1.05e+13 ± 8.26e+09			3.06e+09 ± 2.64e+06		
Trigger	2.94e+09 ± 8.73e+07			8.24e+08 ± 1.31e+06		
Vertex Requirement	2.89e+09 ± 8.64e+07			8.14e+08 ± 1.30e+06		
Event Cleaning	2.89e+09 ± 8.64e+07			8.14e+08 ± 1.30e+06		
Dead Regions	2.84e+09 ± 8.50e+07			8.09e+08 ± 1.29e+06		
Lepton p_T	1.52e+08 ± 1.56e+07			6.02e+07 ± 3.48e+05		
$Di-lepton\ Veto$	1.51e+08 ± 1.55e+07			5.93e+07 ± 3.46e+05		
Tau ID	3.54e+05 ± 9.79e+04			1.40e+05 ± 1.04e+04		
Charge Correlation	2.23e+05 ± 7.81e+04			6.46e+04 ± 6.83e+03		
Missing p_T	1962 ± 1577			6471 ± 2315		
Transverse Mass	190 ± 109			5914 ± 2303		
	$0-jet$	$1-jet$	$2-jet$	$0-jet$	$1-jet$	$2-jet$
N_{Jets}	0.0 ± 0.0	0.03 ± 0.03	62.9 ± 62.9	4721 ± 2246	797 ± 464	132 ± 82
Visible Mass	0.0 ± 0.0	0.0 ± 0.0	62.9 ± 62.9	1263 ± 1263	120 ± 82	4.16 ± 3.89

Table 44: Number of events in 1 fb^{-1} data for QCD backgrounds to MSSM $h/A/H(300\ GeV) \to \tau\tau \to lh$ analysis.

Bibliography

[1] "CERN Web Page." http://public.web.cern.ch/Public/Welcome.html.

[2] P. W. Higgs, "Spontaneous Symmetry Breakdown without Massless Bosons," *Phys. Rev.*, vol. 145, pp. 1156–1163, 1966.

[3] B.R.Martin and G.Shaw, *Particle Physics, Second Edition.* Wiley, 1997.

[4] The LEP Working Group for Higgs Boson Searches, on behalf of the ALEPH, DELPHI, L3 and OPAL Collaborations, "Search for the Standard Model Higgs Boson at LEP," *Phys. Lett. B*, vol. 565, pp. 61–75, March 2003.

[5] The TEVNPH Working Group, for the CDF and D0 Collaborations, "Combined CDF and D0 Upper Limits on Standard Model Higgs-Boson Production with up to 6.7 fb^{-1} of Data," July 2010. Results prepared for the ICHEP 2010 conference, 22-28 July 2010, Paris, France.

[6] H. Flacher, M. Goebel, J. Haller, A. Hocker, K. Monig, and J. Stelzer, "Revisiting the Global Electroweak Fit of the Standard Model and Beyond with Gfitter," *Eur. Phys. J. C*, vol. 60, pp. 543–583. 65 p, Oct 2008. Gfitter web: http://cern.ch/project-gfitter.

[7] O. Buchmueller, R. Cavanaugh, A. De Roeck, J. R. Ellis, H. Flacher, S. Heinemeyer, G. Isidori, K. A. Olive, F. J. Ronga, and G. Weiglein, "Predictions for m_t and M_W in Minimal Supersymmetric Models," *Phys. Rev. D*, vol. 81, p. 035009, Dec 2009.

[8] M. S. Carena, S. Heinemeyer, C. E. M. Wagner, and G. Weiglein, "Suggestions for Benchmark Scenarios for MSSM Higgs Boson Searches at Hadron Colliders," *Eur. Phys. J. C*, vol. 26, pp. 601–7. 8 p, Feb 2002.

[9] The ATLAS Collaboration, "Expected Performance of the ATLAS Experiment: Detector, Trigger and Physics," Tech. Rep. arXiv:0901.0512. CERN-OPEN-2008-020, Geneva, 2009.

[10] *ATLAS Detector and Physics Performance Technical Design Report*. No. CERN-LHCC-99-14, Geneva: CERN, 1999.

[11] S. Asai, G. Azuelos, C. Buttar, V. Cavasinni, D. Costanzo, K. Cranmer, R. Harper, K. Jakobs, J. Kanzaki, M. Klute, R. Mazini, B. Mellado, W. Quayle, E. Richter-Was, T. Takemoto, I. Vivarelli, and W. S. Lan, "Prospects for the Search for a Standard Model Higgs Boson in ATLAS using Vector Boson Fusion," *Eur. Phys. J. C*, vol. 32, no. hep-ph/0402254. Suppl. 2, pp. s19–s54, 2004.

[12] The TEVNPH Working Group, for the CDF and D0 Collaborations, "Combined CDF and D0 Upper Limits on MSSM Higgs-Boson Production in Tau-Tau Final States with up to 2.2 fb^{-1}," March 2010.

[13] "The ATLAS Experiment at CERN." http://atlas.ch.

[14] *ATLAS Inner Detector Technical Design Report*, vol. 2. Geneva: CERN, 1997.

[15] *ATLAS Calorimeter Technical Design Report*. No. CERN-LHCC-96-40, Geneva: CERN, 1996.

[16] *ATLAS Muon Spectrometer Technical Design Report*. No. CERN-LHCC-97-022, Geneva: CERN, 1997.

[17] "ATLAS Luminosity Determination and Forward Physics." http://atlas-project-lumi-fphys.web.cern.ch/atlas-project-lumi-fphys/.

[18] N. Soni, "ATLAS Forward Detectors and Physics," Tech. Rep. arXiv:1006.5426. ATL-LUM-PROC-2010-002, CERN, Jun 2010.

[19] "ZDC Documentation."
https://twiki.cern.ch/twiki/bin/view/Atlas/ZeroDegreeCalorimeter
Revision 14, 18-Dec-2009.

[20] P. Jenni, M. Nessi, and M. Nordberg, "Zero Degree Calorimeters for ATLAS," Tech. Rep. LHCC-I-016. CERN-LHCC-2007-001, CERN, Geneva, Jan 2007.

[21] "ALFA Documentation."
http://atlas-project-lumi-fphys.web.cern.ch/atlas-project-lumi-fphys/ALFA/.

[22] "ATLAS Trigger Overview."
https://twiki.cern.ch/twiki/bin/view/Atlas/TriggerForDummies
Revision 10, 02-Jul-2007.

[23] A. Corso-Radu, S. Kolos, H. Hadavand, R. Kehoe, and M. Hauschild, "Data Quality Monitoring Framework for the ATLAS Experiment at the LHC," Tech. Rep. IEEE Trans Nucl. Sci. **54** 5, ATL-DAQ-CONF-2008-006, Geneva, Oct 2007.

[24] N. P. Konstantinidis, J. Drohan, Z. Maxa, H. Drevermann, J. Couchman, C. Timmermans, P. Klok, F. Crijns, G. Taylor, D. Petrusca, and E. Jansen, "The Atlantis Event Visualisation Program for the ATLAS Experiment," no. Computing in High Energy Physics and Nuclear Physics 2004, p. 361, 2004.

[25] J. Boudreau, T. Kittelmann, and V. Tsulaia, "VP1 Web Page."
http://atlas-vp1.web.cern.ch/atlas-vp1/index.ph.

[26] "Finite State Machine Definition."
http://en.wikipedia.org/wiki/Finite-state_machine, 9-Sept-2010.

[27] A. Barriuso Poy, H. Boterenbrood, H. J. Burckhart, J. Cook, V. Filimonov, S. Franz, O. Gutzwiller, B. Hallgren, V. Khomutnikov, S. Schlenker, and F. Varela, "The Detector Control System of the ATLAS Experiment," *J. Instrum.*, vol. 3, p. P05006, 2008.

[28] "COOL Package Documentation."
http://lcgapp.cern.ch/doxygen/COOL/COOL_2_6_0/doxygen/html.

[29] "SQLite Database Engine Documentation." http://www.sqlite.org.

[30] P. W. Phillips, "SCT DCS Software."
https://twiki.cern.ch/twiki/bin/view/Atlas/SctDCSSoftware
Revision 11, 16-Oct-2009.

[31] "CoraCool Documentation."
http://alxr.usatlas.bnl.gov/lxr/source/atlas/Database/CoraCool/doc/mainpage.h.

[32] P. Onyisi, "Physics Object Flags Documentation."
https://twiki.cern.ch/twiki/bin/view/Atlas/DQVirtualFlagProposal
Revision 15, 11-Dec-2009.

[33] C. Amsler *et al.*, "Review of particle physics," *Phys. Lett.*, vol. B667, p. 1, 2008.

[34] The ATLAS Collaboration, "Cut-based Identification of Hadronic τ Decays in Early ATLAS Data," Tech. Rep. ATL-PHYS-PUB-2010-001. ATL-COM-PHYS-2009-583, Geneva, January 2010.

[35] M. Cacciari, G. P. Salam, and G. Soyez, "The Anti-k_t Jet Clustering Algorithm," *J. High Energy Phys.*, vol. 04, p. 063. 12 p, Feb 2008.

[36] G. Corcella, I. G. Knowles, G. Marchesini, S. Moretti, K. Odagiri, P. Richardson, M. H. Seymour, and B. R. Webber, "HERWIG 6: An Event Generator for Hadron Emission Reactions With Interfering Gluons (including Supersymmetric Processes)," *J. High Energy Phys.*, vol. 01, p. 010. 93 p, Nov 2000.

[37] "ATHENA Documentation." https://twiki.cern.ch/twiki/bin/view/Atlas/WorkBookAthenaFramework.

[38] S. Frixione and B. R. Webber, "Matching NLO QCD Computations and Parton Shower Simulations," *J. High Energy Phys.*, vol. 06, p. 029. 69 p, Apr 2002.

[39] T. Sjstrand, S. Mrenna, and P. Z. Skands, "PYTHIA 6.4 Physics and Manual," *J. High Energy Phys.*, vol. 05, p. 026. 570 p, Mar 2006.

[40] A. Sherstnev and R. S. Thorne, "Parton Distributions for LO Generators," Tech. Rep. arXiv:0711.2473. CAVENDISH-HEP-2007-12, Nov 2007.

[41] T. Gleisberg, S. Hoeche, F. Krauss, M. Schoenherr, S. Schumann, F. Siegert, and J. Winter, "Event Generation with SHERPA 1.1," *J. High Energy Phys.*, vol. 02, p. 007, Dec 2008.

[42] "CTEQ Parton Distribution Functions." http://hep.pa.msu.edu/cteq/public/6.0_6.5/cteq6pdf.html.

[43] S. Jadach, Z. Was, R. Decker, and J. H. Kuhn, "The τ Decay Library TAUOLA, version 2.4," *Comput. Phys. Commun.*, vol. 76, pp. 361–380. 22 p, Feb 1993.

[44] M. Frank, T. Hahn, S. Heinemeyer, W. Hollik, H. Rzehak, and G. Weiglein, "The Higgs Boson Masses and Mixings of the Complex MSSM in the Feynman-Diagrammatic Approach," *J. High Energy Phys.*, vol. 02, p. 047. 56 p, Nov 2006.

[45] G. Degrassi, S. Heinemeyer, W. F. L. Hollik, P. Slavich, and G. Weiglein, "Towards High-Precision Predictions for the MSSM Higgs Sector," *Eur. Phys. J. C*, vol. 28, pp. 133–143. 19 p, Dec 2002.

[46] S. Heinemeyer, W. F. L. Hollik, and G. Weiglein, "The Masses of the Neutral CP-even Higgs Bosons in the MSSM: Accurate Analysis at the Two-Loop Level," *Eur. Phys. J. C*, vol. 9, pp. 343–366. 45 p, Dec 1998.

[47] S. Heinemeyer, W. F. L. Hollik, and G. Weiglein, "FeynHiggs: A Program for the Calculation of the Masses of the Neutral CP-Even Higgs Bosons in the MSSM," *Comput. Phys. Commun.*, vol. 124, pp. 76–89. 16 p, Dec 1998.

[48] M. L. Mangano, M. Moretti, F. Piccinini, R. Pittau, and A. Polosa, "ALPGEN, a Generator for Hard Multiparton Processes in Hadronic Collisions," *J. High Energy Phys.*, vol. 07, p. 001. 35 p, Jun 2002.

[49] J. Alwall, S. Hche, F. Krauss, N. Lavesson, L. Lonnblad, F. Maltoni, M. L. Mangano, M. Moretti, C. G. Papadopoulos, F. Piccinini, S. Schumann, M. Treccani, J. Winter, and M. Worek, "Comparative Study of Various Algorithms for the Merging of Parton Showers and Matrix Elements in Hadronic Collisions," *Eur. Phys. J. C*, vol. 53, pp. 473–500. mult. p, Jun 2007.

[50] S. e. Agostinelli, "GEANT4: A Simulation Toolkit," *Nucl. Instrum. Methods Phys. Res., A*, vol. 506, pp. 250–303. 86 p, Jul 2002.

[51] S. Winkelmann, M. Fehling, I. Vivarelli, X. Portell Bueso, K. Jakobs, T. Meguro, K. Hanagaki, T. Yamanaka, S. Asai, M. D'Onofrio, P. Laycock, G. Sellers, S. Mahmoud, A. Tua, D. Costanzo, A. Schwartzman, D. Silverstein, P. Hansson, B. Butler, and P. Jackson, "Early Supersymmetry Searches in Events with Missing Transverse Energy and b-Jets with the ATLAS Detector," Tech. Rep. ATLAS-CONF-2010-079, CERN, Geneva.

[52] R. Inoue, K. Leney, K. Nakamura, M. Schumacher, and J. Tanaka, "Data-driven Background Estimation for the $H \to \tau^+\tau^- \to lh$ Search at 7 TeV with the ATLAS Detector," Tech. Rep. ATLAS-CONF-2010-096, CERN, Geneva, Sept 2010.

[53] "Luminosity Determination Using the ATLAS Detector," Tech. Rep. ATLAS-CONF-2010-060, CERN, Geneva, Jul 2010.